REVIEW ARTICLE | NOVEMBER 18 2025

Mixed-anion thermoelectrics: Advanced tuning of electron and phonon transport

Takayoshi Katase ; Naoki Sato ; Takao Mori

Appl. Phys. Rev. 12, 041319 (2025)
https://doi.org/10.1063/5.0263175

Applied Physics Reviews REVIEW pubs.aip.org/aip/are

Mixed-anion thermoelectrics: Advanced tuning of electron and phonon transport

Cite as: Appl. Phys. Rev. **12**, 041319 (2025); doi: 10.1063/5.0263175
Submitted: 4 February 2025 · Accepted: 21 October 2025 ·
Published Online: 18 November 2025

Takayoshi Katase,[1,2,a] Naoki Sato,[3,b] and Takao Mori[3,4,c]

AFFILIATIONS

[1]MDX Research Center for Element Strategy, Institute of Integrated Research, Institute of Science Tokyo, 4259 Nagatsuta, Midori, Yokohama 226-8501, Japan
[2]Materials and Structures Laboratory, Institute of Integrated Research, Institute of Science Tokyo, 4259 Nagatsuta, Midori, Yokohama 226-8501, Japan
[3]Research Center for Materials Nanoarchitectonics (MANA), National Institute for Materials Science (NIMS), Namiki 1-1, Tsukuba 305-0044, Japan
[4]Graduate School of Pure and Applied Sciences, University of Tsukuba, Tennodai 1-1-1, Tsukuba 305-8671, Japan

[a]Electronic mail: katase.t.aa@m.titech.ac.jp
[b]Electronic mail: SATO.Naoki@nims.go.jp
[c]Author to whom correspondence should be addressed: MORI.Takao@nims.go.jp

ABSTRACT

Thermoelectric energy conversion is a promising renewable technology to generate electricity by recovering waste heat. Great progress has been made in energy conversion efficiency of thermoelectric materials, but further performance enhancement has been expected by developing new material design rules. Recently, "mixed-anion" materials, which consist of two or more anionic species in a single phase, have attracted much attention as a next-generation high-performance thermoelectric material. They form unique crystal structures and coordination not observed in single-anion systems and have demonstrated, for example, extremely low lattice thermal conductivity and also specific electronic structure enabling high thermoelectric performance. This paper provides a comprehensive review of the recent advances in mixed-anion thermoelectric materials and the mixed-anion effect on electron and phonon transport. We first provide an overview of the historical approach of multiple-anion substitution onto single-anion compounds and discuss the substantial impacts of multiple anion substitutions across different material systems. Then, we summarize the characteristics of crystal structures and physical properties, as well as the recent advances in thermoelectric properties for the mixed-anion compounds that naturally contain multiple anions. In the end, we point out the currently unsolved challenges and future prospects toward the development of mixed-anion thermoelectrics. Mixed-anion materials have a large degree of freedom regarding the choice of the constituent anion combinations, which provides a wide search space for new materials with further outstanding thermoelectric performance. Going forward, we expect that the mixed-anion strategy offers great potential for finding new classes of high-performance thermoelectric materials.

TABLE OF CONTENTS

I. INTRODUCTION

Ever-increasing energy consumption and growing environmental issues give considerable significance to explore sustainable and eco-friendly energy resources. Today, more than half of the total energy produced from fossil fuels is discarded as waste heat, which is ubiquitous in energy use processes in households, industrial sectors, and automobiles, as well as other energy uses in solar energy conversion and battery heat. If waste heat could be converted into a more useful form of energy such as electricity, we could minimize fuel consumption with reduced carbon emission. One of the most promising approaches to harvest such waste heat is to utilize thermoelectric materials, which can directly convert the waste heat into electrical energy via Seebeck effect.[1–4]

The energy conversion efficiency of the thermoelectric materials is a monotonically increasing function of the dimensionless figure of merit (ZT), defined as $ZT = S^2\sigma T/\kappa$, where S is the Seebeck coefficient, σ is the electronic conductivity, T is the absolute temperature, and κ is the thermal conductivity. The output electric power can be defined by $S^2\sigma$, which is called the power factor (PF), and κ includes the electronic thermal conductivity (κ_e) and lattice thermal conductivity (κ_{lat}). High-performance thermoelectric materials are typically made of heavily doped semiconductors, where both electrons and phonons contribute to thermal transport ($\kappa = \kappa_e + \kappa_{lat}$). To achieve a high ZT, both high S and high σ are required, while κ must be minimized, simultaneously. However, achieving high ZT is impeded by the well-known tradeoff relationship among the parameters. For example, σ and S have an opposite relation with the carrier concentration (n); i.e., σ increases with growing n, whereas S decreases, limiting the maximum PF at a certain n. Moreover, a higher σ usually results in a high κ_e, as represented by Wiedemann–Franz law of $\kappa_e = L\sigma T$ (L is the Lorenz number). Due to the complex coupling between these physical properties, designing thermoelectric materials with high ZT is highly challenging.[5] On the other hand, only κ_{lat} is almost independent of the other parameters, and effective reduction of κ_{lat} can often lead to ZT enhancement.

Many strategies have been developed to realize high ZT materials by enhancing PF and decreasing thermal conductivity over the past several decades. Enhancement of PF relies on optimizing the concentration, effective mass, and mobility of charge carriers through modification of the electronic band structure and density of states near the Fermi level. Various band structure engineering approaches, such as resonant state doping,[6,7] band convergence,[8,9] utilization of magnetism,[10] and dimensionality reduction,[11] have been demonstrated to tune electrical transport properties for PF enhancement. The reduction of lattice thermal conductivity usually involves structural engineering at various length scales. The conventional approach to enhance phonon scattering includes introducing extrinsic defects, such as atomic scale defects,[12–14] cation disorder,[15] and nanoscale precipitates,[16] as well as nanostructuring by grain refinement,[17,18] and porosity design.[19,20] In addition, low lattice thermal conductivity can be realized by intrinsic phonon scattering sources originating from chemical bonding and structural aspects, such as layered structures,[21] liquid-like sublattices,[22–24] chemical bond heterogeneity (the coexistence of strong and weak bonds),[25,26] local structural distortions,[27,28] ferroelectric instability,[29,30] anharmonic lattice vibrations originating from lone pairs,[31] and atomic rattling.[32] Minimizing lattice thermal conductivity by strong phonon scattering without deteriorating electronic conductivity (minimizing electron scattering) is the ideal solution for achieving high ZT materials. This is conceptualized as phonon-glass electron-crystal (PGEC),[33] where the phonon and electron transport channels are decoupled, thus facilitating independent control of phonon and electron transport.

These strategies have led to significant ZT enhancement in different classes of materials. For example, high ZT materials at ~300–500 K include $(Bi,Sb)_2(Se,Te)_3$-based alloys,[12,34,35] Mg_3Bi_2-based alloys,[36–38] and MgAgSb alloys.[39,40] For intermediate-temperature range ~500–900 K, promising candidates are PbCh (Ch = S, Se, Te),[41–45] SnCh (Ch = S, Se, Te),[21,46–49] GeTe,[50,51] Cu_2Ch (Ch = S, Se, Te),[22,52] $Mg_2(Si,Sn,Ge)$,[53,54] Mg_3Sb_2-based alloys,[55–59] BiCuOSe,[60,61] Zn_4Sb_3,[62,63] In_4Se_3,[64] $Ba_8Ga_{16}Ge_{30}$, and some other clathrate compounds,[65,66] $CoSb_3$-based filled skutterudites,[67–69] and tetrahedrites.[70–72] For high temperature range > 900 K, SiGe,[73,74] $(Pr,La)_3Te_4$,[75,76] $Yb_{14}MnSb_{11}$,[77,78] and half-Heusler alloys[79–81] have been developed up until now. There have been numerous excellent reviews of the strategies and progress in the development of thermoelectric materials[82–99] as well as mechanisms of the performance enhancement.[100–116]

On the other hand, "mixed-anion" materials, which consist of two or more anionic species in a single compound, have recently gained attention as next-generation thermoelectric materials with extremely low lattice thermal conductivity. In mixed-anion materials, the high flexibility in the arrangement of multiple anions with different sizes, masses, electronegativity, etc., enables the formation of unique crystal structures with specific local coordination. The mixed-anion materials have been proven to possess the potential to offer novel and attractive functionalities including catalysts, batteries, and superconductors, which were not observed in traditional "single-anion" materials.[117–120] In mixed-anion materials, special local structure can be designed to realize extremely low lattice thermal conductivity and also unique electronic structure for PF enhancement. Various kinds of anions can be selected and arranged in mixed-anion materials, which provide a wide search space for the new materials with outstanding thermoelectric performance. There have been many recent reports on the synthesis and properties of new mixed-anion materials. However, these are limited to an understanding of individual materials, and there

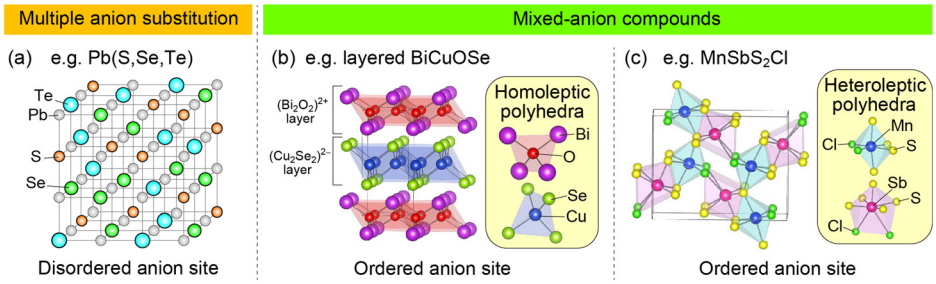

FIG. 1. Categorization of "mixed-anion" materials. (a) Multiple-anion substitution onto single-anion compounds. (b) and (c) Mixed-anion compounds that naturally contain multiple anions, which are classified into two types: (b) mixed-anion compounds with multiple homoleptic polyhedra and (c) mixed-anion compounds with heteroleptic polyhedra.

is a lack of research to achieve a comprehensive understanding of the material system and properties.

In this review, we aim to provide a comprehensive overview of the "mixed-anion concept" as a new strategy to develop thermoelectric materials, and highlight their characteristics and advantages. In Sec. II, we introduce the concept of mixed-anion materials and categorize them into three types based on structural perspective, followed by an overview of the multiple anion effect on electronic and thermal transport properties. In Sec. III, we comprehensively introduce recent advances in thermoelectric properties for each of the three categories of mixed-anion materials. In the end, we highlight the currently unsolved challenges and future prospects toward the development of mixed-anion thermoelectrics.

II. CLASSIFICATION OF MIXED-ANION MATERIALS AND VARIOUS ROLES OF MULTIPLE ANIONS

In this review, we classify mixed-anion materials into three types according to the arrangement of multiple anions within a single compound (Fig. 1). A typical example involves the partial substitution of anion sites in single-anion materials with different anions, which likely represents the majority of mixed-anion materials [Fig. 1(a)]. In most cases, the substituted anions randomly occupy the original anion sites, such as Pb(S,Se,Te). On the other hand, there are numerous compounds which naturally contain multiple types of anions occupying crystallographically inequivalent sites, such as oxynitrides, oxychalcogenides, and oxyhalides. These should be classified separately from the case of partial anion substitution as "mixed-anion compounds" [Figs. 1(b) and 1(c)]. Among the mixed-anion compounds, a further classification can be made based on their local structures. The first type includes the crystal structures consisting only of homoleptic coordination polyhedra, in which cations are coordinated by only one type of anion. In this case, multiple types of homoleptic polyhedra, each containing a different anion species, are spatially separated, such as $(Cu_2Se_2)^{2-}$ and $(Bi_2O_2)^{2-}$ layers in a layered BiCuOSe [Fig. 1(b)]. Multiple types of homoleptic polyhedra are not limited to layered compounds but can also be observed in three-dimensional frameworks. The second type comprises heteroleptic polyhedra, in which cations are coordinated with two or more different types of anions, e.g., $MnSbS_2Cl$ with heteroleptic polyhedra of $[MnS_4Cl_2]$ and $[SbS_5Cl_2]$ [Fig. 1(c)]. This type is characterized by significantly distorted local structures not observed in single-anion materials, due to the presence of multiple anions with notably different electronegativities and ionic radii within the coordination polyhedra. There are also intermediate cases, such as compounds that contain both homoleptic and heteroleptic polyhedra; for example, $Sr_6Ge_3OSe_{11}$ contains homoleptic $GeSe_4$ tetrahedra and heteroleptic $GeOSe_3$ polyhedra.[121] Viewed from another perspective, BiCuOSe can also be described as follows: Bi is coordinated by four O and four Se atoms, forming a heteroleptic BiO_4Se_4 square antiprism, while Cu is coordinated solely by Se atoms, forming homoleptic polyhedra.

To summarize, although there are some intermediate or exceptional cases, in this review we broadly classify "mixed-anion" materials into the three categories: (1) multiple anion substitution onto a single-anion compound, (2) mixed-anion compound with homoleptic polyhedra, and (3) mixed-anion compound with heteroleptic polyhedra.

(1) Partial anion substitution is one of the traditional strategies to enhance the thermoelectric performance of some single-anion materials [Fig. 1(a)]. Conventionally, aliovalent ion substitution is performed to control carrier concentration to optimize PF. Isovalent ion substitution is typically considered to provide minor changes in physical properties. However, the solid solution of a large amount of isovalent ions with different sizes, masses, electronegativity, etc., has significant effects on the large modulation of electronic and/or phonon band structures as well as the formation energy of donor or acceptor type defects. For example, isovalent anionic solid solutions, such as PbTe–PbSe,[8,111] have been regarded as an effective way to realize the PF enhancement by band structure engineering, and also the reduction of lattice thermal conductivity by the strong phonon-alloy scattering.

(2) Mixed-anion compounds consisting of multiple homoleptic polyhedra have been expected as potential thermoelectric materials with intrinsically low lattice thermal conductivity [Fig. 1(b)]. Mixed-anion compounds containing anions with different bonding characteristics to cations, with some forming predominantly ionic bonds and others forming predominantly covalent bonds, tend to form complex crystal structures. These are characterized by the coexistence of bonds with varying degrees of ionicity and covalency within a single phase, which sometimes leads to the formation of distinct structural blocks. Typical example is layered BiCuOSe, consisting of $(Cu_2Se_2)^{2-}$ and $(Bi_2O_2)^{2-}$ layers. The O and Se anions do not mix with each other, but form separate layers with homoleptic unit of O-Bi_4 and Cu-Se_4 polyhedra, respectively. The naturally formed superlattice structure, where conductive Cu_2Se_2 layer is sandwiched by insulating Bi_2O_2 layer, provides a highly anisotropic electronic band structure, resulting in sharp density of states around Fermi level and the large Seebeck coefficient. In addition, the two-dimensional (2D) layered network with strong chemical bonding, while having much weaker interaction

between the layers, provides the lattice anharmonicity and strong phonon scattering, resulting in the intrinsically low lattice thermal conductivity.

(3) Heteroleptic coordination environment in mixed-anion compounds [Fig. 1(c)] have various roles in determining their electronic and phonon transport properties. The different anion arrangements provide local structure symmetry breaking and the concomitant crystal-field splitting, which have a significant correlation with the electronic structures and modulate the effective mass and carrier scattering rate. In addition, it provides the chemical bond heterogeneity, which effectively realizes strong phonon scattering and extremely low lattice thermal conductivity. For example, $MnPnS_2Cl$ (Pn = Sb, Bi) contains two types of highly distorted heteroleptic units, $[MnS_4Cl_2]$ and $[PnS_5Cl_2]$. Bond strength between cations and anions shows a wide variety within these heteroleptic units, which results in an increase in the number of phonon scattering channels.[122] Such effects derived from the heteroleptic coordination can be more prominent than homoleptic mixed-anion compounds due to the pronounced distortion in local structures. Hence, utilizing unique bonding arrangements in heteroleptic unit could offer powerful opportunities for designing high ZT thermoelectric materials with extremely low lattice thermal conductivity.

The effects of incorporating multiple anions into a single material vary widely, ranging from straightforward outcomes to those still under investigation. Some of the mixed anion effects on electron and phonon transport properties are summarized in Fig. 2. As will be explained later, multiple anion substitutions at anion sites such as in Pb(Te,Se) enable electronic band structure engineering for increasing the band degeneracy and tuning the bandgap [Fig. 2(a)]. Furthermore, the variation of bond strengths formed by multiple anions can significantly modulate the phonon band structure [Fig. 2(b)]. Since phonon frequencies are highly dependent on the strength of interatomic interactions, vibrations arising from strong and weak bonds may split in frequency space, which markedly affects thermal transport. Additionally, the local symmetry breaking of heteroleptic coordination polyhedra places center cations in off-center environments [Fig. 2(c)], often resulting in highly anharmonic and localized vibrational states that substantially reduce lattice thermal conductivity. The large differences in ionic radius and electronegativity between anions affect the formation enthalpy of native defects. Thus, even with isovalent anion substitution, it is possible to control carrier concentration and, in some cases, switch carrier polarity [Fig. 2(d)]. The coexistence of distinct multiple chemical bonds, such as ionic and covalent bonds within a single material, also suggests that the units containing these bonds may spatially separate, as exemplified by BiCuOSe [Fig. 2(e)]. In such layered structures, conductive and insulating layers are separated, resulting in a strongly anisotropic electronic structure that often positively influences thermoelectric properties. Phonon transport is also affected by the anisotropic chemical bonding and weak interlayer interaction. Incorporating multiple anions often enhances phonon scattering and reduces lattice thermal conductivity. However, these same effects can increase carrier scattering and reduce electrical conductivity. Balancing these competing effects is therefore crucial for designing high-performance mixed-anion thermoelectric materials. On the other hand, in layered mixed-anion compounds where phonon-scattering layers and highly conductive layers are spatially separated, it is possible to achieve strong phonon scattering and low lattice thermal conductivity while maintaining high electrical conductivity, as charge carriers experience minimal scattering in the conducting layers.

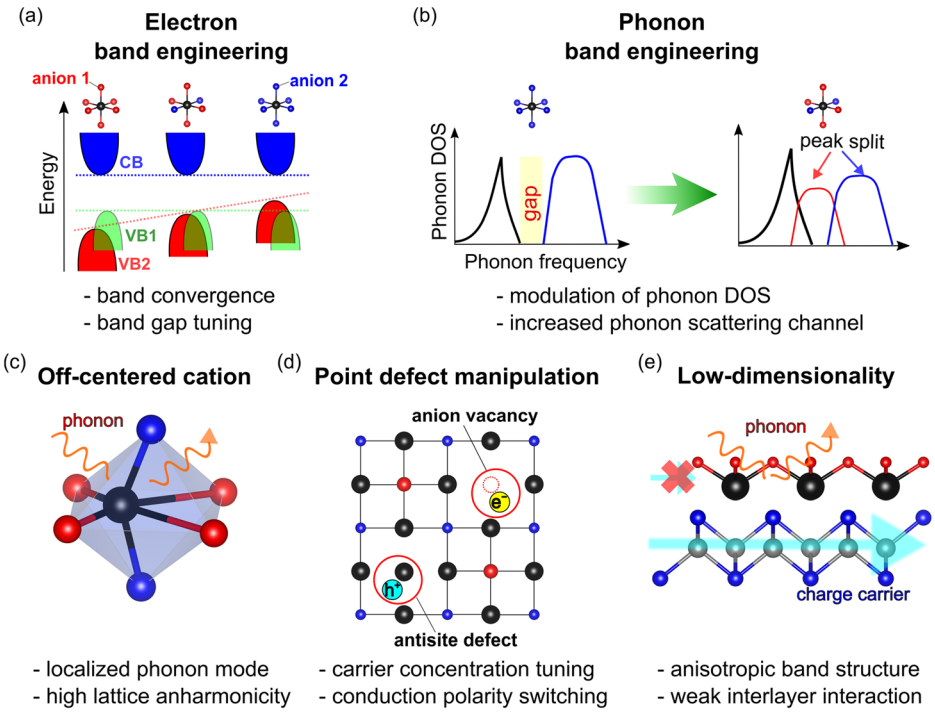

FIG. 2. Schematic illustrations of the effects of mixed-anion approach on electron and phonon transport properties. (a) Electron band engineering. Mixing of multiple anions modulates the relative band energies near the band edge, achieving band convergence and bandgap tuning. (b) Phonon band engineering. Bonding heterogeneity in heteroleptic coordination polyhedron induces a peak split in the phonon density of states (DOS), filling a gap and enhancing phonon scattering channel. (c) Off-centered cation. Heteroleptic polyhedra with significantly off-centered cations induce localized and highly anharmonic phonon modes that effectively hinder thermal transport. (d) Point defect manipulation. Formation energies of point defects can be tuned by anion mixing, enabling carrier concentration tuning and conduction polarity switching. (e) Low dimensionality. Layered structure of mixed-anion compounds, created by spatially separated distinct anions, leads to a large anisotropy in electron and phonon transport.

III. THERMOELECTRIC PROPERTIES OF MIXED-ANION MATERIALS

In this section, we introduce recent advances of mixed-anion thermoelectric materials and highlight prominent mixed-anion effects on electron and phonon transport properties across various material systems, based on the categorization described in Sec. II: multiple-anion substitution onto single-anion compounds (Sec. III A), mixed-anion compounds with homoleptic polyhedra (Sec. III B), and mixed-anion compounds with heteroleptic polyhedra (Sec. III C). Intermediate compounds that contain both homoleptic and heteroleptic polyhedra are included in Sec. III C. In Sec. III A, to comprehend the key developments of mixed-anion thermoelectric materials, we first highlight the historical approach of multiple-anion substitution onto single-anion compounds, presenting various examples of substantial impacts from multiple anion substitutions on electron and phonon transport. In Sec. III B, we provide an overview of the characteristics of crystal structures and physical properties, as well as the recent advances in thermoelectric properties for the mixed-anion layered compounds. In Sec. III C, we summarize the structural features and thermoelectric and thermal transport properties of mixed-anion compounds with heteroleptic local structures.

A. Multiple anion substitution onto single-anion compounds

One of the most common approaches to enhancing the performance of thermoelectric materials involves selecting a parent material with appropriate crystal and electronic structures, followed by elemental substitution to optimize carrier concentration and reduce lattice thermal conductivity. Thus, it is not uncommon in thermoelectric materials to find multiple anions within a single material, even in small amounts. Isovalent anionic substitution, much like cationic substitution, leads to somewhat minor changes in physical properties in many cases. For example, the effect of substituting S for Se in PbSe[123] on lattice thermal conductivity can be quantitatively explained using Klemens model, which considers point defect scattering arising from mass differences and strain fields.[124] However, there are some reports where such isovalent anionic substitutions have non-trivial effects on the electronic and/or thermal transport properties, thereby acquiring superior thermoelectric properties. Although these cases of anion substitution can be broadly categorized as mixed-anion materials, they should be distinguished from the groups of mixed-anion compounds that naturally contain multiple anions, introduced in Secs. III B and III C. In this section, we introduce various examples of substantial impacts from anionic substitutions across different materials systems, including notable changes in transport properties. We also present several metastable phases enabled by extensive anionic substitution. Here, the focus is on the effects of anionic substitutions, rather than providing a broad overview of thermoelectric materials. More general reviews covering a wider range of material systems are available.[5,88,90,91,97,99,103,115,116,125–127]

1. Bi_2Ch_3 (Ch = S, Se, Te)

Bi_2Te_3-based thermoelectric materials are among the most widely used commercially due to their superior performance near room temperature (RT) compared to other known materials.[128] Since the first report on thermoelectric properties of Bi_2Te_3-based materials, extensive studies have been conducted on the effects of various intrinsic defects, extrinsic dopants, and microstructures.[129–133]

In most cases, Bi_2Te_3-Sb_2Te_3 alloys are predominantly used for p-type materials, while Bi_2Te_3-Bi_2Se_3 alloys are commonly employed for n-type materials. The conduction type and carrier concentration of binary Bi_2Te_3 are primarily influenced by a high concentration of antisite defects, which arise due to the small differences in electronegativity and atomic size between Bi and Te.[134] In the Bi-Te binary phase diagram, the congruently melting point of binary compound is slightly shifted toward the Bi side of the Bi_2Te_3 composition. Consequently, a solid grown from a stoichiometric melt has a slightly Bi-rich composition and exhibits weak p-type conduction due to Bi_{Te} antisite acceptor defects, whose formation energy is lower than V_{Te} donor vacancies.[135] For Sb_2Te_3, even lower formation energy of Sb_{Te} antisite results in strong p-type conduction across its entire composition range. As a result, isovalent cation site alloying in $(Bi,Sb)_2Te_3$ enables a wide range of control of hole carrier concentration via regulating Sb_{Te} antisite defects. In contrast, Bi_2Se_3 has sufficiently low formation energy of V_{Se} vacancies, leading to n-type conduction.[134,136,137] Thus, anion site alloying in $Bi_2(Te,Se)_3$ with Se amounts exceeding 33%, where the concentration of anion vacancies surpasses that of antisite defects, can convert the conduction type from p-type to n-type, and the electron carrier concentration can be tuned by further alloying,[138–140] as shown in Fig. 3(a). Interestingly, alloying with Bi_2S_3 rapidly reduces the hole carrier concentration and induces the p-n transition at only about 4.3% substitution,[141–143] probably due to the lower formation energy of V_S vacancies.

The variation in thermal conductivity of p-type $(Bi,Sb)_2Te_3$ alloys has been well described using a mass contrast alloy scattering model.[130,144] However, this model does not fully explain the behavior of n-type $Bi_2(Te,Se)_3$ anion solid solution.[130,140,144,145] As shown in the variation of lattice thermal conductivity for $Bi_2(Te,Se)_3$ solid solutions [Fig. 3(b)], qualitative trends in lattice thermal conductivity within this system vary widely, but most studies report a global minimum near $Bi_2Te_{2.5}Se_{0.5}$. However, apparently different trends are observed between $0 < x < 1$ and $1 < x < 3$ in $Bi_2Te_{3-x}Se_x$. This difference is attributed to the site occupancy preference of the two inequivalent *Ch* sites upon alloying and the presence of an ordered compound at Bi_2Te_2Se, which divides the $Bi_2Te_{3-x}Se_x$ system into two parts: Bi_2Te_3-Bi_2Te_2Se and Bi_2Te_2Se-Bi_2Se_3.[144] This site selectivity has been linked to a reduction in bond angle strain due to anion size difference and the more electronegative Se occupying the site with the highest cation coordination.[146,147] In the composition range of $1 < x < 3$, the variation in lattice thermal conductivity can be explained solely by mass fluctuation effects since only one of the *Ch* sites changes occupancy. On the other hand, in the composition range of $0 < x < 1$, strain effects and/or changes in bonding must be considered to understand the changes in lattice thermal conductivity.[144]

The electronic transport properties and band structures of the $Bi_2(Te,Se)_3$ system have also been studied. The band structure of Bi_2Te_3 consists of conduction and valence band extrema with high valley degeneracy, while Bi_2Se_3 has a rather simple band structure with single carrier pockets at the zone-center [Fig. 3(c)].[144] Upon alloying, the band edge energies shift systematically, but this does not result in optimized thermoelectric performance. The weighted mobility monotonically decreases from 590 to 170 $cm^2\ V^{-1}\ S^{-1}$ from Bi_2Te_3 to Bi_2Se_3 likely due to a decrease in valley degeneracy and/or in the conduction

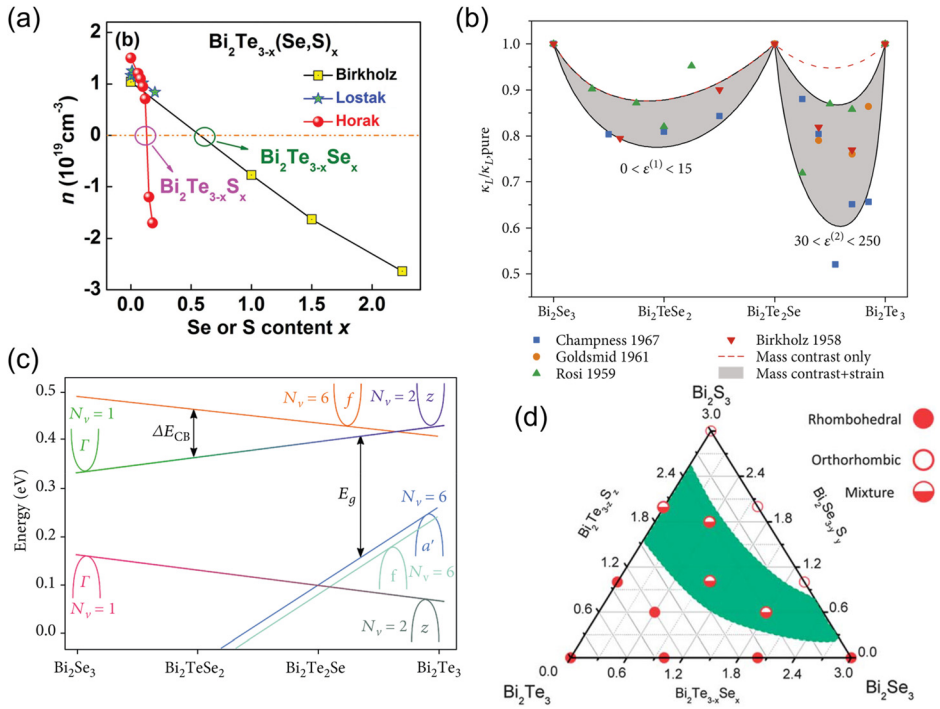

FIG. 3. (a) Room temperature carrier concentration of unidirectionally grown polycrystalline $Bi_2Te_{3-x}(Se/S)_x$ as a function of Se or S content, where positive and negative values of carrier concentration (n) correspond to hole and electron, respectively. The data are extracted from references named Birkholz,[140] Lostak,[142] and Horak.[141] (b) Experimental variation of lattice thermal conductivity (κ_L) for $Bi_2(Te,Se)_3$ alloys[130,140,145,151] together with the calculated ones using the model with mass contrast alone and with mass contrast and strain effects. (c) Band extrema responsible for the electronic transport in $Bi_2(Te,Se)_3$ alloys and their energy shift with changing the composition. (d) Phase diagram of pseudo-ternary Bi_2Te_3-Bi_2Se_3-Bi_2S_3 system. (a) Reproduced with permission from Zhu *et al.*, Adv. Sci. **3**, 1600004 (2016). Copyright 2016 Author(s), licensed under a Creative Commons Attribution (CC BY 4.0) license.[134] (b) and (c) Reproduced with permission from Witting *et al.*, Research **2020**, 4361703. Copyright 2020 Author(s), licensed under a Creative Commons Attribution (CC BY 4.0) license.[144] (d) Reproduced with permission from Liu *et al.*, Energy Environ. Sci. **6**(2), 552–560 (2013). Copyright 2013 The Royal Society of Chemistry.[149]

band anisotropy of each valley.[148] Thus, reported ZT values of n-type $Bi_2(Te,Se)_3$ (ranging from 1.0 to 1.2) are typically inferior to those of p-type $(Bi,Sb)_2Te_3$ (ranging from 1.4 to 1.8).[144]

The site selectivity at the *Ch* site upon alloying is also observed in $Bi_2(Te,S)_3$ alloys, but some reports indicate that phase separation occurs at Bi_2Te_2S and some other compositions.[147,149] This can be attributed to large bond angle strains inhibiting the formation of the ordered compound. As shown in Fig. 3(d), such phase separation occurs in the Bi_2Te_3-Bi_2Se_3-Bi_2S_3 pseudo-ternary system.[149] Some reports suggest that thermoelectric properties at wide temperature range can be improved through the phase separation, such as nanocomposite *Pnma* Bi_2SeS_2–*Pnnm* Bi_2SeS_2 ($ZT_{ave} = 0.72$ in the range of 323–773 K).[150]

2. PbCh, GeCh, and $AgSbCh_2$ (Ch = S, Se, Te)

PbCh-based materials with NaCl-type structure are known as one of the best thermoelectric materials with high ZT at mid-temperature range. To improve ZT of p-type PbCh, monovalent cation doping at Pb site has been extensively applied, such as Na-doping for PbTe[152–154] and PbSe,[154,155] K-doping for PbTe.[156,157] Some dopants are theoretically predicted to create resonant states in PbTe near the Fermi level,[158] and Tl-doping experimentally demonstrated the formation of a resonant state that significantly enhances thermoelectric properties.[6]

Pioneering work by Pei *et al.* demonstrated that an anion substitution of Se for Te site in PbTe allows to control the temperature at which the valence band maximum (VBM) at the L point and the second band along the Σ line converge.[8] Figure 4(a) shows the carrier pockets for PbTe in the first Brillouin zone, showing that the valley degeneracy of L and Σ bands is 4 and 8, respectively. As shown in Fig. 4(b), in $PbTe_{0.85}Se_{0.15}$, the band convergence of the two bands occurs at around 500 K, leading to the significant enhancement of thermoelectric properties ($ZT = 1.8$ at 850 K) due to the effectively increased valley degeneracy of 12. This finding not only prompted a reevaluation of the importance of anion site alloying in PbCh but also widely popularized the effectiveness of band engineering in thermoelectric materials.[111,123,159–165] The pseudo-ternary PbTe-PbSe-PbS system has also been explored to optimize p-type thermoelectric performance, as shown in Fig. 4(c).[164] The optimized ZT values around 1.9 have been obtained at the composition range of $x = 0.15$ to 0.25 in $(PbTe)_{1-2x}(PbSe)_x(PbS)_x$.

In contrast, for n-type PbCh, carrier doping through aliovalent anion site substitution has long been recognized as effective. Most commercially used n-type PbTe is doped with PbI_2.[166,167] Wang *et al.* revealed that anion substitutions are more suitable than cation

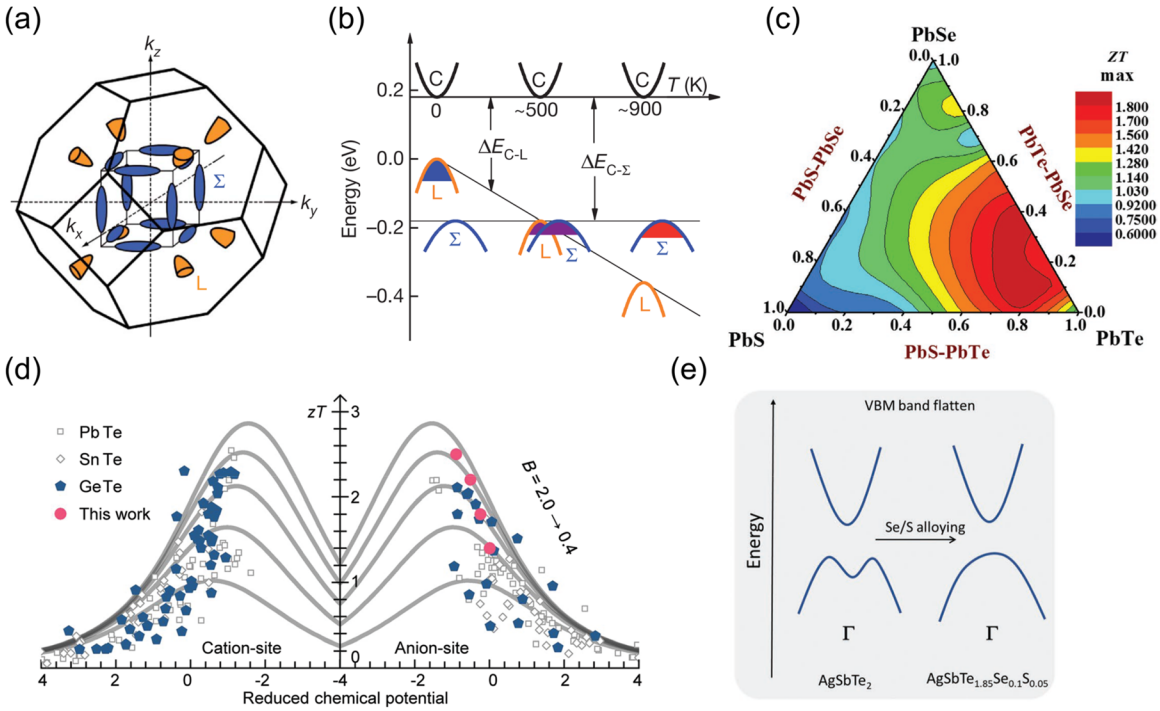

FIG. 4. (a) Hole carrier pockets at L point (orange) and along Σ line (blue) in the first Brillouin zone of PbTe, and (b) relative energy of valence band maxima and their shift with increasing temperature in $PbTe_{0.85}Se_{0.15}$. (c) Contour plot of *ZT* values of 2 mol. % Na-doped PbTe-PbSe-PbS pseudo-ternary alloys. (d) Comparison of *ZT* and the quality factor *B* of *M*Te (*M* = Pb, Sn, Ge) with cationic and anionic doping. (e) Schematic image of the band flattening at Γ point of $AgSbTe_2$ induced by anion site alloying. (a) and (b) Reproduced with permission from Pei *et al.*, Nature **473**(7345), 66–69 (2011).[8] Copyright 2011 Springer Nature. (c) Reproduced with permission from Qin *et al.*, Adv. Elect. Mater. **5**(12), 1900609 (2019). Copyright 2019 Wiley-VCH.[164] (d) Reproduced with permission from Li *et al.*, Adv. Funct. Mater. **32**, 2208579 (2022). Copyright 2022 Wiley-VCH.[175] (e) Reproduced with permission from Zhang *et al.*, Adv. Mater. **35**, e2208994 (2022). Copyright 2023 Wiley-VCH.[182]

substitutions for achieving high electron mobility in PbSe.[168] Since the conduction band edge of PbSe comprises Pb-*s* orbitals mostly, anion substitution can protect the charge carriers from disorder scattering by dopants. Recently, the concept of high-entropy alloying has been introduced to enhance the thermoelectric properties of both p-type and n-type PbCh.[169–171]

GeCh has recently attracted attention as potential Pb-free alternative to PbCh. GeTe has NaCl-type structure above around 700 K, and undergoes a structural phase transition to the low-temperature rhombohedral phase (*R*3*m*).[172] The anion site alloying in pseudo-binary GeTe-GeSe[173] and pseudo-ternary GeTe-GeSe-GeS[174] systems have been reported to effectively reduce the lattice thermal conductivity. Li *et al.* comprehensively studied the roles of anion site doping in GeTe from the viewpoint of chemical bonding and transport properties. Figure 4(d) summarizes the reported *ZT* of *M*Te (*M* =Pb, Sn, Ge) varying with the reduced chemical potential tuned by cation- or anion-site doping. It was revealed that less-explored anion-site doping is as effective as cation-site doping in improving the quality factor *B*, defined as

$$B = \left(\frac{k_B}{e}\right)^2 \frac{T}{\kappa_{lat}} \sigma_{E0}, \tag{1}$$

$$\sigma_{E0} = \frac{e(2m_e k_B T)^{\frac{3}{2}}}{3\pi^2\hbar^3} \mu_0 \left(\frac{m^*_{DOS}}{m_e}\right)^{3/2}, \tag{2}$$

where k_B is the Boltzmann constant, e is the electronic charge, μ_0 is the carrier mobility, $m^*_{DOS} = N_v^{2/3} m^*_b$ is the density of state effective mass, N_v is the band degeneracy, m^*_b is the effective mass of a single band, m_e is the electronic mass, and $\hbar$ is the Dirac constant. A significantly enhanced *ZT* value of 2.5 at 675 K was achieved by cationic Bi and anionic I co-doping on GeTe.[175]

$AgSbTe_2$ is known for its high thermoelectric properties in alloys such as the alloy with PbTe ($AgPb_{18+x}SbTe_{20}$), referred to as LAST,[41] and the alloy with GeTe known as TAGS, $(GeTe)_x(AgSbTe_2)_{1-x}$.[166] However, recent studies have shifted focus toward $AgSbTe_2$ itself, which has been shown to exhibit excellent performance on its own. $AgSbTe_2$ is stabilized in NaCl-type structure at RT, with Ag and Sb randomly occupying the cation sites.[176–179] Although the cation disorder is partly responsible for low lattice thermal conductivity, enhancing cation ordering has been identified as a key factor in achieving higher *ZT* values.[180,181] Zhang *et al.* reported that substituting Se and S for Te reduced the formation energy of Ag vacancies and stabilized $AgSbTe_2$ by inhibiting the formation of Ag_2Te impurity phase, which degraded the electronic properties.[182] Additionally, as shown in Fig. 4(e), density functional theory (DFT) calculations revealed that the anion site alloying can flatten the VBM at the zone center, contributing to a significant enhancement of the PF and *ZT* ($ZT_{max} = 2.3$ at 673 K). Recently, high-entropy alloying at anion sites in a related compound, $AgBiSe_2$, with S and Te has been reported to stabilize the cubic NaCl-type structure at RT, which was originally high-temperature phase above around 590 K.[183,184]

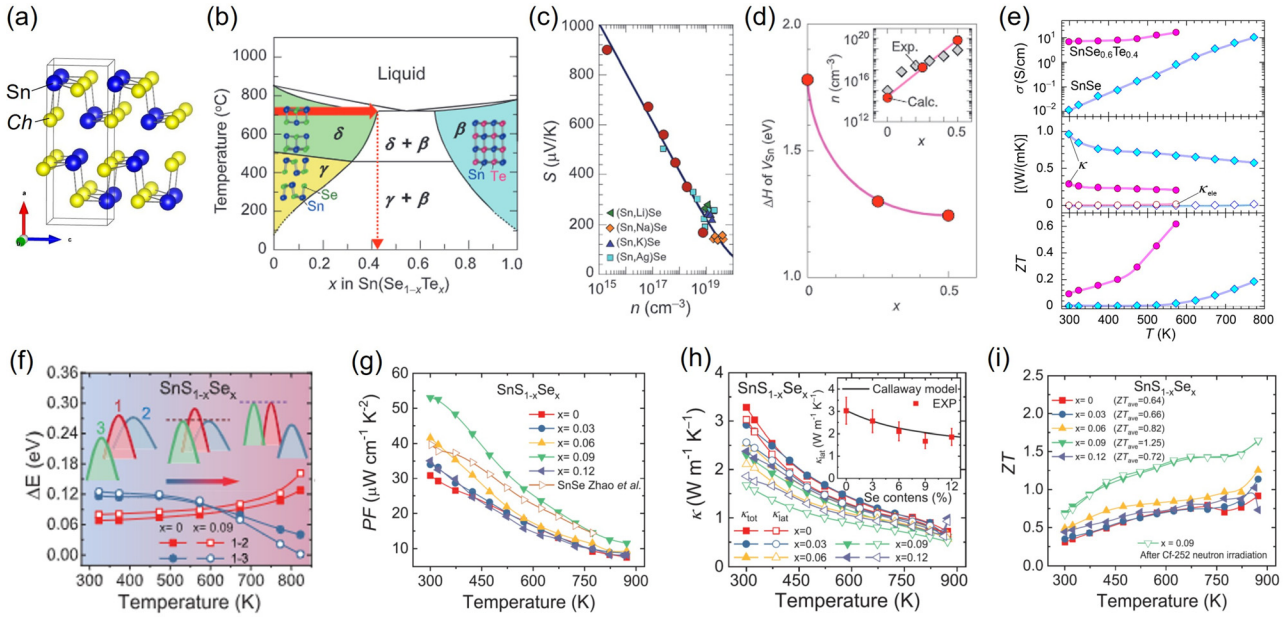

FIG. 5. (a) Schematic crystal structure of layered Sn*Ch* (*Ch* = S and Se). (b) Equilibrium phase diagram of SnSe−SnTe. (c) Seebeck coefficient (*S*) vs carrier concentration (*n*) for $Sn(Se_{1-x}Te_x)$ polycrystals, compared with those of alkali-doped SnSe. (d) Defect formation enthalpies (ΔH) of Sn vacancy (V_{Sn}) as a function of *x* in $Sn(Se_{1-x}Te_x)$. Inset shows the *x* dependence of *n* obtained from experimental measurement and theoretical estimation. (e) Temperature dependence of σ, κ, and *ZT* for SnSe and $SnSe_{0.6}Te_{0.4}$ polycrystals. (f) Temperature dependence of the energy gap (ΔE) between three separate valence bands VBM1,2,3 for SnS and $SnS_{0.91}Se_{0.09}$. (g)–(i) Temperature dependence of (g) PF, (h) κ, and (i) *ZT* for $Sn(S_{1-x}Se_x)$ crystals. (b)–(e) Reproduced with permission from He *et al.*, Adv. Sci. **9**, 2105958 (2022). Copyright 2022 Author(s), licensed under a Creative Commons Attribution (CC BY 4.0) license.[198] (f)–(i) Reproduced with permission from He *et al.*, Science **365**(6460), 1418–1424 (2019). Copyright 2019 AAAS.[202]

3. SnCh (Ch = S, Se, Te)

Sn*Ch* (*Ch* = S and Se) have received great attention as high *ZT* p-type thermoelectric materials due to their ultra-low κ_{lat} in single crystals[21,46,185] and polycrystals.[186] The SnS and SnSe adopt layered crystal structure (space group: *Pnma*) built from alternate stacking of 2-dimensional Sn−*Ch* layers [Fig. 5(a)]. The layered structure of Sn*Ch* is characterized by the stereochemically active lone pair state of Sn^{2+} $5s^2$, which does not form a covalent bond with *Ch* ions in the adjacent Sn−*Ch* layers along the stacking direction. The weak interatomic bonding between the Sn−*Ch* layers provides the strong anharmonicity and ultra-low lattice thermal conductivity. The pure SnS and SnSe exhibit p-type conduction, originating from the naturally formed acceptor-type Sn vacancy (V_{Sn}) defects.[187,188] The monovalent cations, such as alkali ions, Ag^+ ion, and Tl^+ ion, can increase the hole concentrations and realize high *ZT* in p-type SnS and SnSe.[189–197] On the other hand, there have been several reports on the solid solution of anions for thermoelectric performance enhancement. For example, isovalent Te^{2-} ion substitution at Se^{2-} site in SnSe polycrystals can achieve increasing σ and reducing κ simultaneously.[198] The solubility limit (*x*) of Te ion in the layered $Sn(Se_{1-x}Te_x)$ is very low under thermal equilibrium condition, because of the formation of counterpart cubic SnTe phase. On the other hand, it is possible to expand the *x* up to 0.4 in $Sn(Se_{1-x}Te_x)$ by high-temperature solid-state reaction and rapid thermal quenching from 973 K (700 °C) to RT, as indicated by red arrow in the phase diagram of SnSe-SnTe [Fig. 5(b)].[199–201] Usually, isovalent ion substitution does not generate carriers, while the hole concentration increases from $1.0 \times 10^{15}\,cm^{-3}$ of pure SnSe to $2.0 \times 10^{18}\,cm^{-3}$ of $Sn(Se_{0.6}Te_{0.4})$. Figure 5(c) compares the Seebeck coefficient as a function of hole concentration (*n*) at RT. The Seebeck coefficient decreases with increasing *n*, similar to Li^+, Na^+, K^+, and Ag^+ doped SnSe bulks.[192] Defect calculations clarified that the formation enthalpy (ΔH) of V_{Sn} becomes lower with increasing Te concentration [Fig. 5(d)]. The large-size Te ion in SnSe forms weak Sn−Te bonds. The Sn−Te bond is easily dissociated, and a high density V_{Sn} is formed in the structure, leading to a high *n* and high σ in $Sn(Se_{1-x}Te_x)$. In addition, the weak Sn−Te bonds in $Sn(Se_{1-x}Te_x)$ reduce the phonon frequency and enhance the phonon scattering, resulting in the large reduction of lattice thermal conductivity of less than one-third at RT. The simultaneous σ increase and thermal conductivity reduction demonstrate the *ZT* enhancement in $Sn(Se_{1-x}Te_x)$ [Fig. 5(e)].

In addition, σ and PF enhancement by band manipulation and lattice thermal conductivity reduction were reported in $Sn(S_{1-x}Se_x)$ single crystal.[202] SnS possesses three separate valence bands (VBM1,2,3) and their energy offsets change as a function of temperature [Fig. 5(f)]. The energy level rise of light VBM3 band results in a strong convergence with VBM1, while the heavier band VBM2 shifts to deeper energy. The Se substitution in SnS decreases the energy offsets between the sharp VBM1 and VBM3, contributing to the enhancement of carrier mobility. The band manipulation enhances the PF from ~30 $\mu W\,cm^{-1}\,K^{-2}$ of Na-doped SnS to ~53 $\mu W\,cm^{-1}\,K^{-2}$ of Na-doped $SnS_{0.91}Se_{0.09}$ at 300 K [Fig. 5(g)]. The PF of Na-doped $SnS_{0.91}Se_{0.09}$ exceeds those of the other thermoelectric materials in the

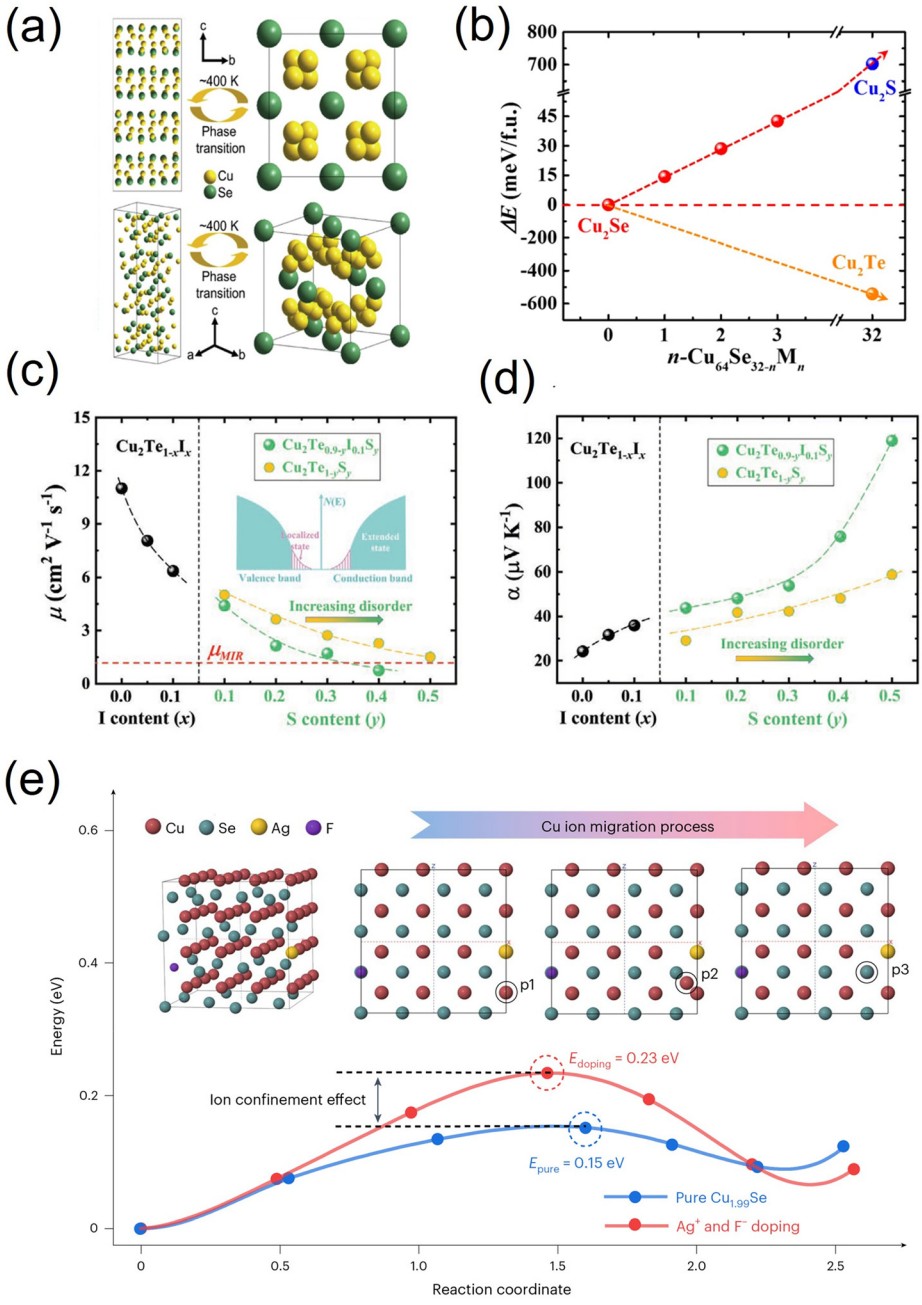

FIG. 6. (a) Crystal structure of β-Cu_2Se. (b) Bonding energy of $Cu_{64}Se_{32-n}M_n$ (M = S, Te) as a function of M content. (c) Carrier mobility and (d) Seebeck coefficient as a function of I content or S content for $Cu_2Te_{1-x}I_x$, $Cu_2Te_{0.9-y}I_{0.1}S_y$, and $Cu_2Te_{1-y}S_y$ at 300 K. The inset in (c) shows a schematic of the localized electronic states and extended electronic states, and the red dashed line denotes the carrier mobility at MIR limit, μ_{MIR}. (e) Energy landscapes of the pure and Ag and F co-doped $Cu_{1.99}Se$ during the Cu ion migration. (a) Reproduced with permission from Liu *et al.*, Nano Today **35**, 100938 (2020). Copyright 2020 Elsevier Ltd.[212] (b) Reproduced with permission from Zhao *et al.*, Chem. Mater. **29**(15), 6367–6377 (2017). Copyright 2017 American Chemical Society.[210] (c) and (d) Reproduced with permission from Zhao *et al.*, Adv. Mater. **34**(19), e2108573 (2022). Copyright 2022 Wiley-VCH.[215] (e) Reproduced with permission from Hu *et al.*, Nat. Mater. **23**(4), 527–534 (2024). Copyright 2024 Springer Nature.[221]

group IV–VI compounds in the range from 300 to 523 K. In addition, the Se substitution effectively reduces the lattice thermal conductivity of SnS [Fig. 5(h)] because of the optical phonon softening by Se substitution and further coupling with acoustic branches. The simultaneous PF enhancement and lattice thermal conductivity reduction realize the ZT enhancement in the Na-doped $SnS_{0.91}Se_{0.09}$ crystals with maximum ZT (ZT_{max}) of ~1.6 at 873 K and an average ZT (ZT_{ave}) of ~1.25 at 300 to 873 K [Fig. 5(i)].

4. Cu_2Ch, Ag_2Ch, and AgCuCh (Ch = S, Se, Te)

Numerous phases are known in binary Cu-based chalcogenides, with some exhibiting high thermoelectric performance. Among them, Cu_2Ch-based materials have gained significant attention over the past decade, particularly since the discovery of ultra-low lattice thermal conductivity caused by "liquid-like" behavior of mobile Cu ions in high-temperature superionic phase of β-$Cu_{2-x}Se$ [Fig. 6(a)].[22] The

Cu-deficient $Cu_{2-x}Se$ undergoes structural transition from a low-temperature α-phase to the high temperature β-phase. The β-phase has Se atoms in a simple face-centered cubic (fcc) sublattice while the superionic Cu ions are kinetically disordered throughout the structure. High p-type peak ZT values around or above 2 have been reported for Cu_2Ch-based materials in various studies.[22,203–214] The bonding energy in Cu_2Se can be tuned by S or Te substitution for Se site [Fig. 6(b)], enabling wide range control of formation energy of Cu vacancies and hole carrier concentration.[210] Co-alloying with I and S in Cu_2Te introduces several intriguing effects: (i) I-doping reduces the hole carrier concentration, and (ii) the anion sublattice with highly size-mismatched S/Te quenches the originally mobile Cu sublattice.[215] This quenching alters the electronic states from itinerant to localized, where the carrier mobility approaches the Mott–Ioffe–Regel (MIR) limit, as shown in Fig. 6(c). This change in the conduction mechanism enhances the Seebeck coefficient despite the carrier concentration remaining unchanged [Fig. 6(d)]. Similar enhancements in thermoelectric properties observed near electron localization and/or the MIR limit have been reported for some other thermoelectric materials.[180,181,211,216–220] Very recently, an ultrahigh ZT value of 3.0 at 1050 K was reported for Ag and F co-doped $Cu_{1.99}Se$.[221] The co-doping of Ag, with larger ionic radius than Cu, and F, with high electronegativity, modulates the chemical bonding, resulting in enhanced thermal stability and restriction of Cu-ion migration [Fig. 6(e)] as well as improved thermoelectric properties.

Ag-chalcogenides, Ag_2Ch, exhibit similar liquid-like behavior in their high-temperature superionic phases. As shown in Fig. 7(a), Ag_2Ch adopts various crystal structures depending on temperature. All three compounds undergo one or more phase transitions upon heating, and Ag ions become highly mobile in the cubic structures at high temperatures. Unlike Cu_2Ch, most Ag_2Ch compounds exhibit n-type conduction and high electron mobility, which is two orders of magnitude higher than the hole mobility of p-type Cu_2Ch. High peak ZT values around unity have been reported for Ag_2Se and Ag_2Te at around 300–400 K, due to their small band gaps of 0.1–0.2 eV.[209,222–225] Moreover, following the striking discovery of ductility at RT in α-Ag_2S [Fig. 7(b)],[226] the Ag_2Ch family has been recognized as promising candidates for high-performance flexible inorganic thermoelectric materials. As shown in Fig. 7(c), both thermoelectric and mechanical properties can be optimized by adjusting the anionic composition in Ag_2Ch.[225–236] Moderately high ZT values at RT have been achieved in some compositions such as $Ag_2S_{0.5}Se_{0.5}$ ($ZT = 0.25$),[228] $Ag_2S_{0.5}Te_{0.5}$ ($ZT = 0.6$),[231] and $Ag_2S_{0.5}Se_{0.45}Te_{0.05}$ ($ZT = 0.44$),[228] while maintaining plasticity. Additionally, as a p-type counterpart to these ductile thermoelectric semiconductors, AgCuCh compounds have also been recently investigated.[237–239] As shown in Fig. 7(d), tuning the composition within the pseudo-ternary AgCuSe-AgCuS-AgCuTe system can switch the conduction type, and the maximum p-type ZT value of 0.45 at 300 K is achieved at the composition $(AgCu)_{0.998}Se_{0.22}S_{0.08}Te_{0.7}$.[237]

Several reports have indicated that anion substitutions with high concentration such as Cu_2(S,Te) and Ag_2(S,Te), where the relative atomic size difference between anions exceeds 15%, have been successfully synthesized.[211,215,225] However, the well-known Hume-Rothery (H-R) rules suggest that a large atomic size mismatch (>15%) and significant electronegativity difference between solute and solvent atoms typically lead to phase separation.[240,241] Zhao *et al.* proposed that the diffusion coefficient should be added as a new dimension to the classic H-R rules. Solid solutions with large atomic size mismatch between anions (Δr) and diffusion coefficient mismatch between cations and anions (ΔD) lead to a single phase distinct from the original ones [Fig. 7(e)]. This new phase of matter, termed a "meta-phase," possesses atomic structure and properties distinct from conventional solid solutions.[218] Since the meta-phase can accommodate multiple anions with large difference in atomic size, which have been dismissed according to the classic H-R rule, it could offer a new paradigm for optimizing thermoelectric properties across a wide range of material systems.

5. Pnictides and tetrelides: $Mg_3(Sb,Bi)_2$, skutterudites, and Mg_2X (X = Si, Ge, Sn)

Across pnictides and tetrelides, Zintl phases are prevalent and have played a notable role in the discovery of candidate thermoelectric materials. Zintl phases often feature complex crystal structures composed of anionic frameworks with intricate covalent bonding networks and cations donating electrons, and these have been studied as potential thermoelectric materials for a long time.[242,243] In some systems, local structural units composed of electropositive and electronegative elements accept electrons from more electropositive constituents, such that the resulting network can be regarded as a polyanionic covalent framework; such cases are also often described as Zintl phases. It should be noted that the term "Zintl phase" is being used in a somewhat broader sense than its original definition. The complex structures with coexistence of ionic and covalent characters frequently lead to very low lattice thermal conductivity. Mg_3Sb_2 contains alternating layers of Mg^{2+} and $[Mg_2Sb_2]^{2-}$ with covalent polyanionic Mg–Sb framework, and is widely recognized as a Zintl phase in the thermoelectrics literature. Mg_3Sb_2 contains alternating layers of Mg^{2+} and $[Mg_2Sb_2]^{2-}$ with covalent polyanionic Mg–Sb framework and is widely recognized as a Zintl phase in the thermoelectrics literature. Tamaki *et al.* demonstrated that excess Mg suppresses the formation of acceptor Mg vacancies in Mg_3Sb_2, leading to excellent n-type thermoelectric properties.[55] In addition, substituting the anion site of Bi for Sb effectively reduces the lattice thermal conductivity [Fig. 8(a)] leading to a high ZT value of 1.5 at 716 K. Following this finding, the n-type $Mg_3(Sb,Bi)_2$-based materials have been extensively investigated as promising candidates for practical thermoelectric applications.[36–38,56–58,244–249] The anionic alloying also has significant effects on the electronic band structure. As shown in Fig. 8(b), the other end compound Mg_3Bi_2 is a semimetal, and the bandgap and the band effective mass at the conduction band minimum (CBM) decrease monotonically with increasing Bi content in $Mg_3(Sb,Bi)_2$.[244,247,250] Consequently, the temperature at which the thermoelectric performance is optimized can be controlled by adjusting Bi content. For instance, $ZT = 1.1$ at 300 K is obtained for Bi-rich composition ($Mg_{3.2}Bi_{1.998-x}Sb_xTe_{0.002}Cu_{0.005}$, $x = 0.4$)[38] while $ZT = 2.0$ at 723 K is obtained for Sb-rich composition ($Mg_{3.2}In_{0.005}Sb_{1.5}Bi_{0.49}Te_{0.01}$).[58]

Skutterudites, such as $CoSb_3$, are typical inclusion compounds featuring cages of about two angstroms within their unit cells, into which guest atoms can be inserted. Filled skutterudites, denoted as $M_xCo_4Sb_{12}$, have been extensively studied as ideal PGEC thermoelectric materials because the inserted guest atoms act as rattlers that effectively scatters long-wavelength phonons without sacrificing electrical properties.[251–254] In most cases, the guest atom is electropositive, as the interaction between the cationic guest and anionic framework stabilizes the structure of filled skutterudites. However, Duan *et al.* reported that some electronegative guest atoms were successfully inserted into $CoSb_3$ [Fig. 8(c)].[255] The electronegativity difference

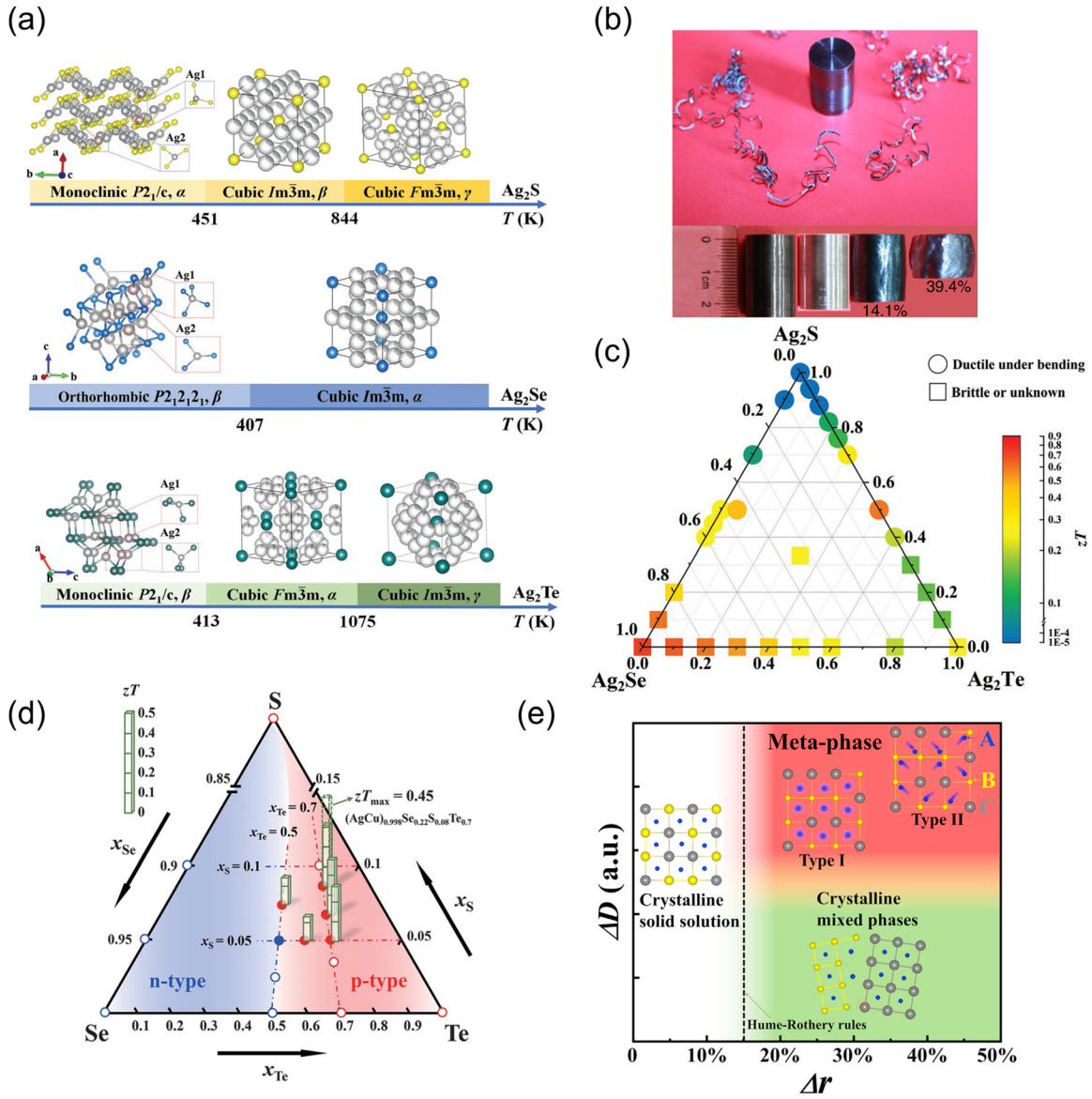

FIG. 7. (a) Crystal structures variation with varying temperature for Ag_2Ch (Ch = S, Se, Te). (b) Compression test of the α-Ag_2S cylinder suggesting that a significant compression as shown in the bottom part. The thin and winding wires shown at the upper part are obtained during the lathing. (c) Room-temperature ZT values and plastic deformability of Ag_2Ch-based solid solutions. Circles and squares represent ductile and brittle compositions, respectively. (d) Room-temperature ZT and conduction type variation of the pseudo-ternary AgCuCh-based solid solutions. Filled and hollow circles represent ductile and brittle compositions, respectively. (e) Schematic diagram of the condition of formation of meta-phase. Solid solutions with large atomic size mismatch between anions (Δr) and diffusion coefficient mismatch between cations and anions (ΔD) lead to a formation of meta-phase, which is beyond the classic Hume-Rothery rule. (a) and (c) Reproduced with permission from Wei *et al.*, Adv. Mater. **35**(1), e2110236 (2023). Copyright 2023 Wiley-VCH.[225] (b) Reproduced with permission from Shi *et al.*, Nat. Mater. **17**(5), 421–426 (2018). Copyright 2018 Springer Nature.[226] (d) Reproduced with permission from Shi *et al.*, Nat. Mater. **17**(5), 421–426 (2018). Copyright 2022 AAAS.[237] (e) Reproduced with permission from Zhao *et al.*, Matter **5**(2), 605–615 (2022). Copyright 2021 Elsevier Ltd.[218]

between Sb and the guest atom determines whether the interaction between them is ionic or covalent. The strongly covalent guest-host interactions observed for the electronegative guests (S, Se) result in a unique localized "cluster vibration," which is not observed for the conventional electropositive guest. Such cluster vibration effectively reduces the lattice thermal conductivity of $CoSb_3$ in a different manner from the electropositive guest. The average ZT at the range of 550–850 K is 1.3 for $S_{0.26}Co_4Sb_{11.11}Te_{0.73}$, making the electronegative guest as promising as the electropositive guest for practical applications at intermediate temperatures.

Cheap, earth-abundant, and environmentally benign Mg_2Si-based materials have been regarded as an attractive alternative to

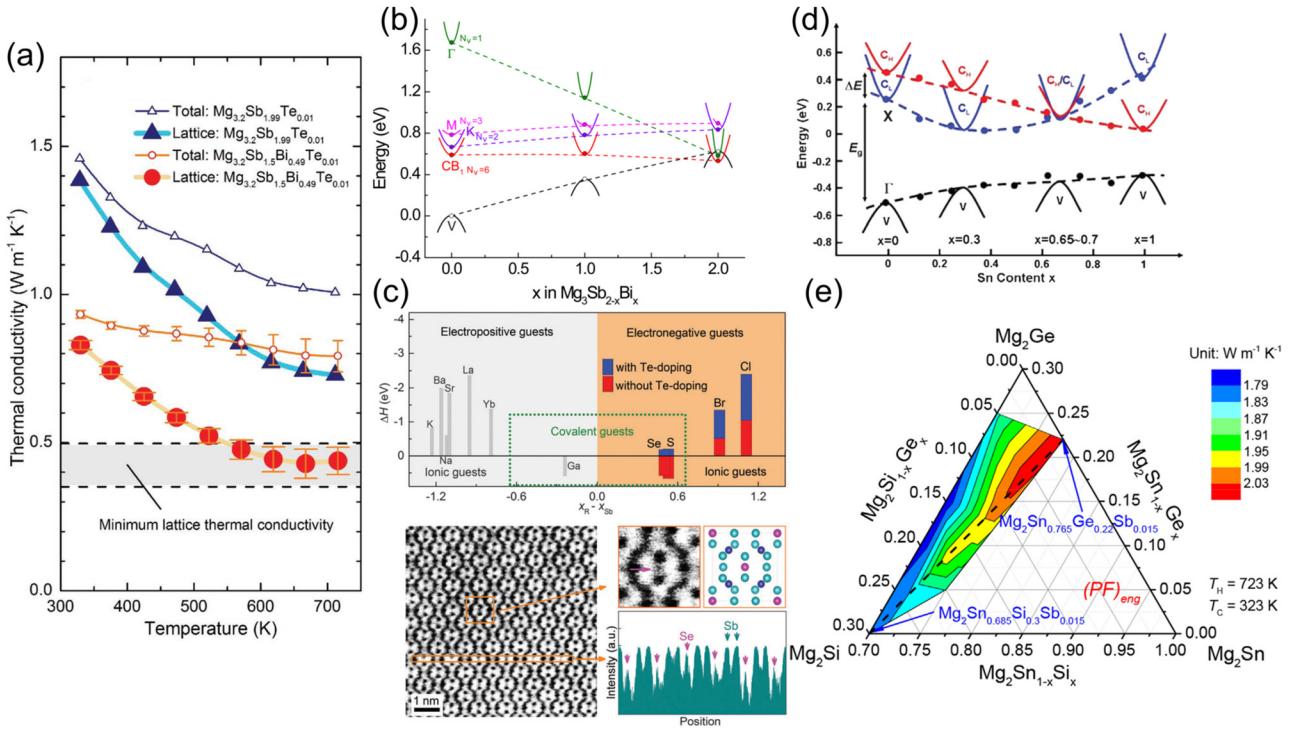

FIG. 8. (a) Temperature dependence of thermal conductivity (open symbols) and lattice thermal conductivity (filled symbols) for $Mg_{3.2}Sb_{1.99}Te_{0.01}$ and $Mg_{3.2}(Sb,Bi)_{1.99}Te_{0.01}$. (b) Relative energy shift in the band extrema for $Mg_3Sb_{2-x}Bi_x$ solid solutions with varying Bi content. (c) (Top) Formation enthalpies of the guest atom insertion into $CoSb_3$ with respect to electronegativity difference between Sb and the guest atom ($x_R - x_{Sb}$), and (bottom) ABF-STEM image of Se-filled $CoSb_3$ along the [100] direction and an intensity profile. (d) Relative energy shift in the band extrema for $Mg_2Si_{1-x}Sn_x$ solid solutions with varying Sn content. (e) Contour plot of the engineering power factor $(PF)_{eng}$ in the pseudo-ternary Mg_2Si-Mg_2Ge-Mg_2Sn system. (a) Reproduced with permission from Tamaki *et al.*, Adv. Mater. **28**(46), 10182–10187 (2016). Copyright 2016 Wiley-VCH.[55] (b) Reproduced with permission from J. Zhang and B. B. Iversen, J. Appl. Phys. **126**(8), 085104 (2019). Copyright 2019 AIP Publishing.[250] (c) Reproduced with permission from Duan *et al.*, Energy Environ. Sci. **9**(6), 2090–2098 (2016). Copyright 2016 The Royal Society of Chemistry.[255] (d) Reproduced with permission from Liu *et al.*, Phys. Rev. Lett. **108**(16), 166601 (2012). Copyright 2012 American Physical Society.[53] (e) Reproduced with permission from Mao *et al.*, Acta Mater. **103**, 633–642 (2016). Copyright 2016 Elsevier Ltd.[257]

widely used state-of-the-art thermoelectric materials. Liu *et al.* revealed that the light and heavy conduction bands converge at the composition of $x = 0.65$–0.7 in $Mg_2Si_{1-x}Sn_x$ [Fig. 8(d)], leading to a significant enhancement of the PF.[53] Similarly, the solid solutions $Mg_2Sn_{1-x}Ge_x$ also offer a search space for achieving the band convergence, and an extraordinary high PF of 55 μW cm^{-1} K^{-2} and ZT of 1.4 were achieved at $x = 0.25$.[54] Figure 8(e) shows the contour of engineering power factor, $(PF)_{eng}$, in the pseudo-ternary Mg_2Si-Mg_2Ge-Mg_2Sn system. The $(PF)_{eng}$ and an engineering figure of merit, $(ZT)_{eng}$, are proposed to predict reliably and accurately the efficiency of materials at a large temperature difference between hot and cold sides, where the conventional ZT and PF at a specific temperature are supposed to fail.[256] Mao *et al.* characterized the $(PF)_{eng}$ along the line between $Mg_2Si_{0.3}Sn_{0.7}$ and $Mg_2Sn_{0.78}Ge_{0.22}$ in the pseudo-ternary Mg_2Si-Mg_2Ge-Mg_2Sn system, though significant enhancement was not achieved for the intermediate compositions [Fig. 8(e)].[257] The $Mg_2Si_{1-x}Sn_x$ has been proposed as an aforementioned meta-phase due to the large atomic size mismatch between Si and Sn.[218]

In addition to $Mg_3(Sb,Bi)_2$, there are numerous Zintl phase pnictides being studied as thermoelectric materials. However, reports on tuning the structure and thermoelectric properties through elemental substitution at the anion sites are very scarce.[258,259] Isovalent and/or aliovalent substitutions at the anion sites, while preserving Zintl–Klemm electron counting rule, represent promising routes to control crystal chemistry and thermoelectric properties in this class of materials.

6. Oxides

Following the discovery of high p-type thermoelectric performance in single-crystalline layered cobalt oxides, Na_xCoO_2[260] and $Ca_3Co_4O_9$,[261] oxide thermoelectric materials have been extensively explored as stable high-temperature applications. Perovskite oxide $SrTiO_3$ has also been investigated for its high n-type PF at RT, ranging from 20 to 30 μW cm^{-1} K^{-2}.[262–264] However, its high lattice thermal conductivity ~10 W m^{-1} K^{-1} limits its practical applications, prompting many efforts to reduce it. He *et al.* revealed that an anionic substitution of H^- for O^{2-} was particularly effective in reducing the lattice thermal conductivity of $SrTiO_3$, compared with conventional La-doped $SrTiO_3$ [Fig. 9(a)].[265] Although the mass difference effect between H and O on phonon scattering is small in $SrTiO_{3-x}H_x$ [inset of Fig. 9(b)], the H^- substitution provides significant local structure

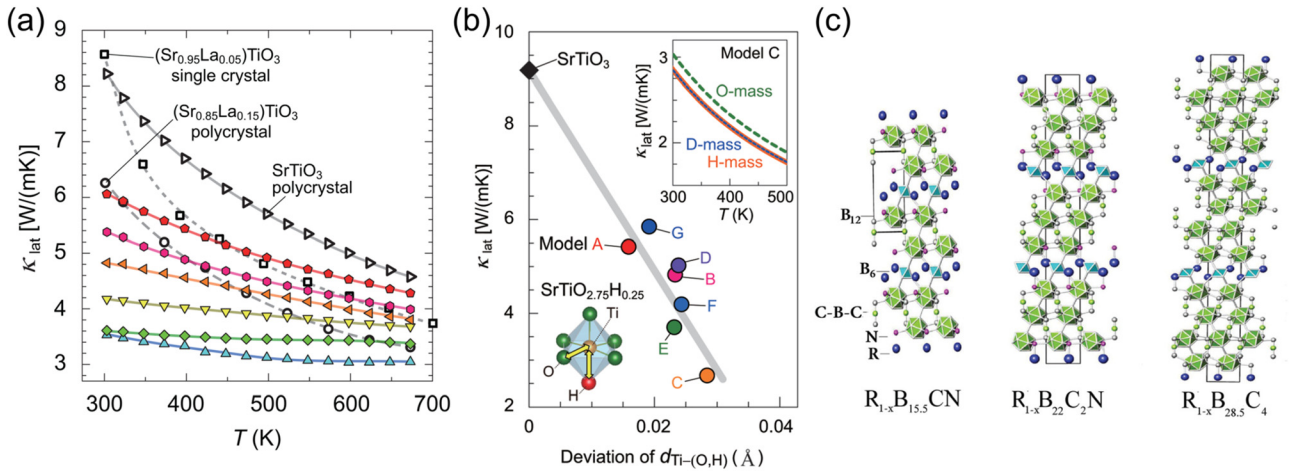

FIG. 9. (a) Temperature (T) dependence of the lattice thermal conductivity (κ_{lat}) for $SrTiO_{3-x}H_x$ bulks with $x = 0.057$–0.216. Those of $(Sr_{0.95}La_{0.05})TiO_3$ single crystal and $(Sr_{0.85}La_{0.15})TiO_3$ polycrystal are also shown for comparison. (b) Relationship between the calculated κ_{lat} at 300 K and the deviations of Ti–(O,H) bond lengths for seven $SrTiO_{2.75}H_{0.25}$ hypothetical structure models. Inset shows the calculated κ_{lat} as a function of T for $SrTiO_{2.75}H_{0.25}$ model with different virtual ion masses (H, D, and O ion masses). (c) Crystal structures of homologous rare earth borocarbonitride and borocarbide series with B_{12} icosahedra and B_6 octahedra. (a) and (b) Reproduced with permission from He *et al.*, Adv. Funct. Mater. **33**(28), 2213144 (2023). Copyright 2023 Wiley-VCH.[265] (c) Reproduced with permission from Mori *et al.*, Dalton Trans. **43**(40), 15048–15054 (2014). Copyright 2014 The Royal Society of Chemistry.[276]

distortion arising from the different chemical bond characteristics of the strong Ti–O bond and the weak Ti–H bond in Ti–(O,H) octahedra. The distributed Ti–(O,H) bond lengths strongly enhance the phonon scattering [Fig. 9(c)], which results in the significant reduction of lattice thermal conductivity from 8.2 to 3.5 W m^{-1} K^{-1}. In addition, the PF of polycrystalline oxide thermoelectric materials is often limited by low σ across the grain boundaries with low carrier concentration. On the other hand, the $SrTiO_{3-x}H_x$ realizes the single-crystal-like electron transport, resulting in higher PF, leading to $ZT = 0.11$ at RT and 0.22 at 657 K.[266] The H^- concentration is optimized in $SrTiO_{3-x}H_x$ epitaxial films and the maximum $ZT = 0.14$ at RT is obtained at H^- concentration of 1.2×10^{21} cm^{-3}.[267] The hydrogen doping approach would be promising to realize low κ_L and high PF in oxides.

7. Boron-rich cluster compounds

Some boron-based materials are regarded as good candidates for high-temperature thermoelectric applications, such as topping cycles in thermal power plants, due to their high melting points and chemical stability at high temperatures.[268] In B-rich metal borides, boron tends to form complex, electron-deficient clusters, such as B_6 octahedra,[269] B_{12} cuboctahedra,[270] and B_{12} icosahedra,[269] and metals provide electrons to stabilize the electron-deficient boron cluster network structures.[271] Boron carbide is known for its good p-type thermoelectric performance at high temperatures.[272–274] N-type conduction has been achieved in some rare earth borocarbides (*R*-B-C, *R*: rare earth)[275,276] and borocabonitrides (*R*-B-C-N),[275,277] which incorporate more electronegative C and N than B into the covalent network. Figure 9(c) shows the crystal structure of the rare earth borocarbides and borocabonitrides series sharing the same local structures of B_{12} icosahedra and B_6 octahedra, which are homologous to boron carbide B_4C. Although the absolute values of the Seebeck coefficients in these n-type compounds are relatively small, a significant enhancement of both electrical conductivity and the Seebeck coefficient in $YB_{22}C_2N$ by a combination of carrier doping and nanocomposite effects has been reported.[278]

B. Mixed-anion compounds with homoleptic polyhedra

Mixed-anion compounds containing multiple anions with contrasting ionic and covalent bonding characteristics to cations tend to form complex crystal structures, characterized by the coexistence of bonds with varying degrees of ionicity and covalency within a single phase, which can sometimes result in separation into distinct structural blocks. The most representative case is a layered oxychalcogenide, BiCuOSe. BiCuOSe adopts layered crystal structure, which possesses the alternate stacks of Bi_2O_2 layers and Cu_2Se_2 layers. The O and Se anions do not mix with each other, but form separate layers with homoleptic O-Bi_4 and Cu-Se_4 polyhedra. Therefore, such oxychalcogenides naturally form superlattice structure consisting of widegap insulating oxide layer and highly conducting chalcogenide layer. The layered structure can lead to a highly anisotropic electronic band structure, resulting in sharp density of states around Fermi level and the large Seebeck coefficients. In addition, the layered structures with chemically different types of layers possess anisotropic chemical-bond contrast produced by weak inter-layer bonds and strong in-layer bonds. Such imbalances in chemical bonding strongly enhance the lattice anharmonicity and phonon scattering, resulting in the low lattice thermal conductivity. After the demonstration of high $ZT = 0.76$ in BiCuOSe with low lattice thermal conductivity,[279] the ZT has been improved to ~1.5 at 873 K.[280] Concurrently, analogous layered Cu-based oxychalcogenides, Ag-based oxychalcogenides, and Bi-based oxy(fluoro)chalcogenides, have been investigated as potential high performance thermoelectric materials. Tables I and II summarize the reported thermal conductivity and thermoelectric properties for mixed-anion layered compounds. This section provides an overview of

TABLE I. Summary of lattice thermal conductivity (κ_{lat}) of mixed-anion layered compounds at room temperature.

Material		κ_{lat} (W m^{-1} K^{-1})	Reference
BiCuOSe	Expt. (Poly.)	0.87	311
	Calc.	0.46 ⊥ layer (*c*-axis)	345
		1.70 ∥ layer (*ab*-axis)	
BiCuOS	Expt. (Poly.)	1.10	323
	Calc.	0.41 ⊥ layer (*c*-axis)	401
		1.10 ∥ layer (*ab*-axis)	
BiCuOTe	Expt. (Poly.)	0.50	324
	Calc.	0.14 ⊥ layer (*c*-axis)	401
		0.44 ∥ layer (*ab*-axis)	
LaCuOSe	Expt. (Poly.)	2.10	316
	Calc.	0.18 ⊥ layer (*c*-axis)	317
		2.51 ∥ layer (*ab*-axis)	
BiAgOSe	Expt. (Poly.)	0.62	345
	Calc.	0.22 ⊥ layer (*c*-axis)	345
		1.29 ∥ layer (*ab*-axis)	
BiAgOS	Calc.	0.20 ⊥ layer (*c*-axis)	402
		2.41 ∥ layer (*ab*-axis)	
BiAgOTe	Calc.	0.10 ⊥ layer (*c*-axis)	402
		0.73 ∥ layer (*ab*-axis)	
BaCuSeF	Calc.	1.18 ⊥ layer (*c*-axis)	327
		1.86 ∥ layer (*ab*-axis)	
BaCuTeF	Calc.	0.76 ⊥ layer (*c*-axis)	327
		1.30 ∥ layer (*ab*-axis)	
BaAgSeF	Calc.	1.22 ⊥ layer (*c*-axis)	327
		1.58 ∥ layer (*ab*-axis)	
BaAgTeF	Calc.	0.75 ⊥ layer (*c*-axis)	327
		0.98 ∥ layer (*ab*-axis)	
$Bi_2YO_4Cu_2Se_2$	Expt. (Poly.)	1.8	332
$Bi_2DyO_4Cu_2Se_2$	Expt. (Poly.)	1.13	329
$Sr_2MnCu_2O_2Te_2$	Expt. (Poly.)	1.41	336
$Sr_2CoCu_2O_2Te_2$	Expt. (Poly.)	1.72	336
Sr_2CuInO_3S	Expt. (Poly.)	0.73	338
$SrOCuBiSe_2$	Expt. (Poly.)	1.0	341
$SrOCuSbSe_2$	Expt. (Poly.)	1.0	339
$LaOBiS_2$	Expt. (Poly.)	1.85	373
LaOBiSSe	Expt. (c-axis textured poly.)	0.77 ⊥ layer (*c*-axis)	374
		1.20 ∥ layer (*ab*-axis)	
$LaOBiSe_2$	Expt. (Poly.)	1.37	379
$LaOSbSe_2$	Expt. (Poly.)	1.50	377
$CeOSbSe_2$	Expt. (Poly.)	0.80	377
$SrFBiS_2$	Expt. (Poly.)	2.51	375
$Bi_4O_4S_3$	Expt. (Poly.)	3.99	380
$LaOPbBiS_3$	Expt. (Poly.)	4.21	369
Bi_2O_2Se	Expt. (Poly.)	1.1	382
Bi_2O_2Se	Expt. (Single cryst.)	2.0 ∥ layer (*ab*-axis)	383
Bi_2O_2Se	Calc.	0.82 ⊥ layer (*c*-axis)	384
		1.32 ∥ layer (*ab*-axis)	
Bi_2O_2S	Calc.	0.4 ⊥ layer (*c*-axis)	396

TABLE I. (*Continued.*)

Material		κ_{lat} (W m^{-1} K^{-1})	Reference
		0.8 ‖ layer (*ab*-axis)	
Bi_2O_2Te	Expt. (Poly.)	0.91	397

TABLE II. Summary of thermoelectric properties (E_g: bandgap, *ZT*: dimensionless figure of merit, PF: power factor, *T*: temperature, *S*: Seebeck coefficient, σ: electronic conductivity, κ: total thermal conductivity) experimentally reported for mixed-anion layered compounds.

Material		Carrier type	E_g (eV)	*ZT*	PF (μW cm^{-1} K^{-2})	*T* (K)	*S* (μV K^{-1})	σ (S cm^{-1})	κ (W m^{-1} K^{-1})	Reference
BiCuOS	Poly.	p-type	1.1	0.05	0.50	700	545	1.67	0.68	323
$Bi_{0.95}Pb_{0.05}CuOS$	Poly.	p-type	N/A	0.2	2.05	700	345	17.2	0.72	323
BiCuOSe	Poly.	p-type	0.8	0.38	2.02	873	+380	14	0.46	279
$Bi_{0.925}Sr_{0.075}CuOSe$	Poly.	p-type	N/A	0.76	5.47	873	+223	110	0.63	279
$Bi_{0.875}Ba_{0.125}CuOSe$	*c*-axis textured poly.	p-type	N/A	1.34	7.53	923	+185	220	0.52	290
$Bi_{0.88}Ca_{0.06}Pb_{0.06}CuOSe$	Poly.	p-type	N/A	1.46	8.70	873	+229	166	0.52	280
BiCuOTe	Poly.	p-type	0.2	0.66	7.08	673	+181	216	0.72	403
$Bi_2YO_4Cu_2Se_2$	Poly.	p-type	0.3 (calc.)	0.06	0.62	873	+62	160	0.95	332
$Bi_2DyO_4Cu_2Se_2$	Poly.	p-type	0.04	0.27	2.96	923	+97	315	1.03	329
$Sr_2MnCu_2O_2Te_2$	Poly.	p-type	0.85	0.007	0.10	770	+64	25	1.12	336
$Sr_2CoCu_2O_2Te_2$	Poly.	p-type	1.50	0.045	0.70	770	+122	47	1.20	336
$SrOCuBiSe_2$	Poly.	p-type	1.33	0.01	0.07	700	+450	0.37	0.45	341
$SrOCuSbSe_2$	Poly.	p-type	1.56	0.21	1.00	850	+520	3.7	0.40	339
$LaOBiS_2$	Poly.	n-type	0.7	0.07 (estimated)	1.90	743	−200	47.6	2 (estimated)	373
LaOBiSSe	*c*-axis textured poly.	n-type	N/A	0.36	4.22	650	−162	161	0.78	374
$LaOBiSe_2$	Poly.	n-type	N/A	0.25 (estimated)	4.67	743	−140	238	1.4 (estimated)	373
$LaO_{0.9}F_{0.1}SbSe_2$	Poly.	n-type	1.0	0.02	0.18	673	−430	1.0	0.51	377
$CeOSbSe_2$	Poly.	n-type	0.6	0.03	0.34	637	−370	2.5	0.76	377
$SrFBiS_2$	Poly.	n-type	0.95	0.12	1.37	773	−224	27.4	0.85	376
SrFBiSSe	Poly.	n-type	0.52	0.34	4.12	773	−258	62	0.94	376
$Bi_4O_4S_3$	Poly.	n-type	N/A	0.030	0.42	280	−52	155	4.0	380
$LaOPbBiS_3$	Poly.	n-type	∼0.1	0.0023	0.34	320	−55	111	4.6	369
Bi_2O_2Se	Poly.	n-type	0.8	1.63	0.19	800	−230	31	0.70	382
$Bi_2O_{1.96}Te_{0.04}Se$	Poly.	n-type	N/A	6.85	0.69	773	−205	163	0.77	395
Bi_2O_2Te	Poly.	n-type	0.23	2.04	0.13	573	−200	51	0.88	397

the crystal structures and physical properties including electronic and phonon transport, as well as the recent advances in thermoelectric properties for the mixed-anion layered compounds.

1. Layered Cu-based oxychalcogenides

a. BiCuOCh (Ch = S,Se,Te). BiCuOSe crystallizes in a layered tetragonal ZrCuSiAs-type structure with space group of *P*4/*nmm*.[281,282] The crystal structure of BiCuOSe consists of alternate stacking of anti-fluorite-type $(Cu_2Se_2)^{2-}$ layer and fluorite-type $(Bi_2O_2)^{2+}$ layer along the *c*-axis [Fig. 9(a)]. Each layer has homoleptic unit of O-Bi_4 and Cu-Se_4 polyhedra, respectively. The edge-shared $(Cu_2Se_2)^{2-}$ layer acts as a carrier transport channel and the edge-shared $(Bi_2O_2)^{2+}$ layer behaves as an insulating layer. The Cu–Se bonds are covalent, Bi–O bonds are ionic, and the bonding between the layers is not electroneutral because it arises from the stacking of positively charged $(Bi_2O_2)^{2+}$ layers and negatively charged $(Cu_2Se_2)^{2-}$ layers. While the overall structure is charge-balanced and does not

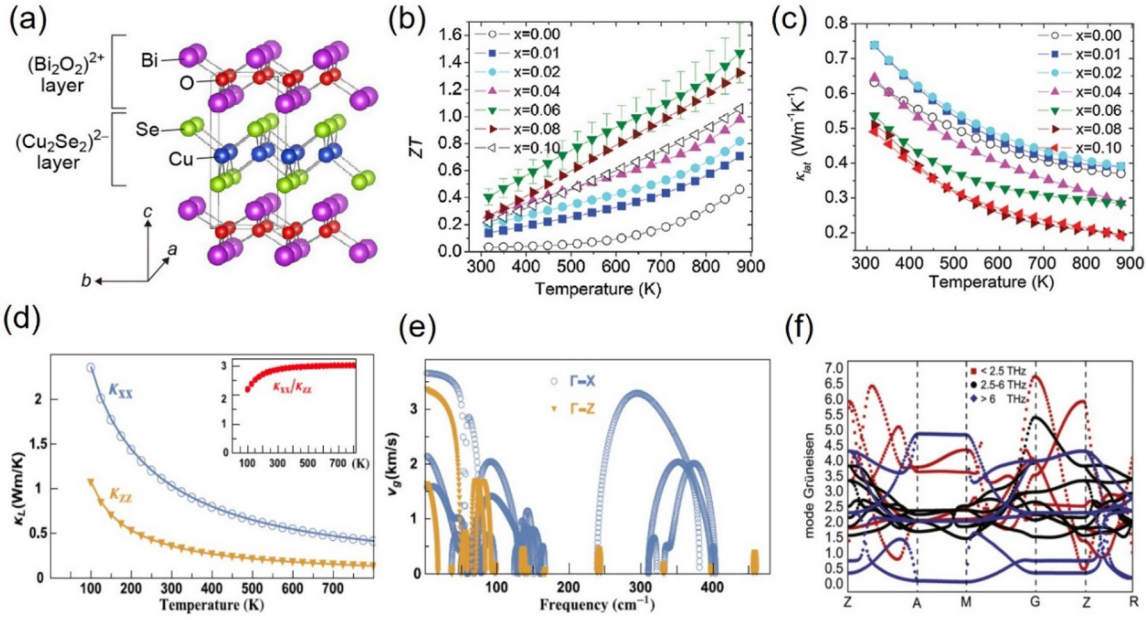

FIG. 10. Phonon transport and thermoelectric properties of layered BiCuOSe. (a) Crystal structure. (b) *ZT* and (c) lattice thermal conductivity (κ_{lat}) as a function of temperature for $Bi_{1-2x}Ca_xPb_xCuSeO$ polycrystals with different *x*. Reproduced with permission from Liu *et al.*, Adv. Energy Mater. **6**(9), 1502423 (2016). Copyright 2016 Wiley-VCH.[280] (d) Calculated lattice thermal conductivity for BiCuOSe along *a*-*b* plane (κ_{xx}) and *c*-axis (κ_{zz}) as a function of temperature. The inset shows the ratio of κ_{xx} and κ_{zz}. (e) Calculated frequency-dependent phonon group velocity (v_g) along Γ−X (in-layer direction) and Γ−Z (inter-layer direction). Reproduced with permission from Shao *et al.*, Sci. Rep. **6**, 21035 (2016). Copyright 2016 Author(s), licensed under a Creative Commons Attribution (CC BY 4.0) license.[312] (f) Calculated mode Grüneisen parameters for phonons with different frequencies. Reproduced with permission from Ding *et al.*, New J. Phys. **17**, 083012 (2015). Copyright 2015 Author(s), licensed under a Creative Commons Attribution (CC BY 3.0) license.[313]

create a macroscopic electric field, this charge arrangement results in anisotropic ionic bonding and localization of carriers within the Cu_2Se_2 layers. These features contribute to the highly anisotropic electronic structure with a sharp density of states near the Fermi level, enhancing the Seebeck coefficient. In addition, the ionic interlayer coupling contributes to anisotropic chemical bonding and strong lattice anharmonicity, which lead to low lattice thermal conductivity. BiCuOSe is a narrow gap semiconductor with bandgap of ∼0.8 eV.[283] Pristine BiCuOSe exhibits p-type conduction, mainly due to the low formation energies of acceptor Cu vacancies,[284] which is similarly observed in other Cu-based oxychalcogenide semiconductors.[285] L. D. Zhao *et al.*[279] first reported high $ZT = 0.76$ at 873 K in $Bi_{0.85}Sr_{0.15}CuOSe$ bulk polycrystals, making the family of mixed-anion layered compounds promising for thermoelectric applications in the medium temperature range. After that, significant efforts have been made to improve the *ZT* value of BiCuOSe bulks by carrier doping to optimize carrier concentration. Aliovalent ion substitution with divalent alkaline-earth elements, such as Mg^{2+}, Ca^{2+}, Sr^{2+}, and Ba^{2+},[286–290] monovalent alkali elements, such as Na^{+},[291–293] K^{+},[294,295] and Cs^{+}[296] at Bi^{3+} site have been successful in optimizing hole carrier concentration to obtain maximum PF of BiCuOSe. In addition, Pb^{2+} substitution at Bi^{3+} site[297] and Zn^{2+} substitution at Cu^{+} site,[298] as well as self-doping by Cu^{+} vacancies,[299] are effective approaches to enhance the performance of BiCuOSe. Further, converging the light and heavy hole bands through La^{3+} substitution at Bi^{3+} site,[300] and increasing the electronic conductivity by isovalent Ag^{+} substitution at Cu^{+} site[301–303] are also effective to enhance the thermoelectric properties of BiCuOSe. Currently, the co-doping of Ca^{2+} and Pb^{2+} at Bi^{3+} sites has led to a record-high $ZT = \sim 1.5$ for $Bi_{0.88}Ca_{0.06}Pb_{0.06}CuOSe$ polycrystal at 873 K [Fig. 10(b)].[280] Thermoelectric properties of BiCuOSe are reviewed in Refs. 60, 61, 304, and 305.

The remarkable advantage of high *ZT* of BiCuOSe is its low lattice thermal conductivity.[60,279,287,297,299,306–311] Non-doped BiCuOSe polycrystal exhibits lattice thermal conductivity of 0.65 W m^{-1} K^{-1} at 315 K and 0.37 W m^{-1} K^{-1} at 873 K, and the high-*ZT* $Bi_{0.88}Ca_{0.06}Pb_{0.06}CuOSe$ polycrystal exhibits 0.54 W m^{-1} K^{-1} at 320 K and 0.28 W m^{-1} K^{-1} at 873 K [Fig. 10(c)]. Several experiments have proposed that the low lattice thermal conductivity of BiCuOSe originates from its strong crystal anharmonicity (larger Grüneisen parameter, $\gamma \sim 1.5$),[60] weak chemical bonds (Young's modulus, $E \sim 78.8$ GPa at 300 K),[306] and low Debye temperature ($\Theta_D \sim 243$ K).[60] The origin of low lattice thermal conductivity for BiCuOSe has been discussed with the assistance of DFT calculations.[312–315] H. Shao *et al.* discussed the anisotropy of lattice thermal conductivity of BiCuOSe.[312] Figure 10(d) shows the temperature dependence of lattice thermal conductivity (κ_{xx}) along *a*-axis (in-layer direction) and κ_{zz} along *c*-axis (inter-layer direction) of BiCuOSe. The κ_{zz} of 0.36 W m^{-1} K^{-1} is much lower than $\kappa_{xx} = 1.04$ W m^{-1} K^{-1} at 300 K, and the ratio of κ_{xx} to κ_{zz} is 2.3–3 in all temperature range. Therefore, the low lattice thermal conductivity along inter-layer direction plays an important role in realizing high *ZT* of BiCuOSe bulk polycrystals. The obvious anisotropy of phonon conduction originates from the quite anisotropic group velocities (v_g) in BiCuOSe. Figure 10(e) shows the phonon-frequency dependence of v_g along Γ−X (in-layer direction) and Γ−Z (inter-layer

direction), indicating that the v_g along Γ−X is larger than that along Γ−Z. The low-frequency phonons originate mainly from the vibrations of Bi, Cu, and Se atoms, while the high-frequency phonons come from light O atom of BiCuOSe. The larger v_g along Γ−X originates from the chemical bonding of Bi_2O_2 and Cu_2Se_2 layers. Actually, the bulk modulus along *a* and *c* axes exhibits strong anisotropy, reflecting the anisotropic chemical bonds in BiCuOSe. Especially for high-frequency optical phonon modes, very large v_g was observed only for Γ−X direction. Due to the strong interaction of O and Bi atoms in Bi_2O_2 layer, the vibration modes related to O atom exhibit high v_g along in-layer direction. The high-frequency optical phonons contribute considerably more than one-third to the total κ_{xx}, which is remarkably different from the usual picture with little contribution from such high frequency phonons in most bulk materials.

Ding *et al.*[313] proposed that strong anharmonic bonding of Bi and abnormal atomic motion originating from the layered structure cause a large anharmonicity in BiCuOSe. The Cu and Se atoms in Cu_2Se_2 layer vibrate synchronously, while the Bi and O atoms in Bi_2O_2 layer vibrate with a different phase. The in-layer and inter-layer off-phase vibration modes provide the strong scattering in the propagation of the in-plane phonons. Figure 10(f) shows the mode Grüneisen parameters for phonons with different frequencies. The average Grüneisen parameter is ∼2.5, which is comparable to that of layered SnSe with ultra-low lattice thermal conductivity of 0.42 W m^{-1} K^{-1} along inter-layer direction at 300 K.[21] The mode Grüneisen parameters of phonon modes at low frequency region < 2.5 THz are very large, due to the strong interaction between acoustic and optical phonons. These phonon–phonon Umklapp processes scatter acoustic phonons significantly. The middle-frequency phonon modes are dominated by heavy Bi atom at 2.5–6 THz, where the mode Grüneisen parameters range from ∼2 to 2.5 around G and Z points. The high-frequency phonon modes are dominated by light O atom at > 6 THz, where the large mode Grüneisen parameters are related to Bi–O bonds. Therefore, the large Grüneisen parameter of BiCuOSe originates from Bi atom. BiCuOSe has similar layered crystal structure with LaCuOSe, but lattice thermal conductivity of BiCuOSe is less than half of 2.1 W m^{-1} K^{-1} of LaCuOSe,[316] suggesting that Bi plays important role in reducing the lattice thermal conductivity.[317] Saha *et al.* explained that the acoustic phonon modes can be hybridized with optical phonons more strongly in BiCuOSe than in LaCuOSe, which leads to a strong acoustic-optical phonon scattering and then lower lattice thermal conductivity in BiCuOSe.[314]

On the other hand, Vaqueiro *et al.*[315] proposed the presence of a localized low-energy vibration mode on the Cu atoms, which is the main origin of strong anharmonicity and the large Grüneisen parameter in BiCuOSe. The atomic displacement parameter (ADP) for Cu atom is larger than that for Bi, O, and Se atoms due to weak Cu–Se bonds. The BiCuOSe does not have cage structure, but may exhibit a Cu rattling motion because there is no suitable path for Cu ion transport in the layered structure. The presence of a localized low-energy vibration mode on the Cu atoms also contributes to the origin of low lattice thermal conductivity in BiCuOSe.

Theoretical study predicts that superior thermoelectric properties could be realized in n-type BiCuOSe.[318] Defect calculation suggests that Cl- and Br- anions are effective n-type dopants in BiCuOSe under Cu-rich growth conditions via suppressing Cu vacancy formation.[284] However, contrary to many successes in carrier doping control and high *ZT* in p-type BiCuOSe, there have been difficulties in stable n-type doping[319–322] and further study is necessary to realize the high-performance n-type BiCuOSe.

BiCuOS and BiCuOTe, sister compounds of BiCuOSe, also demonstrated moderate *ZT* values in the bulk polycrystals. $Bi_{0.95}Pb_{0.05}CuOS$ bulks shows $ZT = 0.2$ at 700 K[323] and BiCuOTe bulks show $ZT = 0.6$ at 650 K,[324] comparable to electron-doped $SrTiO_3$ bulks ($ZT \approx 0.3$ at 700 K).[262] In addition, it should be noted that the Bi_2O_2 layer of BiCuO*Ch* can be replaced with Ba_2F_2 layer, resulting in BaCu*Ch*F. The synthesized bulks show p-type conduction.[325,326] Although there are no reports on their thermoelectric properties, low lattice thermal conductivity < ∼1 W m^{-1} K^{-1} is predicted by phonon calculations.[327] Reduction of lattice thermal conductivity and further enhancement of *ZT* can be expected by expanding the material system with other chemical compositions and different layers.

b. $Bi_2REO_4Cu_2Se_2$ (RE = rare earth). The low lattice thermal conductivity and excellent thermoelectric performance observed in layered BiCuOSe prompt the expansion to the analogous layered compounds with Cu_2Se_2 transport layers sandwiched by other oxide layers. $Bi_2REO_4Cu_2Se_2$ (*RE* = Y, Nd, Sm, Eu, Gd, Tb, Dy, Ho, and Er) crystallizes in the $Sr_2Mn_3Sb_2O_2$-type structure with space group of *I*4/*mmm*, and consists of fluorite-type $(Bi_2REO_4)^+$ layer and anti-fluorite-type $(Cu_2Se_2)^{2-}$ layers stacked alternatively along the *c*-axis [Fig. 11(a)].[328,329] $Bi_2YO_4Cu_2Se_2$ has narrow bandgap of 0.3 eV estimated by DFT calculations,[330] while the bandgaps of other $Bi_2REO_4Cu_2Se_2$ are estimated to be 0.03–0.04 eV.[329] First, Tan *et al.* reported that $Bi_2YO_4Cu_2Se_2$ exhibits relatively low lattice thermal conductivity ∼1.8 W m^{-1} K^{-1} at 300 K and it is further decreased to ∼0.9 W m^{-1} K^{-1} at 873 K.[330] Very large anisotropy of lattice thermal conductivity along in-layer and inter-layer direction is expected for $Bi_2REO_4Cu_2Se_2$ due to the thick Bi_2REO_4 layers, and it is considered that the contribution of heavy Bi and the local vibration of Cu atom in Cu_2Se_2 layer could generate anharmonicity and low lattice thermal conductivity. Most of the reported Cu-based layered oxychalcogenides are semiconductors, but the metallic behavior is observed in the $Bi_2REO_4Cu_2Se_2$.[331] The $(Bi_2REO_4)^+$ layer provides only one electron to the $(Cu_2Se_2)^{2-}$ layer, and hole is naturally generated, resulting in a metallic conduction with p-type carriers. $Bi_2YO_4Cu_2Se_2$ shows a low ZT ∼0.057 at 673 K because the Fermi level is deep inside the valence band, resulting in low Seebeck coefficient.[332] On the other hand, substituting Y with other *RE* ions results in further reduction of lattice thermal conductivity and an increase in electronic conductivity. Maximum $ZT = 0.27$ at 923 K is achieved in $Bi_2DyO_4Cu_2Se_2$ [Figs. 11(b) and 11(c)].[329] Further *ZT* enhancement can be expected in the $Bi_2REO_4Cu_2Se_2$ if the over-doped hole concentration is reduced by electron doping.

c. $Sr_2TMCu_2O_2Ch_2$ (TM = Mn, Co, Zn, Ch = S, Se, Te). Further complex layered Cu-based oxychalcogenides $Sr_2TMCu_2O_2Ch_2$ with *TM* = Mn, Co, Zn and *Ch* = S, Se, Te have been investigated as a potential thermoelectric material,[333–336] because it shares the Cu_2Ch_2 transport layer similar to BiCuOSe [Fig. 12(a)]. $Sr_2TMCu_2O_2Ch_2$ crystallizes in $Sr_2Mn_3Sb_2O_2$-type structure with space group of *I*4/*mmm*, consisting of alternately stacked anti-fluorite-type Cu_2Ch_2 and square planar *TM* oxide layers. Between these two layers, Sr surrounded by 4 *Ch* and 4 O atoms, forms the interstitial layer. The *TM* ions are

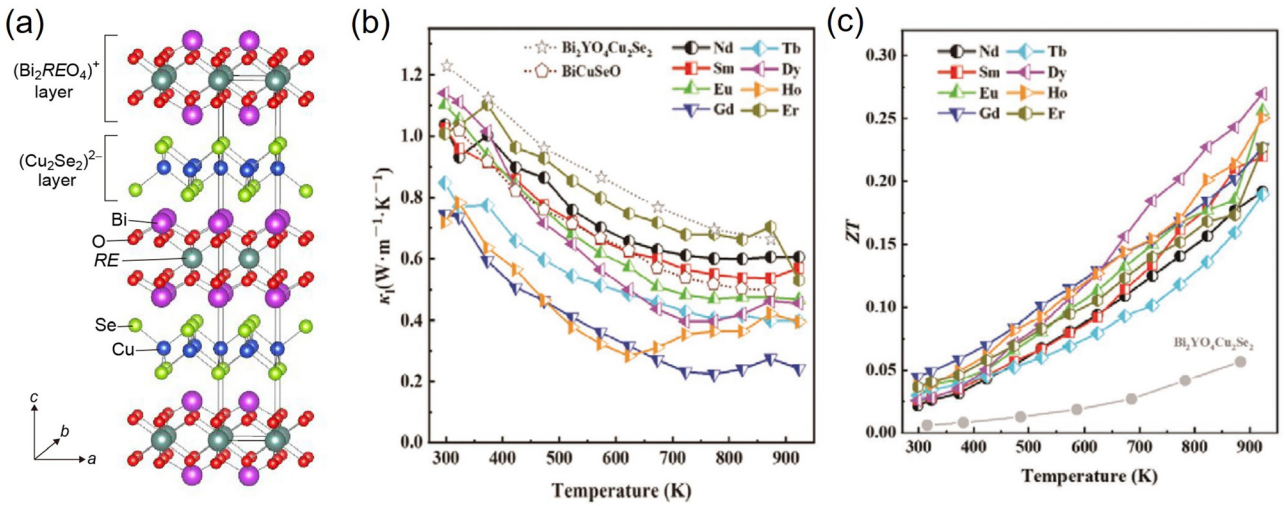

FIG. 11. Phonon transport and thermoelectric properties of layered $Bi_2REO_4Cu_2Se_2$ (RE = rare earth). (a) Crystal structure. (b) and (c) Temperature dependence of lattice thermal conductivity (κ_l) and ZT. Reproduced with permission from Yang *et al.*, Adv. Funct. Mater. **32**(18), 2113164 (2022). Copyright 2022 Wiley-VCH.[329]

surrounded by four in-layer O atoms and two apical O atoms, resulting in a tetragonally elongated perovskite-like structure. It is reported that $Sr_2ZnCu_2O_2S_2$ has relatively large bandgap of 2.7 eV, and the pristine $Sr_2ZnCu_2O_2S_2$ bulk is highly insulating, but Na^+ ion substitution at Sr^{2+} site largely increases hole concentration, resulting in higher electronic conductivity of 0.12 S cm^{-1} at RT.[333,337] $Sr_2CoCu_2O_2Se_2$ has smaller bandgap of 1.45 eV.[335] $Sr_2CoO_2Cu_2Se_2$ bulk shows p-type conduction with electronic conductivity of 50 S cm^{-1} and high hole mobility of 33.3 cm^2 V^{-1} s^{-1} at RT.[334] The bandgap of $Sr_2MnCu_2O_2Te_2$ is 0.85 eV,[336] and it also shows p-type conduction with electronic conductivity of 25 S cm^{-1} at RT. Thermoelectric properties of $Sr_2TMCu_2O_2Te_2$ (TM = Mn, Co, and Zn) are summarized in Figs. 12(b)–12(f). The Zn compound exhibits semiconducting behavior, whereas the Mn and Co compounds show weak temperature dependence of electrical resistivity, indicative of degenerate conduction [Fig. 12(b)]. The Seebeck coefficient increases gradually with

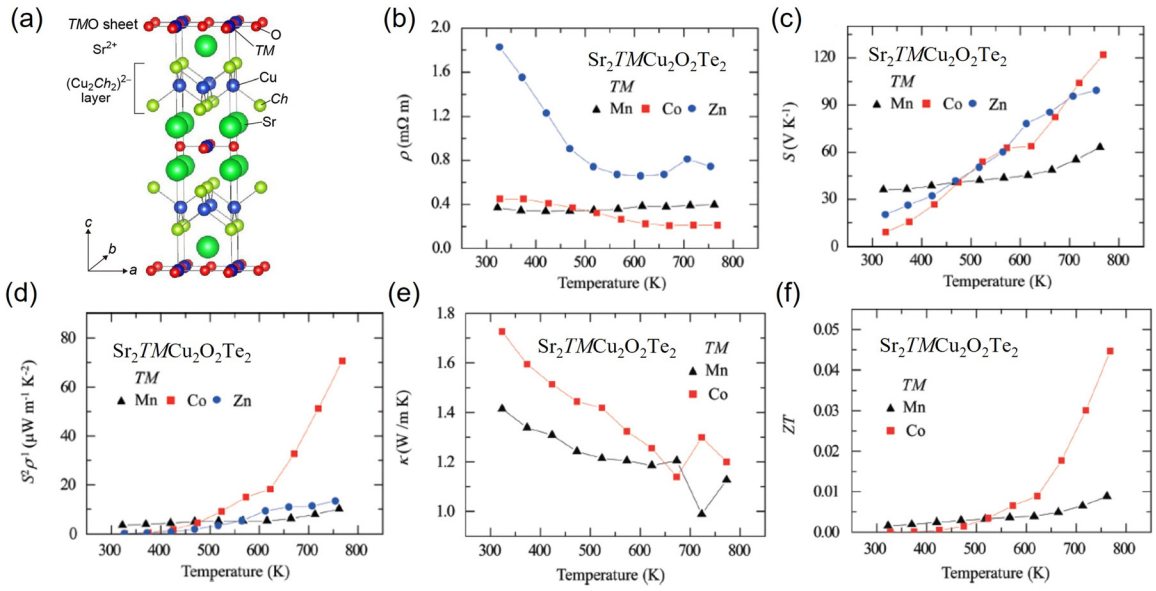

FIG. 12. Thermoelectric properties of layered $Sr_2TMCu_2O_2Ch_2$: (a) Crystal structure. (b)–(d) Temperature dependence of (b) electrical resistivity (ρ), Seebeck coefficient (S), (d) power factor for bulk polycrystals of $Sr_2TMCu_2O_2Te_2$ with TM = Mn, Co, and Zn. (e) and (f) Temperature dependence of (e) thermal conductivity (κ) and (f) dimensionless figure of merit for bulk polycrystals of $Sr_2TMCu_2O_2Te_2$ with TM = Mn and Co. Reproduced with permission from Song *et al.*, J. Mater. Chem. C **6**(45), 12260–12266 (2018). Copyright 2018 The Royal Society of Chemistry.[336]

temperature, with the slope systematically varying depending on the *TM* element; the slope becomes steeper on the order of Mn, Zn, to Co [Fig. 12(c)]. The PF of the Co compound reaches 70 μW m^{-1} K^{-2} at 770 K, which is the highest among those of the three compounds [Fig. 12(d)]. Thermal conductivity has been measured only for $Sr_2TMCu_2O_2Te_2$ with *TM* = Mn and Co [Fig. 12(e)]. The thermal conductivity at RT is 1.41 W m^{-1} K^{-1} for $Sr_2MnCu_2O_2Te_2$ and 1.72 W m^{-1} K^{-1} for $Sr_2CoCu_2O_2Te_2$.[336] With increasing temperature, the thermal conductivity decreases to ∼1.2 W m^{-1} K^{-1} at 770 K. Although their *ZT* is limited to 0.045 at 770 K [Fig. 12(f)], but the complex layered structures and selectable many ions with variable sizes in $Sr_2TMCu_2O_2Ch_2$ are still expected to provide opportunities for lower lattice thermal conductivity and higher *ZT*. It should be noted that a related compound AE_2CuInO_3Ch (*AE* = Sr, Ba and *Ch* = S, Se, Te) has a layered structure composed of alternately stacked $(AE_4In_2O_6)^{2+}$ perovskite-like layer and the Cu_2Ch_2 transport layer along the *c*-axis. Sr_2CuInO_3S bulk exhibits low lattice thermal conductivity of 0.73 W m^{-1} K^{-1} at 300 K.[338]

d. SrOCuPnSe$_2$ (Pn = Sb and Bi). SrOCu*Pn*Se$_2$ (*Pn* = Sb and Bi) crystallizes in a unique layered crystal structure (monoclinic space group of $P2_1/m$) composed of $(CuPnOSe_2)^{2-}$ carrier transport layers sandwiched by Sr^{2+} cations [Fig. 13(a)].[339–341] These compounds were designed and synthesized by the interaction of SrO into van der Waals gap of layered Cu*Pn*Se$_2$.[342,343] The SrOCuSbSe$_2$ has an in-direct bandgap of 1.56 eV,[339] while SrOCuBiSe$_2$ has a direct bandgap of 1.33 eV.[341]

Here, we explain the characteristics of the crystal structure and phonon transport for SrOCuBiSe$_2$ as a representative. The $(CuBiOSe_2)^{2-}$ layer is composed of $(CuSe_2)^{3-}$ double chains and

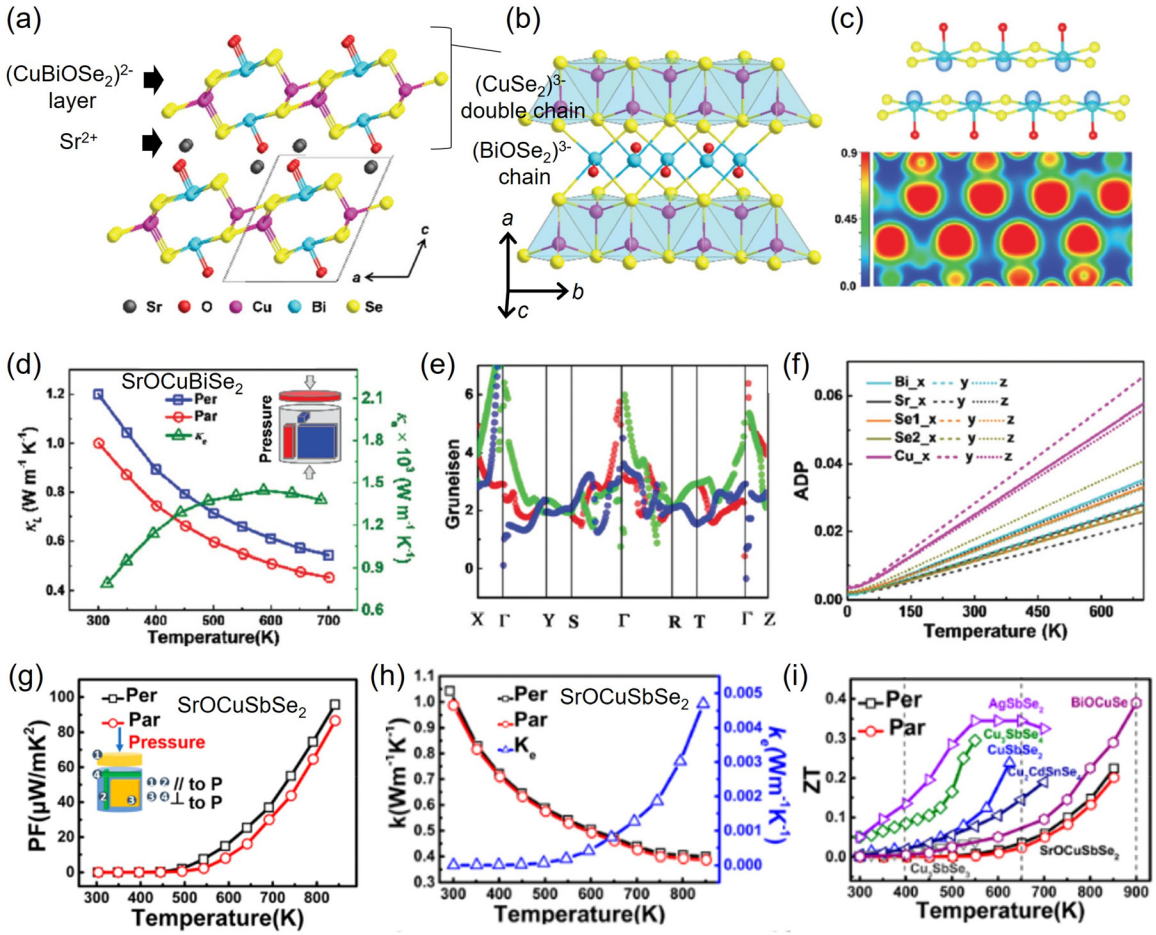

FIG. 13. Phonon transport and thermoelectric properties of layered SrOCu*Pn*Se$_2$ (*Pn* = Sb and Bi). (a) Crystal structure of SrOCuBiSe$_2$. (b) Enlarged view of $CuBiOSe_2$ layer. (c) Electron localization function graph (top panel) and valence electron density map (bottom panel) for polyhedral coordination of Bi atoms in SrOCuBiSe$_2$. (d) Temperature dependence of lattice thermal conductivity (κ_L) and electronic thermal conductivity (κ_{ele}) for SrOCuBiSe$_2$ polycrystals, where Per and Par indicate the perpendicular and the parallel direction to the SPS pressure, respectively, as shown in the inset. (e) Grüneisen dispersion for acoustic phonon modes. (f) Atomic displacement parameter (ADP) for different atoms along the *a*, *b*, and *c* directions. Reproduced with permission from Luo *et al.*, Chem. Commun. **56**(31), 4356–4359 (2020). Copyright 2020 The Royal Society of Chemistry.[341] (g)–(i) Thermoelectric properties of (g) power factor (PF), (h) thermal conductivity (*k*) and electronic thermal conductivity (k_e), and (i) dimension-less figure of merit for SrOCuSbSe$_2$ polycrystals. Reproduced with permission from Bu *et al.*, Inorg. Chem. **58**(1), 69–72 (2019). Copyright 2018 The American Chemical Society.[340]

$(BiOSe_2)^{3-}$ chains [Fig. 13(b)]. Each $(CuSe_2)^{3-}$ chain shares Se atoms with $(BiOSe_2)^{3-}$ chain, which forms the $(CuBiOSe_2)^{2-}$ anionic layers. The iso-surface of charge density map around the Bi atoms shows the anisotropic electron localization [Fig. 13(c)], which is the typical signature of the $6s^2$ lone-pair electrons. The existence of Bi $6s^2$ lone pair electrons results in soft phonon modes and strong anharmonicity in the lattice. Figure 13(d) shows the lattice thermal conductivity measured along the direction parallel or perpendicular to the pressure applied to the $SrOCuBiSe_2$ bulk polycrystals during spark plasma sintering (SPS).[341] Due to their layered structure and high external pressure during the SPS process, the *a*-*b* plane tends to be perpendicular to the pressure direction. Low lattice thermal conductivity of 1.0 W m^{-1} K^{-1} was observed along parallel direction at 300 K, and it further decreases to 0.45 W m^{-1} K^{-1} at 700 K. Also, the lattice thermal conductivity parallel to pressure direction ($\kappa_{lat,parallel}$) is lower than that perpendicular to the pressure direction ($\kappa_{lat,perpendicular}$) in the entire temperature range, reflecting the anisotropic layered structure of $SrOCuBiSe_2$. $SrOCuSbSe_2$ polycrystals also show low lattice thermal conductivity of 0.40 W m^{-1} K^{-1} at 700 K.[339] Based on phonon calculations, K. Bu *et al.* observed the anisotropic vibration modes of Sr, O, Bi, and Se, where Bi atoms tend to vibrate along the *a* axis, while the Sr and Se atoms vibrate mainly along the *c* direction. The anisotropic vibration of Sr indicates that the SrO units are phonon scattering layers, which is consistent with the strong anisotropy of κ_{lat}. Actually, compared to the lattice thermal conductivity of 3.0 W m^{-1} K^{-1} for $CuBiSe_2$ bulk at 300 K,[344] the SrO intercalation for $SrOCuBiSe_2$ strongly suppresses lattice thermal conductivity by serving as a thermal blocking layer.

Similar to BiCuOSe, Bi atom dominates the low-frequency phonons and leads to an extensive acoustic-optical phonon scattering. The calculated Grüneisen parameters are shown in Fig. 13(e). The average Grüneisen parameter of 3.46 for $SrOCuBiSe_2$ is much larger than 2.90 of BiCuOSe. Therefore, a strong lattice anharmonicity is an important sign for their low lattice thermal conductivity. Higher values of the Grüneisen parameters are found along the Γ−Z and X−Γ dispersions, corresponding to the two directions of the Bi $6s^2$ lone-pair electrons. In addition, the large ADP of Cu atoms is observed especially along the *b*-axis direction, indicating a weak bonding between Cu and Se atoms. The large ADP suggests that the Cu atoms possess rattling vibration along the *b*-axis direction, which further decreases the lattice thermal conductivity. The ADP of Cu atoms in $SrOCuBiSe_2$ is much larger than that of the Cu atoms in $CuBiSe_2$. The low lattice thermal conductivity is attributed to the dual effects of high ADP value and large Grüneisen parameter, which are caused by rattling vibration of Cu atoms and lone-pair electrons of Bi atom, respectively.

Non-doped bulks of $SrOCuSbSe_2$ ($SrOCuBiSe_2$) show p-type conduction with hole concentration of 2.4×10^{19} (5.4×10^{18}) cm^{-3} and hole mobility of 0.114 (0.235) cm^2 V^{-1} S^{-1} at RT, respectively. Although the *ZT* is limited at 0.01 for $SrOCuBiSe_2$ at 700 K,[341] higher thermoelectric performance was reported for $SrOCuSbSe_2$.[340] The bulk sample of $SrOCuSbSe_2$ exhibits an increase in PF, reaching ∼100 μW m^{-1} K^{-2} at 850 K. The high PF originates from the large Seebeck coefficient, which may be attributed to the insulating SrO layers that enhance two-dimensional confinement of the charge carriers. The thermal conductivity of $SrOCuSbSe_2$ is as low as ∼1.0 W m^{-1} K^{-1} at RT and further decreases to ∼0.4 W m^{-1} K^{-1} at 850 K. Consequently, the *ZT* value of $SrOCuSbSe_2$ reaches a maximum of 0.22 at 850 K. Further performance enhancement can be expected by carrier doping and texture engineering to obtain higher PF.

2. Layered Ag-based oxychalcogenide, BiAgOCh (Ch = S, Se, Te)

Layered BiAgOSe with space group of *P*4/*nmm*, i.e., the complete replacement of Ag^+ ion at Cu^+ site in BiCuOSe, is also expected to show high thermoelectric performance with low lattice thermal conductivity. BiAgOSe was synthesized by hydrothermal method with an alkaline environment at low temperature. The conventional solid-state reaction is not applicable for synthesis of BiAgOSe because of the decomposition to the stable intermediate compounds, such as Bi_2O_2Se, $AgBiSe_2$, and Ag_2Se at high temperature > 500 °C.[345] The BiAgOSe is an indirect bandgap semiconductor with a bandgap of 0.95 eV. Note that BiAgOS was synthesized by hydrothermal method[346] and mechanochemical method,[347] and the bandgap was reported to be 1.5 eV. Meanwhile, there have been no reports on the experimental synthesis of BiAgOTe until now.

The temperature dependence of total thermal conductivity for BiAgOSe bulk polycrystals is shown in Fig. 14(a). The total thermal conductivity of BiAgOSe at RT is ∼0.61 W m^{-1} K^{-1} and decreases to 0.35 W m^{-1} K^{-1} at 650 K, which is further lower than that of BiCuOSe. Figure 14(b) compares the calculated lattice thermal conductivity (κ_{xx}) along in-layer direction and κ_{zz} along inter-layer direction of BiAgOSe. The calculated κ_{zz} of 0.21 W m^{-1} K^{-1} is much lower than $\kappa_{xx} = 1.29$ W m^{-1} K^{-1} at RT, displaying the large anisotropy of lattice thermal conductivity originating from the layered structure, and the ratio of κ_{xx} to κ_{zz} is estimated to be ∼6, which is much larger than BiCuOSe. The calculated Grüneisen parameter (γ) and three phonon–phonon scattering rate (τ^{-1}) are compared between BiAgOSe and BiCuOSe in Fig. 14(c). BiAgOSe has larger γ and higher τ^{-1} than BiCuOSe in the low-frequency region < 100 cm^{-1}, where phonons carry most of the heat. The strong phonon–phonon scattering within this frequency region effectively lowers the phonon relaxation time and subsequently reduces lattice thermal conductivity in BiAgOSe. There are two large peaks of γ at ∼60 and ∼25 cm^{-1}, where the former is mainly due to Bi and Ag atoms and the later is mainly due to Ag atom.

The crystal structure of BiAgOSe consists of $(Bi_2O_2)^{2+}$ and $(Ag_2Se_2)^{2-}$ layers. BiAgOSe has larger lattice parameters due to the larger ionic radius of Ag^+ (102 pm) than that of Cu^+ (60 pm).[348] The large distortion is introduced in $Ag-Se_4$ tetrahedra as a result of the large size mismatch with $O-Bi_4$ tetrahedra, i.e., the $[Ag_2Se_2]^{2-}$ layer is under compressive strain from $[Bi_2O_2]^{2+}$ layer. The large deviation from the ideal tetrahedra reduces the orbital overlap/coupling between Ag-4*d* and Se-4*p* orbitals, which results in a lower Ag–Se bond stiffness and more localized Ag displacement (rattling-like behavior). Actually, Ag has the largest ADP due to the soft Ag–Se bonds, and the fastest increasing rate with temperature, which indicates the large vibration of Ag atoms [Fig. 14(d)]. Therefore, the mismatch between layers in the mixed-anion compounds can tune phonon interactions, which provides an extra avenue for engineering phonon transport properties. There are theoretical predictions of very low lattice thermal conductivity also in BiAgOTe[349] and LaAgO(S,Se).[350] In addition, theoretical study predicts that BaAg*Ch*F, where the Bi_2O_2 layers are replaced by Ba_2F_2 layer, shows low lattice thermal conductivity, although there have been no reports on experimental synthesis. Experimental

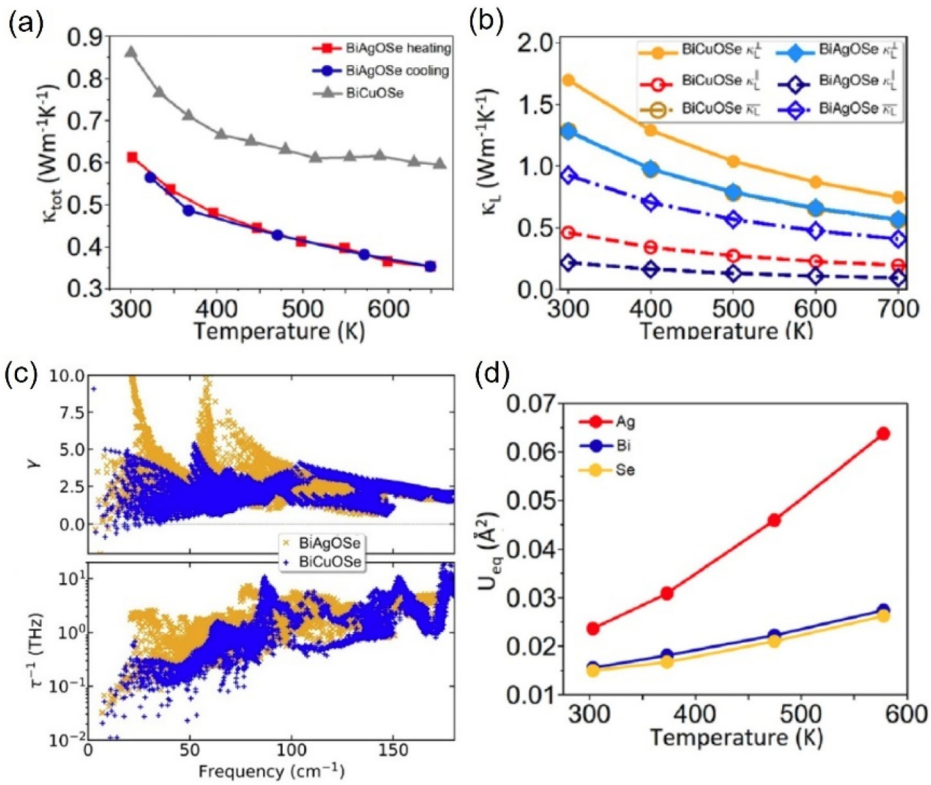

FIG. 14. Phonon transport in layered BiAgOSe. (a) Total thermal conductivity (κ_{tot}) as a function of temperature. (b) Calculated lattice thermal conductivity along *a*-axis ($\kappa_L^{\perp}$) and *c*-axis ($\kappa_L^{\parallel}$) and average $\kappa(-)_L$ of BiAgOSe and BiCuOSe. (c) Calculated frequency-dependent Grüneisen parameters (γ) and phonon-phonon scattering rate (τ^{-1}) of BiAgOSe and BiCuOSe. (d) Atomic displacement parameter (U_{eq}) for Ag, Bi, and Se atoms of BiAgOSe as a function of temperature. Reproduced with permission from Zhang *et al.*, J. Am. Chem. Soc. **144**(6), 2569–2579 (2022). Copyright 2022 American Chemical Society.[345]

confirmation of high *ZT* is expected for the layered Ag-based oxychalcogenides.

3. Layered Bi-based oxy(fluoro)chalcogenides

Layered Bi-based oxychalcogenides and fluorochalcogenides have received great attention since the discovery of superconductivity. For example, superconductivity has been observed in $Bi_4O_4S_3$ with a critical temperature (T_c) of 8.6 K,[351] F-doped *RE*OBiS$_2$ (*RE*: La, Ce, Pr, Nd, and Yb) with T_c as high as 11 K,[352–358] *AE*FBiS$_2$ (*AE*: Sr and Eu) with T_c as high as 3 K,[359–362] and $Eu_3F_4Bi_2(S,Se)_4$ with T_c of 3.4 K.[363,364] In addition, Bi_2O_2Ch is also known as a Bi-based oxychalcogenide with layered structure. Recently, Bi_2O_2Ch has received great attention as a new-type 2-dimensional (2D) material, since the discovery of high carrier mobility,[365] tunable bandgap,[366] and ferroelectricity[367] in ultra-thin Bi_2O_2Ch crystals.

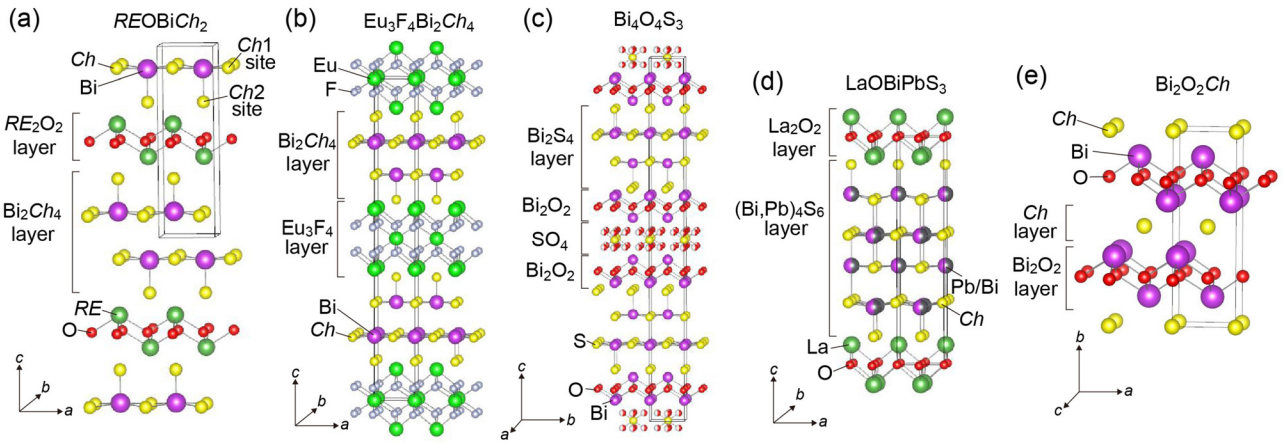

FIG. 15. Layered crystal structures of Bi-based oxy(fluoro)chalcogenides. (a) *RE*OBiCh_2 (*RE* = rare earth, *Ch* = S, Se), (b) $Eu_3F_4Bi_2Ch_4$ (*Ch* = S, Se), (c) $Bi_4O_4S_3$, (d) LaOBiPbS$_3$, and (e) Bi_2O_2Ch (*Ch* = S, Se, Te).

Typical crystal structures are categorized into five groups (Fig. 15). *RE*OBi*Ch*$_2$ (*RE* = rare earth, *Ch* = S and Se) possesses layered crystal structure (space group: *P*4/*nmm*) with the Bi$_2$*Ch*$_4$ layer (Bi*Ch*$_2$ double layers) as a conducting layer and the RE_2O_2 layer as a blocking insulator layer [Fig. 15(a)]. The RE_2O_2 layer of *RE*OBi*Ch*$_2$ structure can be replaced with the AE_2F_2 (*AE* = Sr and Eu) layer, resulting in the formation of *AE*FBi*Ch*$_2$. Eu$_3$F$_4$Bi$_2$*Ch*$_4$ (*Ch*: S and Se) possesses the layered structure (space group of *I*4/*mmm*) with similar Bi$_2$*Ch*$_4$ layer for carrier transport, but it is sandwiched by a thick Eu$_3$F$_4$ layer as a blocking layer [Fig. 15(b)].[363,368] Bi$_4$O$_4$S$_3$ takes layered crystal structure with alternate stacks of Bi$_2$*Ch*$_4$ layer and the Bi$_4$O$_4$(SO$_4$) blocking layer, which is composed of two Bi$_2$O$_2$ layers and SO$_4$ layer [Fig. 15(c)]. The parent compound is Bi$_4$O$_4$(SO$_4$)Bi$_2$S$_4$ (space group of *I*4/*mmm*), while the Bi$_4$O$_4$S$_3$ compound has vacancies at 50% of SO$_4$ layer, i.e., Bi$_4$O$_4$(SO$_4$)$_{0.5}$Bi$_2$S$_4$ [351]. Note that there has been no report on the synthesis of Bi$_4$O$_4$Se$_3$ and Bi$_4$O$_4$Te$_3$ compounds. On the other hand, further complex layered structure is found in LaOBiPbS$_3$ (space group of *P*4/*nmm*) with a thick carrier transport layer of *Pn*$_4$S$_6$ (*Pn* = Bi, Pb) sandwiched by La$_2$O$_2$ blocking layers [Fig. 15(d)].[369] In these layered Bi-based oxy(fluoro)chalcogenides, the crystal structures are characterized by the alternate stacking of Bi*Ch*$_2$ (or *MCh*$_2$) carrier transport layers and blocking layers.

On the other hand, Bi$_2$O$_2$*Ch* has different-type layered structure consisting of $[Bi_2O_2]^{2+}$ layers and Ch^{2-} square net layers alternately stacked along the *c*-axis [Fig. 15(e)].[370] Bi$_2$O$_2$Se and Bi$_2$O$_2$Te have anti-ThCr$_2$Si$_2$ type layered structure (space group of *I*4/*mmm*), while Bi$_2$O$_2$S has similar layered structure but distorted structure (space group of *Pnnm*) with lower symmetry, where Bi atoms slide slightly apart along *a*-axis. These Bi-based oxy(fluoro)chalcogenides exhibit n-type conduction. The bottom of the conduction band consists primarily of Bi 6*p* states, and the Bi*Ch*$_2$ layers or Bi$_2$O$_2$ layer dominate the electronic conduction. Due to these characteristics of the low-dimensional crystal structure and electronic states, the layered Bi-based oxy(fluoro)chalcogenides have been expected as potential n-type thermoelectric materials with low lattice thermal conductivity, complemented by p-type Cu- and Ag-based ones.

*a. LaOBi*Ch$_2$ *(*Ch = *S, Se).* LaOBiS$_2$ is an n-type semiconductor with a bandgap ~0.7 eV.[371] The carrier concentrations can be controlled by partial substitution of F^- ion at O^{2-} site of La_2O_2 layer (electron doping to BiS$_2$ layer).[372] LaOBiS$_2$ bulk polycrystal exhibits relatively low lattice thermal conductivity of 1.85 W m^{-1} K^{-1} at 300 K,[373] and it is reported that the partial substitution of Se ion at S site of LaOBiS$_2$ is very effective to enhance PF and reduce lattice thermal conductivity.[373,374] Figure 16(a) summarizes the temperature dependence of lattice thermal conductivity and *ZT* for hot-pressed LaOBiSSe bulk polycrystals.[374] There is a large anisotropy in lattice thermal conductivity, and the low lattice thermal conductivity <1 W m^{-1} K^{-1} is obtained along the pressure direction due to the preferred orientation along *c*-axis. The lattice thermal conductivity is further reduced with increasing temperature, and the lowest lattice thermal conductivity is 0.8 W m^{-1} K^{-1} at 650 K. Maximum *ZT* = 0.36 at 650 K is obtained for the n-type LaOBiSSe. Note that the low lattice thermal conductivity of ~2.5 W m^{-1} K^{-1} at 300 K is also reported in bulk polycrystals of SrFBiS$_2$, where LaO layer is replaced with SrF layer.[375] Similarly, SrFBiS$_2$ shows n-type conduction, and the large amount of Se substitution at S site of SrFBiS$_2$ leads to higher PF and lower lattice thermal conductivity of 1.25 W m^{-1} K^{-1} at 300 K, resulting in the enhanced *ZT* = 0.34 in SrFBiSSe at 773 K.[376] In addition, the low lattice thermal conductivity of 1.5 W m^{-1} K^{-1} at 300 K is reported for LaOSbSe$_2$, where the BiS$_2$ layer of LaOBiS$_2$ is replaced with SbSe$_2$ layer.[377] Further lower lattice thermal conductivity of 0.8 W m^{-1} K^{-1}

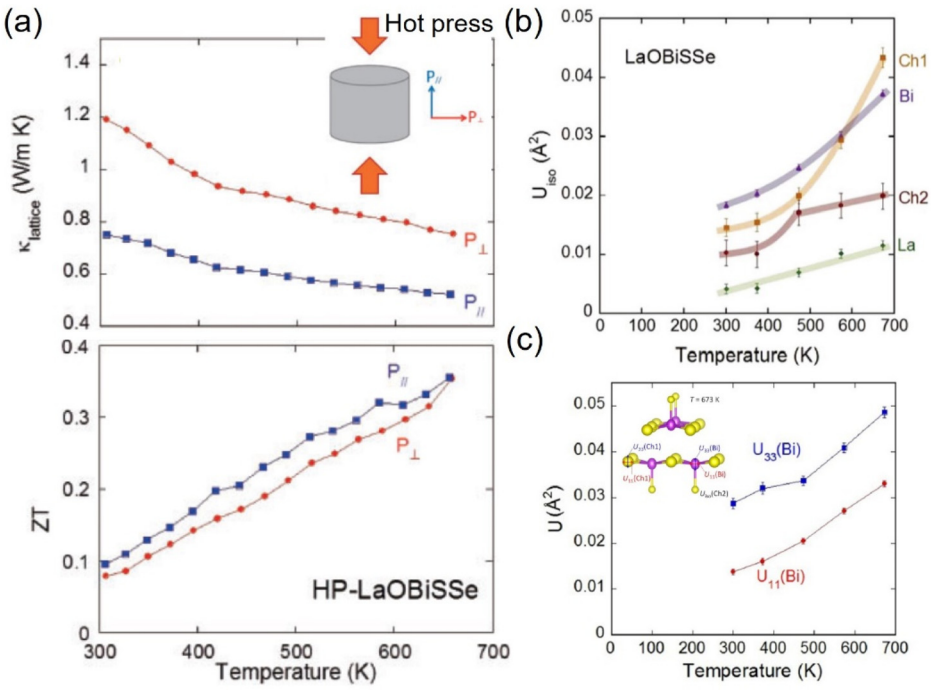

FIG. 16. (a) Temperature dependence of lattice thermal conductivity, $\kappa_{lattice}$ (upper panel) and *ZT* (lower panel) for hot-pressed LaOBiSSe bulk polycrystals. Reproduced with permission from Nishida *et al.*, Appl. Phys. Express **8**(11), 111801 (2015). Copyright 2015 IOP Publishing.[374] (b) Temperature dependences of isotropic atomic displacement parameters (U_{iso}) for the La, Bi, *Ch*1, and *Ch*2 sites of LaOBiSSe. (c) In-plane atomic displacement parameters (U_{11} and U_{33}) for Bi site of LaOBiSSe. Inset shows the schematic images of the crystal structure of the Bi$_2$*Ch*$_2$ layer depicted using U_{11} and U_{33} at 673 K. Reproduced with permission from Mizuguchi *et al.*, J. Appl. Phys. **119**(15), 155103 (2016). Copyright 2016 AIP Publishing.[378]

at 300 K is observed for $CeOSbSe_2$. These (La,Ce)$OBiS_2$ compounds also show n-type conduction, but further carrier doping is necessary to increase PF and ZT at the current stage.

The low lattice thermal conductivity of LaOBiSSe is explained by anomalous rattling motion of Bi atoms, even though it does not have cage structure.[378,379] The BiS_2 layer is composed of Bi–S_5 pyramid structure with a Bi atom located at the center of its basal plane [Fig. 15(a)]. Crystal structure refinements revealed that Se atoms are mainly replaced at the in-plane *Ch*1 site of $LaOBiS_2$. The ion radius of Se is larger than that of S, and thus Se substitution provides chemical pressure to Bi atoms. Figure 16(b) shows the temperature dependence of the isotropic ADP (U_{iso}) of LaOBiSSe. The Bi, *Ch*1, and *Ch*2 atoms vibrate considerably compared with La atoms. The extrapolation of the temperature dependence of U_{iso} for Bi, *Ch*1, and *Ch*2 atoms does not approach zero and shows a finite large value at 0 K, suggesting that they exhibit anharmonic vibrations. Particularly, the in-plane Bi and *Ch*1 atoms exhibit large U_{iso} values. The anisotropic ADP (U_{11} and U_{33}) as a function of temperature for the Bi site is shown in Fig. 16(c). Both *U*11(Bi) and *U*33(Bi) increase with increasing temperature, but U_{33}(Bi) is larger than U_{11}(Bi) at the entire temperature range. The large Bi atomic displacement along the *c*-axis direction is explained by the presence of the rattling-like motion of Bi atoms. Lee *et al.*[379] reported that the energy of the Bi rattling mode decreases with increasing the substituted Se concentration, resulting in the increased anharmonicity and the lower lattice thermal conductivity. The in-plane chemical pressure should be responsible for the enhancement of rattling motion in the planar coordination of BiCh_2 layer. The crystal structure of LaOBiSSe is not a cage structure, but the observed rattling-like vibration of Bi in the layered structure would lead to new design concept for high performance thermoelectric materials with very low lattice thermal conductivity.

b. $Bi_4O_4S_3$. $Bi_4O_4S_3$ shows high n-type electronic conductivity, because of the natural formation of vacancies at SO_4 layer.[351] The total thermal conductivity is 4.92 W m^{-1} K^{-1}, and the lattice contribution is estimated to be 4.0 W m^{-1} K^{-1} at RT.[380] Unfortunately, due to the high electron concentration, $Bi_4O_4S_3$ exhibits low Seebeck coefficient. However, their high electronic conductivity and relatively low thermal conductivity provide the $ZT = 0.03$ at 280 K. If the carrier concentration can be suppressed by controlling the chemical composition in $Bi_4O_4S_3$, i.e., reducing the amount of SO_4 vacancies, it would be possible to enhance their thermoelectric properties.

c. $LaOBiPbS_3$. Sun *et al.*[369] reported thermoelectric properties of $LaOBiPbS_3$ below the RT. The $LaOBiPbS_3$ has narrow bandgap ~0.1 eV and the bulk polycrystal shows high n-type conductivity with 111 S cm^{-1} at RT. The total thermal conductivity is estimated to be ~4 W m^{-1} K^{-1}, and the ZT is limited to be 0.0023 at RT. However, Kurematsu *et al.* theoretically investigated the thermoelectric properties of 24 possible variations of the constituent elements in analogous compounds of $LaOBiPbS_3$.[381] Especially, $LaOPbSbSe_3$ is predicted to have a PF five times as large as that of $LaOBiPbS_3$, which expects to lead the experimental conformation for the enhancement of ZT in this material system.

d. Bi_2O_2Ch (Ch = S, Se, Te). Bi_2O_2Se has been intensively studied with detailed characterization of physical properties in bulk, single crystal, and thin film. Bi_2O_2Se is an n-type semiconductor with bandgap of 0.8 eV.[365] The bulk single crystal of Bi_2O_2Se exhibits high electron mobility ~300 cm^2 V^{-1} s^{-1} at RT. Bi_2O_2Se bulk polycrystal shows a very low thermal conductivity of 1.1 W m^{-1} K^{-1} at RT and it further decreases to ~0.7 W m^{-1} K^{-1} at 800 K.[382] Bi_2O_2Se single crystal exhibits thermal conductivity ~2 W m^{-1} K^{-1} along *a*-*b* plane (in-layer direction) at RT.[383] Phonon calculation shows that the in-layer and inter-layer lattice thermal conductivity are 1.32 and 0.82 W m^{-1} K^{-1}, respectively, reflecting the anisotropic layered crystal structure.[384]

Pristine Bi_2OS_2 bulk polycrystal shows $ZT = 0.19$ at 800 K,[382] but the ZT value is limited by insufficient carrier concentration to optimize PF. Further ZT enhancement was demonstrated by the aliovalent ion substitution of Sn^{4+},[385] Ge^{4+},[386,387] Ta^{5+},[388] Nb^{5+} at Bi^{3+} site,[389] and the substitution of Cl- at Se^{2-} site,[390] which are effective to increase electron concentrations for enhancement of PF. In addition, isovalent La^{3+} and Sb^{3+} substitutions at Bi^{3+} site,[391,392] Bi site deficiency,[393] and off-stoichiometry of O and Se, i.e., $Bi_2O_{2-\delta}Se_{1+\delta}$[394] are also proposed to enhance thermoelectric properties. Maximum ZT has been reported to be 0.69 at 770 K for $Bi_2O_{2-2x}Te_{2x}Se$ ($x = 0.02$) bulk polycrystals, which is synthesized by shear exfoliation methods [Fig. 17(a)].[395] The shear exfoliation induced nanograins, point defects, and impurities, resulting in an ultra-low lattice thermal conductivity of ~0.57 W m^{-1} K^{-1} at 773 K [Fig. 17(b)].

Phonon calculations suggest that the low lattice thermal conductivity of Bi_2O_2Ch originates from large anharmonic coupling between Bi and *Ch* atoms.[396] Larger Grüneisen parameter is obtained for Bi and *Ch* atoms compared to O atoms, suggesting that inter-layer Bi–*Ch* bonding is strongly anharmonic and generates stronger phonon scattering. In the structure of Bi_2OCh_2, each *Ch* atom is surrounded by eight Bi atoms. Due to inter-layer charge transfer, the *Ch* atom interacts mainly through electrostatic force with surrounding Bi atoms, forming weak ionic bonds. The Bi atom has lone-pair electrons, which also contribute to the inter-layer coupling.

There have been limited reports on the thermoelectric properties of sister compounds Bi_2O_2Ch (*Ch* = S and Te), currently. Bi_2O_2Te is also n-type semiconductor with bandgap of 0.23 eV, and its polycrystal shows high electron mobility ~47 cm^2 V^{-1} s^{-1} at RT.[397] Bi_2O_2Te bulk exhibits low total thermal conductivity of 0.91 W m^{-1} K^{-1} at RT, and maximum ZT is measured to be 0.13 at 573 K. Phonon calculation predicts that Bi_2O_2S show much lower lattice thermal conductivity of 0.8 W m^{-1} K^{-1} for in-layer direction and 0.4 W m^{-1} K^{-1} for inter-layer direction.[396] Usually, lattice thermal conductivity increases with increasing constituent atomic mass for similar lattice structure, but Bi_2O_2S has the lattice distortion by the shift of Bi atom, which enhances the anharmonic inter-layer coupling between Bi and S atoms and results in the lowest lattice thermal conductivity among this series.

Recently, there has been great attention on thermoelectricity in Bi_2O_2Se ultrathin 2D crystals. Gate-tunable PF as high as ~160 μW m^{-1} K^{-2} at RT was reported in atomically thin Bi_2O_2Se films.[398] In addition, there is a theoretical prediction that strain along in-layer direction can enhance ZT in Bi_2O_2Se.[399] Growing the thin films on various substrates with different lattice mismatches may demonstrate such ZT enhancement. 2D Bi_2O_2Se crystals can be formed on flexible substrates,[400] leading to the potential applications, such as flexible thermoelectric devices.

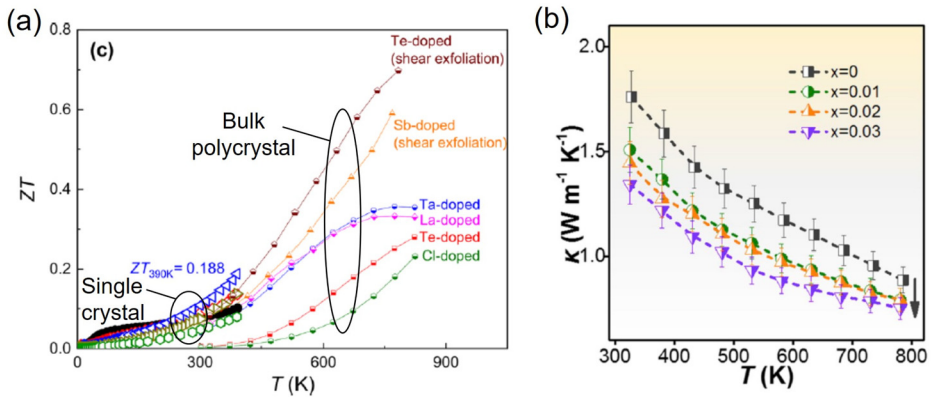

FIG. 17. (a) Temperature dependence of ZT for $Bi_2O_2Se_{1-x}Cl_x$ polycrystal,[390] $Bi_2O_2Se_{1-x}Te_x$ polycrystal,[391] $Bi_{2-x}La_xO_2Se$ polycrystal,[391] $Bi_{2-x}Ta_xO_2Se$ polycrystal,[388] shear exfoliated $Bi_{2-x}Sb_xO_2Se$ polycrystal,[392] shear exfoliated $Bi_2O_{2-2x}Te_{2x}Se$ polycrystal,[395] and Bi_2O_2Se single crystal.[383] Reproduced with permission from Wang *et al.*, Appl. Phys. Lett. **119**(8), 081901 (2021). Copyright 2021 AIP Publishing.[383] (b) Temperature dependence of thermal conductivity (κ) for shear exfoliated $Bi_2O_{2-2x}Te_{2x}Se$ ($x = 0$–0.03) bulk polycrystals. Reproduced with permission from Pan *et al.*, Nano Energy **69**, 104394 (2020). Copyright 2020 Elsevier Ltd.[395]

C. Mixed-anion compounds with heteroleptic polyhedra

Heteroleptic coordination environment in mixed-anion materials, where more than one anionic species is bonded to a cation, have various roles in determining their physical properties as well as crystal chemistry. The expanded degrees of freedom in element selection, coordination geometry, and the arrangement of basis units enable flexible control of local and overall symmetry. This flexibility markedly influences the electron and phonon band structures. Such effects derived from the heteroleptic coordination can be more prominent than homoleptic mixed-anion compounds, such as layered compounds we have discussed in Sec. III B, due to more pronounced distortion in local structures. Nonetheless, the mixed-anion materials featuring heteroleptic units are relatively scarce and challenging to synthesize, as such distorted structures frequently lead to structural instability. To address this, recent high-throughput searches have focused on the structural stability of novel heteroleptic mixed-anion materials as well as their physical properties.[404–406] Additionally, structure prediction approaches, such as evolutionary algorithm, have also been utilized to explore novel mixed-anion materials.[407,408]

In this section, we summarize the thermoelectric and thermal transport properties of mixed-anion compounds with heteroleptic local structures, based on their structural features. While some of the compounds treated in this section contain both homoleptic and heteroleptic coordination polyhedra, we mainly focus on the heteroleptic ones owing to their distinctive roles in these systems. As mentioned above, although identified mixed-anion compounds with heteroleptic structures are scarce, several compounds have been computationally predicted to exhibit superior thermoelectric properties, and some have been experimentally confirmed to have high performance. A notable common characteristic among these compounds is that the heteroleptic units have a significant impact on lattice vibrations, leading to low lattice thermal conductivity. Numerous studies, both computational and experimental, highlight ultra-low thermal conductivity values, with some being lower than 1 W m^{-1} K^{-1}.

1. Perovskite-related materials

As mentioned in Sec. III A 6, oxide perovskite-type materials with the composition of ABO_3 have been extensively studied as thermoelectric materials for many years.[262,263] For instance, the bulk polycrystals of La and Nb-doped $SrTiO_3$ perovskite with nanoscale TiO_2 precipitates exhibit a maximum ZT of 0.6 at over 1000 K.[409] Despite these advancements, the thermoelectric performance of oxide perovskites is not comparable to state-of-the-art materials like Bi_2Te_3 and PbTe-based ones, primarily due to their high lattice thermal conductivity. Recent advancements, however, include the significant reduction of lattice thermal conductivity of $SrTiO_3$ through hydride anion substitution.[265]

There exist groups of materials with more complex crystal structures derived from the perovskite structure, some of which have been explored for thermoelectric applications.[263,410–412] For example, Ruddlesden–Popper (RP) phase is represented by the formula $(ABX_3)_nAX$, where n layers of consecutive ABX_3 perovskite layers alternate with a single layer of NaCl-type AX layers. Within the RP phases, some contain multiple anions, with $[BX_6]$ octahedra replaced by mixed-anion heteroleptic coordination environment. $Cs_2PbI_2Cl_2$ crystalizes in the K_2NiF_4-type structure, the RP phase with $n = 1$, where the $CsPb(I,Cl)_3$ units are separated by a CsI layer. This configuration forms corner-shared $[PbI_2Cl_4]^{4-}$ heteroleptic units. A single crystal of $Cs_2PbI_2Cl_2$ grown by using Bridgman method exhibits exceptionally low lattice thermal conductivities of 0.37 and 0.41 W m^{-1} K^{-1} at 300 K for perpendicular and parallel to the growth direction, respectively.[413] The heterogeneous bonding environment due to the mixed covalent and ionic bonding derives low-energy localized optical phonon modes, which enhance anharmonic coupling with heat-carrying acoustic phonons. It is interesting to note that the dynamic rotation of the heteroleptic octahedra, which is responsible for the lowest-lying optical mode, is also known as a part of origins of ferroelectricity observed for some RP phases.[414–416] $Cs_3Bi_2I_6Cl_3$, belonging to another family of layered perovskites, contains $[BiI_3Cl_3]^{3-}$ heteroleptic units.[417] The lattice thermal conductivity of $Cs_3Bi_2I_6Cl_3$ single crystal displays a glass-like temperature dependence with ultra-low values of 0.20 and 0.22 W m^{-1} K^{-1} at 300 K for

perpendicular and parallel to the growth direction, respectively. The torsional motion of the $[BiI_3Cl_3]^{3-}$ heteroleptic octahedra and localized anharmonic rattling-like vibrations of Cs atoms are responsible for weakly dispersive low-energy optical phonon modes, which result in significantly low sound velocity and short phonon lifetimes.

Antiperovskite-type oxides, also known as inverse-perovskites, wherein the crystallographic sites of constituent elements in the perovskite are interchanged, typically exhibit intrinsically much lower lattice thermal conductivities than the normal perovskites. Some of this class of materials can be classified as the mixed-anion compounds because some constituent metals sometimes have unusual oxidation states and behave as anions. For instance, Ca_3SnO features O^{2-} and Sn^{4-}, with the latter representing an uncommon negative oxidation state for group-14 elements. The polycrystalline Ca_3SnO and $Ca_3Pb_{1-x}Bi_xO$ show metallic behaviors in electrical resistivity and Seebeck coefficient, and Ca_3SnO exhibits a moderate PF of 1.2 $\mu W\ cm^{-1}\ K^{-2}$ at 290 K due to its relatively large positive Seebeck coefficient. Remarkably, the lattice thermal conductivity of Ca_3SnO is 1.7 $W\ m^{-1}\ K^{-1}$ at 290 K, which is significantly lower than that of undoped perovskite oxides.[418] Very recently, orthorhombic antiperovskites Ba_3SiO and Ba_3GeO have been reported to show quite promising thermoelectric performance.[419] As shown in Fig. 18(a), these antiperovskites contain the framework comprising O–A_6 octahedron, which is softer than the B–O_6 one in normal perovskites, leading to quite low lattice thermal conductivities of 1.00 and 0.77 $W\ m^{-1}\ K^{-1}$ at 300 K for Ba_3SiO and Ba_3GeO, respectively [Fig. 18(b)]. The maximum PF values exceed 10 $\mu W\ cm^{-1}\ K^{-2}$ for both compounds, leading to high ZT values of 0.84 at 623 K for Ba_3SiO and 0.65 at 523 K for Ba_3GeO, thus highlighting the potential of this class of mixed-anion compounds in thermoelectric applications.

Despite limited experimental reports on the thermoelectric properties of antiperovskite-based materials, numerous computational studies have reported the potential of high thermoelectric performance based on DFT calculations. Oxides AE_3MO and nitrides AE_3PnN (AE = Ca, Sr, Ba; M = Ge, Sn, Pb; Pn = As, Sb, Bi) were investigated

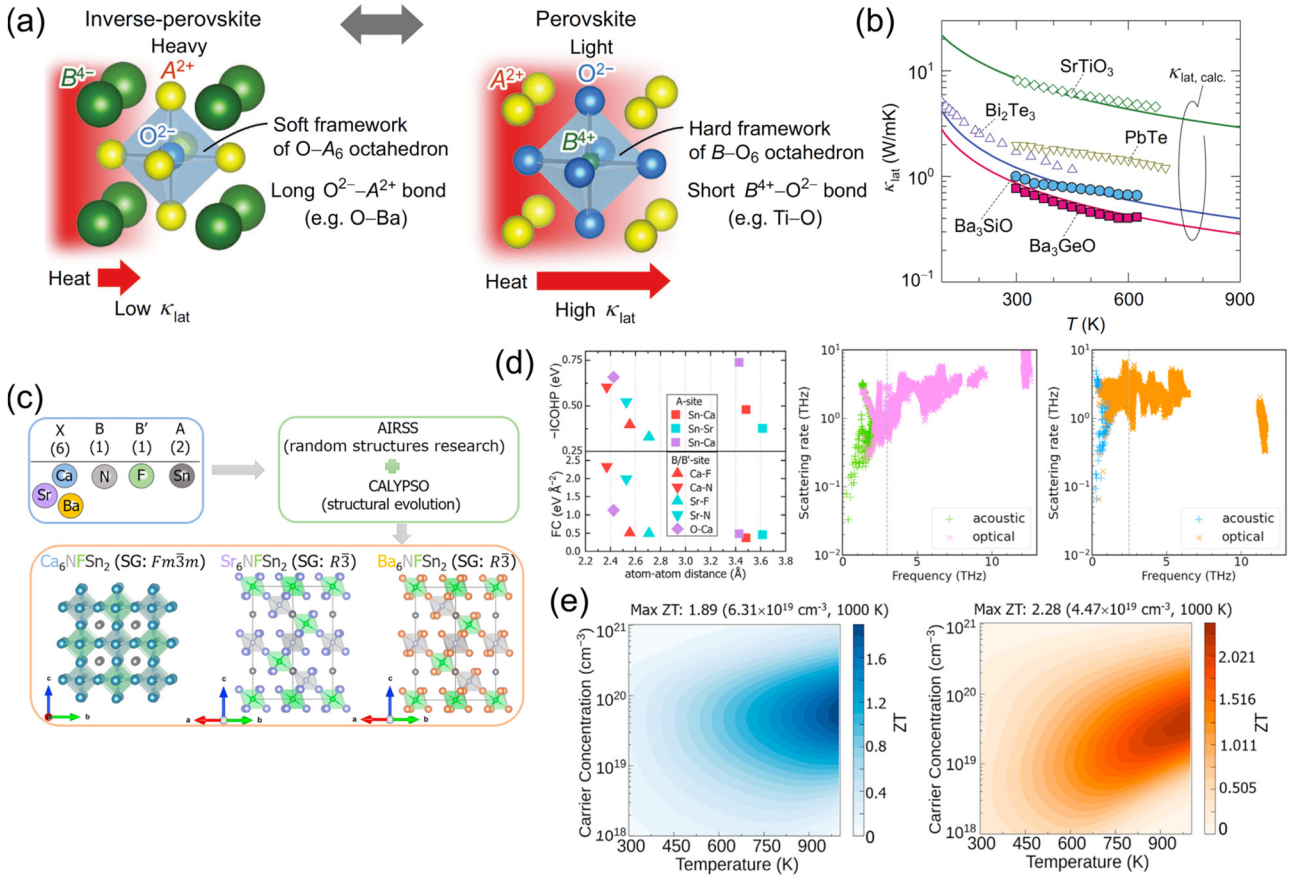

FIG. 18. (a) Comparison of crystal structure and phonon transport between inverse-perovskite (antiperovskite) A_3BO and normal perovskite ABO_3. The former contains the soft framework of O−A_6 octahedron with long O–A bonds, while the latter is built with the hard framework of B−O_6 with short B–O bonds, which consequently leads to the significant difference in thermal transport. (b) Temperature (T) dependences of the lattice thermal conductivity (κ_{lat}) for Ba_3BO polycrystalline bulk samples (B = Si, Ge), compared with the reported ones of perovskite $SrTiO_3$ as well as Bi_2Te_3 and PbTe. Reproduced with permission from He *et al.*, Adv. Sci. **11**, 2307058 (2024). Copyright 2024 Author(s), licensed under a Creative Commons Attribution (CC BY 4.0) license.[419] (c) Crystal structure prediction scheme used for discovering double-antiperovskites X_6NFSn_2 (X = Ca, Sr, Ba). (d) Analysis of the interatomic bond strength, ICOHP (integrated crystal orbital Hamilton population) and FC (interatomic force constants), and enhanced phonon scattering rate for Ca_6NFSn_2 (left) and Sr_6NFSn_2 (right). (e) Predicted p-type ZT values as a function of temperature and carrier concentration for Ca_6NFSn_2 (left) and Sr_6NFSn_2 (right); Reproduced with permission from Han *et al.*, Matter **7**, 158 (2024). Copyright 2024 Author(s), licensed under a Creative Commons Attribution (CC BY 4.0) license.[408]

by means of DFT calculations and Boltzmann transport theory. Among them, Ba_3PbO, Ca_3GeO, and Sr_3SbN are predicted to be promising thermoelectric materials due to their favorable electronic band structure.[420] Nitrides Mg_3PnN (Pn = P, As, Sb, Bi) were predicted to exhibit strong quartic anharmonicity, leading to anomalously weak temperature dependence of the lattice thermal conductivity.[421] Some other A_3BO antiperovskite oxides have also been predicted to have remarkably low lattice thermal conductivity and/or high ZT.[422–424] Furthermore, chalcohalide antiperovskites K_3ChI and Rb_3ChI (Ch = Se, Te) were predicted to have ultra-low lattice thermal conductivity below 1.0 W m^{-1} K^{-1} at 300 K, alongside high ZT value exceeding unity.[425,426] Contrary to the cubic antiperovskites mentioned above, hexagonal Bi-based AE_3BiN (AE = Ba, Sr) are forecasted to show anisotropic thermoelectric properties.[427] Considering these notably low lattice thermal conductivities observed in antiperovskites with relatively simple structures, a thorough investigation into the detailed microscopic mechanisms of phonon transport within this group is deemed highly beneficial.

More complex antiperovskite-related materials have also garnered attention for thermoelectric application. Ca_4Sb_2O and Ca_4Bi_2O with anti-K_2NiF_4 structure type, belonging to a family of anti-RP phase, are predicted to have low lattice thermal conductivity of 1.93 and 1.05 W m^{-1} K^{-1} at 300 K, respectively.[428] Such low lattice thermal conductivity is primarily attributed to the presence of low-lying optical phonon modes, causing avoided crossings with acoustic modes and large anharmonicity. Relatively small hole effective masses result in high mobility and moderate positive Seebeck coefficient, and promising ZT values approaching ~1–2 at elevated temperatures are forecasted. Very recently, double-antiperovskites AE_6NFSn_2 (AE = Ca, Sr, Ba), derived from B-site anion mutation in antiperovskite AE_3OSn, are designed by crystal structure prediction scheme, and predicted to be dynamically and thermodynamically stable [Fig. 18(c)]. Ca_6NFSn_2 (cubic) and Sr_6NFSn_2 (rhombohedral) show remarkably high p-type PFs thanks to favorable electronic structures with fourfold valley degeneracy at the VBM. With their low lattice thermal conductivity below 1.0 W m^{-1} K^{-1}, due to weak bond strength and soft lattice causing high 3-phonon scattering rate [Fig. 18(d)], these materials are anticipated to achieve high ZT values around 2.0 at 1000 K [Fig. 18(e)].[408] This successful interplay between structure prediction and transport properties calculations illuminates a wide, yet mostly unexplored "perovskite universe,"[429] rich with multiple-anion compositions.

2. Anion ordering derived from single-anion materials

Many mixed-anion materials, created through anionic substitution in single-anion frameworks, exhibit a degree of disorder despite the presence of local short-range ordered anionic groups.[117,119,430] Observations and explorations of long-range anionic order are relatively scarce; however, a select few studies have reported or predicted instances of partial or complete ordering among multiple anions.[430,431] This phenomenon of anion ordering is also identifiable in certain thermoelectric materials and materials known for their low thermal conductivity, suggesting a potential link between the anion ordering and enhanced material properties.

$CsAg_5Te_3$, a narrow-gap semiconductor with a complex three-dimensional structure, demonstrates a high ZT of 1.5 at 730 K.[432] Substitution of S for Te, resulting in $CsAg_5TeS_2$, transforms its crystal structure into a two-dimensional configuration with alternating layers of Cs^+ and $[Ag_5TeS_2]^-$ units, as shown in Fig. 19(a). The latter includes both square-planer $[AgTe_4]$ and fully-ordered heteroleptic tetrahedral $[AgTe_2S_2]$. Off-centered Ag atoms within the heteroleptic unit are confirmed by the pair distribution function analysis [Fig. 19(b)], leading to ultra-low lattice thermal conductivity of 0.40 W m^{-1} K^{-1} at 300 K [Fig. 19(c)].[433] A Similar pattern of anion ordering is found in a metallic compound $KCu_{4.2}TeS_2$, which is derived from substitution of Te for S in KCu_4S_3.[434] $Cu_{6-x}Ag_xTe_3S$, featuring heteroleptic $[CuTe_3S]$ units, shows a high ZT of 0.7 at 600 K and an ultra-low lattice thermal conductivity of 0.3 W m^{-1} K^{-1} at 300 K. The partially occupied Cu site and structural instability near phase transition play crucial role in impeding phonon transport.[435] $Ba_3Cu_{16-x}(S,Te)_{11}$, with partially ordered heteroleptic units that include (S,Te) mixing sites as well as highly mobile Cu ions [Fig. 19(d)], displays an ultra-low thermal conductivity below 0.3 W m^{-1} K^{-1} and a high ZT value of 0.88 at 745 K.[436] Low thermal conductivities and relatively high thermoelectric performances are also reported some related Ba-Cu-(S, Se, Te) system [Fig. 19(e)].[437–441] Some of bismuth sulfohalides Bi-S-X (X = Cl, Br, I) family, characterized by a local structure identical to Bi_2S_3 within their unit cell, have Bi-centered partially ordered heteroleptic polyhedra. $Bi_{13}S_{17}Br_3$ shows ultra-low thermal conductivity of 0.35 W m^{-1} K^{-1} at 300 K, though its too high semiconducting electrical resistivity limits its thermoelectric performance.[442] $Bi_{13}S_{18}I_2$ exhibits similar low thermal conductivity and much higher ZT reaching 1.0 at 800 K, while it is delicate whether it can be considered to possess heteroleptic unit because of almost isolated iodine atoms.[443]

3. Complex structures

Utilizing multiple anions tends to intrinsically yield highly complex crystal structures, which are generally unattainable with single-anion materials. Beyond the effect of heteroleptic unit described in Sec. II, these complex structures, characterized by diverse chemical bonds and huge unit cells, contain various mechanisms that hinder phonon transport, consequently leading to extremely low lattice thermal conductivity.

$Cu_{9.1}Te_4Cl_3$ features Cu-centered heteroleptic units; however, focusing on anion substructure rather elucidates its distinct crystal structure. The Cl^- anions form a Kagome lattice, while discrete Te^{2-} anions create a honeycomb network. In this structure, covalently bonded Te_2-dumbbells interpenetrate the Cl^- network.[444] The electrical resistivity and the Seebeck coefficient of this material exhibit metallic behaviors, and the thermal conductivity is quite low between 0.4 and 0.6 W m^{-1} K^{-1} in the temperature range of 300–523 K. Similar thermoelectric properties are observed for $Cu_{20}Te_{11}Cl_3$, which possesses a similar anionic substructure.[445]

As shown in Fig. 20(a), $MnPnS_2Cl$ (Pn = Sb, Bi) contains two types of highly distorted heteroleptic units, $[MnS_4Cl_2]$ and $[PnS_5Cl_2]$.[122,446,447] Bond strength between cations and anions, as represented by the interatomic force constants of the nearest atomic pair, shows a wide variety within these heteroleptic units [Fig. 20(b)]. Such kind of bonding heterogeneity often leads to a shift in phonon frequencies, where weak and strong bonds correspond to lower and higher frequencies, respectively. In materials comprising both light and heavy elements, the phonon band structure frequently has a bandgap as the phonon frequency is influenced by the constituent atomic masses. However, the frequency shift caused by the bonding

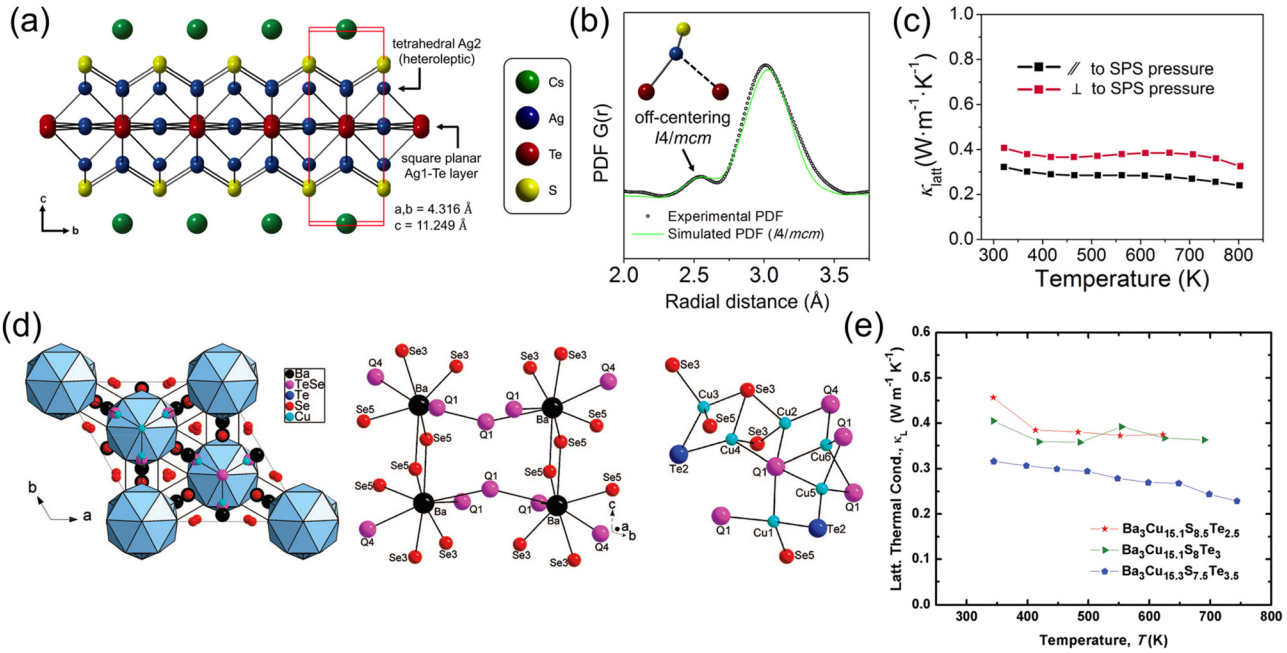

FIG. 19. (a) Crystal structure of $CsAg_5TeS_2$, showing alternating layers of Cs and heteroleptic $[Ag_5TeS_2]$ slabs. (b) Experimental and simulated pair distribution function (PDF) patterns, demonstrating off-centering of the heteroleptic Ag atom. (c) Temperature dependence of the lattice thermal conductivity (κ_{latt}) of polycrystalline $CsAg_5TeS_2$, which is measured in both the parallel and perpendicular directions relative to pressing direction during sintering. Reproduced with permission from Hodges *et al.*, Chem. Mater. **30**(20), 7245–7254 (2018). Copyright 2018 American Chemical Society.[433] (d) Crystal structure of $Ba_3Cu_{17-x}(Se,Te)_{11}$ and coordination environments of Ba-*Q* and Cu-Q (Q = Se, Te) network therein. Reproduced with permission from Kuropatwa *et al.*, Chem. Mater. **21**(1), 88–93 (2009). Copyright 2009 American Chemical Society.[438] (e) Temperature dependence of the lattice thermal conductivity (κ_L) of $Ba_3Cu_{17-x}(Se,Te)_{11}$ polycrystalline samples. Reproduced with permission from Jafarzadeh *et al.*, J. Mater. Chem. C **6**(47), 13043–13048 (2018). Copyright 2018 The Royal Society of Chemistry.[436]

heterogeneity can fill such gaps, which results in an increase in 3-phonon scattering phase space and a decrease in relaxation time [Fig. 20(c)]. This mechanism contributes to the ultra-low thermal conductivity of polycrystalline $MnPnS_2Cl$, which takes 0.5 W m^{-1} K^{-1} at 300 K, despite their relatively light constituent elements [Fig. 20(d)]. A similar effect is observed in layered *TM*NCl (*TM* = Zr, Hf).[448] A larger lattice thermal conductivity is predicted for HfNCl than ZrNCl, despite the atomic mass of Hf being much larger than Zr. This behavior was found to be attributed to the lanthanide-contraction effect, in which Hf and Zr have a similar radius, leading to a stronger bond of Hf–N than Zr–N. Consequently, the phonon bandgap is broadened for HfNCl, which suppresses the phonon scattering channel. Very recently, a novel chalcohalide $CuBiSeCl_2$, containing $[CuSe_2Cl_4]$ and $[BiSe_2Cl_6]$ heteroleptic polyhedra,[449] which is analogous to $MnPnS_2Cl$, was synthesized via a solid state reaction. The polycrystalline sample exhibits a surprisingly low thermal conductivity of 0.27 W m^{-1} K^{-1} at 300 K, which can be mainly attributed to the bonding heterogeneity within the heteroleptic units.

Within certain homologous compounds, complex local structures comprised of different multiple homoleptic units can be effectively regarded as the heteroleptic units. $Bi_{2+2n}O_{2+2n}Cu_{2-\delta}Se_{2+n-\delta}X_\delta$ (X = Cl, Br), a homologous series containing three anions, is built from the parent blocks of BiCuOSe and Bi_2O_2Se [Fig. 21(a)], both of which are recognized as homoleptic mixed-anion compounds.[450,451] Polycrystalline $Bi_4O_4Cu_{1.7}Se_{2.7}Cl_{0.3}$ was reported to exhibit low lattice thermal conductivity value of 0.4 W m^{-1} K^{-1}, which is lower than that of both BiCuOSe and Bi_2O_2Se.[450] Such low lattice thermal conductivity is able to be further reduced by adjusting the composition within this homologous series, ranging from 0.2 to 0.3 W m^{-1} K^{-1}.[451] Moreover, the bulk superlattice material $Bi_4O_4SeCl_2$, composed of BiOCl and Bi_2O_2Se blocks [Fig. 21(b)], exhibits extremely low thermal conductivity of 0.1 W m^{-1} K^{-1} for perpendicular direction to the pellet plane.[452] In this material, different types of chemical bonding anisotropy exist in each parent block, together with mismatched van der Waals interfaces in between, leading to soft anharmonic transverse acoustic phonons [Fig. 21(c)] and ultimately low lattice thermal conductivity, among the lowest for any bulk inorganic materials [Fig. 21(d)].[452,453] Carrier doping by Sn substitution for Bi improves the PF and *ZT* value, though the still low electrical conductivity limits its thermoelectric performance.[454] $Bi_4O_4SeBr_2$, analogous to $Bi_4O_4SeCl_2$, and $Bi_6O_6Se_2Cl_2$, containing an additional Bi_2O_2Se layer, also show quite low lattice thermal conductivities lower than 0.2 W m^{-1} K^{-1}.[455,456] More complex layered material $Bi_8CsO_8SeX_7$ (X = Cl, Br), containing a partially occupied large cation Cs site, shows similar values of 0.27 and 0.22 W m^{-1} K^{-1}, respectively.[457] As described above, materials containing complex heteroleptic local structures assembled from simpler homoleptic units exist within a rich compositional space and incorporate various factors that inhibit phonon transport due to the complexity and anisotropy of chemical bonding, making them worthy of exploration as low thermal conductivity materials and thermoelectric materials.

As an illustrative case in which homoleptic and heteroleptic coordination polyhedra coexist within a single structure, we highlight

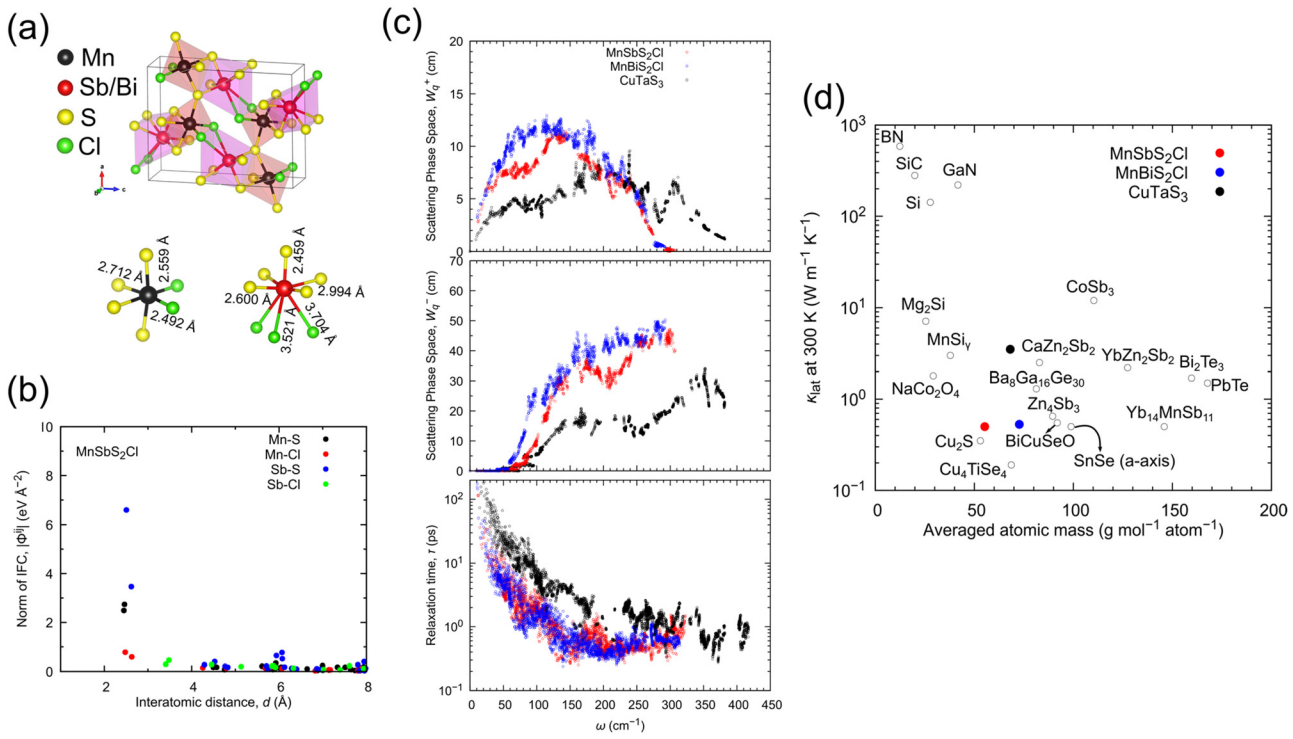

FIG. 20. (a) Crystal structure of Mn*Pn*S_2Cl (*Pn* = Sb, Bi), and the heteroleptic coordination polyhedra around Mn and Sb/Bi cations. (b) Norm of the IFC (interatomic force constants) matrix, $|\Phi^{ij}|$, as a function of interatomic distance between atoms denoted as *i* and *j* for $MnSbS_2Cl$. (c) Three-phonon scattering phase space for absorption and emission processes, and relaxation time as a function of phonon frequency. (d) Lattice thermal conductivities (κ_{lat}) at 300 K for Mn*Pn*S_2Cl are plotted against the averaged atomic mass of the constituent elements, together with that for various compounds, showing that Mn*Pn*S_2Cl features ultra-low lattice thermal conductivity considering their relatively lightweight. Reproduced with permission from Sato *et al.*, J. Mater. Chem. A **9**(39), 22660–22669 (2021). Copyright 2021 The Royal Society of Chemistry.[122]

$Sr_6Ge_3OSe_{11}$. The crystal structure [Fig. 22(a)] contains two Ge-centered tetrahedra of comparable coordination environment: a heteroleptic $[GeOSe_3]^{4-}$ unit and a homoleptic $[GeSe_4]^{4-}$ unit [Fig. 22(b)]. Because these motifs involve the same cation (Ge) and the same coordination number (four) while differing only in whether the coordination is heteroleptic or homoleptic, this compound provides one of the clearest exemplars of the "intermediate" category discussed here. Similar to the heteroleptic compounds mentioned so far, $Sr_6Ge_3OSe_{11}$ exhibits a low thermal conductivity of about 0.57 W m^{-1} K^{-1} at 300 K [Fig. 22(c)].[121]

In addition to the materials described above, there are several materials with complex crystal structures containing heteroleptic units that exhibit very low lattice thermal conductivities. Considering the difficulty in categorizing them based on structural features, they are listed in Table III.[121,458–469] Some of the materials in the list have only been predicted to have low thermal conductivities and have not been confirmed experimentally.

4. Janus TMDCs monolayer

Janus transition metal dichalcogenides (TMDCs), which consist of a transition metal and two different types of chalcogens with a heteroleptic coordination, have recently attracted growing attention for their additional degree of freedom to tune physical properties, including Rashba-type spin splitting and enhanced photocatalytic activity.[470–472] There is an experimental report of a Seebeck coefficient measurement of a Janus MoSSe monolayer sample.[473] Additionally, theoretical studies have extensively explored the thermoelectric performance of the Janus monolayer TMDCs.[474,475] For instance, Janus monolayer WSTe and WSSe were predicted to show lower lattice thermal conductivity than that of a traditional monolayer WS_2. Moreover, a remarkably high *ZT* value exceeding 2 is forecasted for WSTe.[474] Similarly, monolayer In_2SO and In_2SeO are also predicted to exhibit promising *ZT* values approaching 1. Although most of the high thermoelectric performance in this group is currently limited to computational predictions, these materials present a promising platform for thermoelectric applications requiring device flexibility.

IV. SUMMARY AND OUTLOOK

In summary, we comprehensively highlighted the recent advances, characteristics, and thermoelectric properties of mixed-anion thermoelectric materials and discussed the mixed-anion effect on electron and phonon transport. We provided an overview of the historical approach of multiple-anion substitutions onto single-anion compounds and discussed substantial impacts of multiple anion substitutions across different material systems. Then, we reviewed the characteristics of crystal structures and physical properties, as well as the recent advances in thermoelectric properties for the mixed-anion compounds with homoleptic polyhedra and heteroleptic polyhedra.

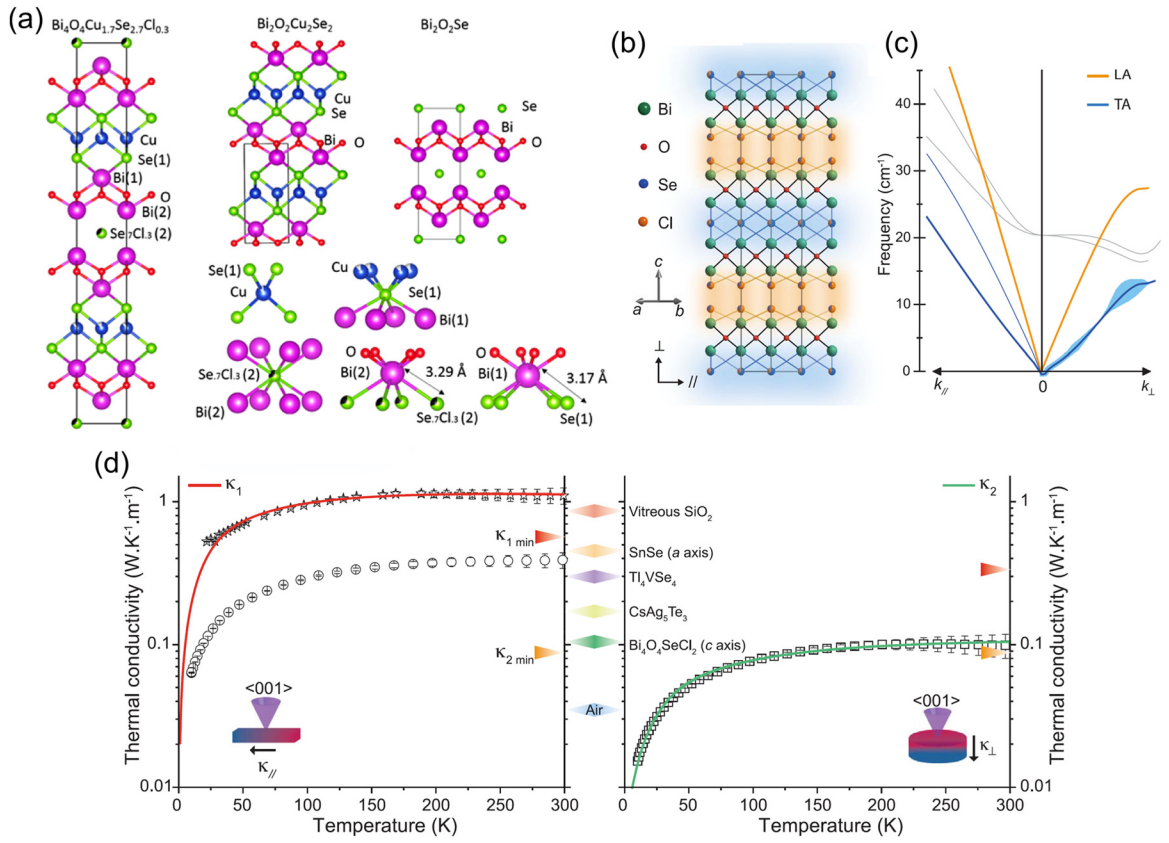

FIG. 21. (a) Crystal structure of $Bi_4O_4Cu_{1.7}Se_{2.7}Cl_{0.3}$ and the constituent parent blocks, BiOCuSe and Bi_2O_2Se, together with the coordination polyhedra therein. Reproduced with permission from Gibson *et al.*, J. Am. Chem. Soc. **139**(44), 15568–15571 (2017). Copyright 2017 American Chemical Society.[450] (b) Crystal structure of $Bi_4O_4SeCl_2$, highlighting the three types of interfaces. (c) Calculated low-frequency phonon dispersion of $Bi_4O_4SeCl_2$, highlighting the longitudinal acoustic (LA) and the transverse acoustic (TA) modes. (d) Temperature dependence of the thermal conductivity of a pressed pellet of $Bi_4O_4SeCl_2$ parallel (left, also including the in-plane single-crystal thermal conductivity) and perpendicular (right) to the pellet plane. Data for some other low-thermal conductivity bulk inorganic materials and air are also shown. Reproduced with permission from Gibson *et al.*, Science **373**(6558), 1017–1022 (2021). Copyright 2021 AAAS.[452]

Here, we would like to outline the characteristics of the mixed-anion thermoelectric materials as follows.

A. Multiple-anion substitution onto single-anion compounds

The solid solution of anions with different sizes, masses, electronegativity, etc., has significant effects on the modulation of electronic and/or phonon band structures as well as the formation energy of donor or acceptor type defects. Even isovalent anion alloying enables a wide range control of carrier concentration by the modulation of formation energy of donor/acceptor type defects, such as $Bi_2(S,Se,Te)_3$[134] and Sn(S,Se,Te).[198–200] The alloying enables the band structure engineering to optimize PF by enhancing valley degeneracy, which is represented by Pb(Se,Te).[8] The anion substitution often leads to a significant reduction in the lattice thermal conductivity that cannot be explained solely by simple mass contrast alloy scattering. Such reduction can be attributed to the distorted local structures formed by different anions, as exemplified by the differences in bond lengths and strengths between Ti-O and Ti-H in hydride-substituted $SrTiO_3$.[265] Mechanical properties can be tuned by the anion substitutions as well as thermoelectric properties, such as $Ag_2(S,Se,Te)$.[225] The classical Hume-Rothery rule suggests that anions with significantly different radii or electronegativities are unlikely to form solid solutions, leading to phase separation. However, recent studies have identified several metastable cases where solid solutions are possible, depending on the diffusion coefficients of cations and anions.[218] Such findings are expected to further expand the degree of freedom to tune thermoelectric properties through anion solid solution.

B. Mixed-anion compounds with homoleptic polyhedra

Mixed-anion compounds containing multiple anions that exhibit different bonding characteristics to cations, with some forming predominantly ionic bonds and others forming predominantly covalent bonds, often adopt complex crystal structures characterized by the coexistence of bonds with varying degrees of ionicity and covalency within a single phase, which can sometimes lead to separation into distinct structural blocks. For example, their mixed-anionic yet

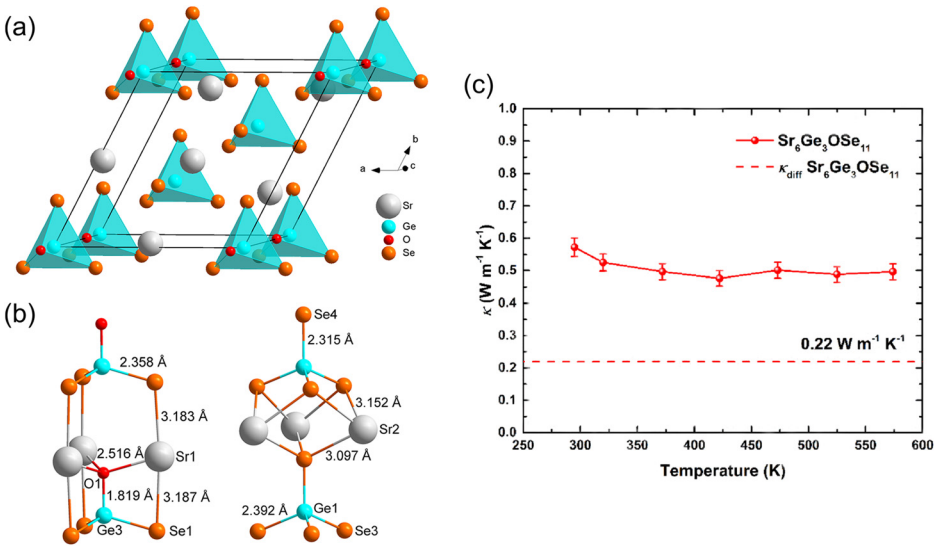

FIG. 22. (a) Crystal structure of $Sr_6Ge_3OSe_{11}$, (b) coordination environments and bond distances of the heteroleptic $[GeOSe_3]^{4-}$ unit (left) and the homoleptic $[GeSe_4]^{4-}$ unit (right), (c) temperature dependence of the thermal conductivity (κ) together with theoretical lower limit (κ_{diff}). Reproduced with permission from Menezes *et al.*, Chem. Mater. **35**(7), 3033–3040 (2023). Copyright 2023 American Chemical Society.[121]

homoleptic polyhedral nature of these compounds tends to intrinsically drive the formation of layered block-structures. As a result, the mixed-anion layered compounds are composed of separate building blocks with different chemical, electronic, and phonon properties, which enable specific thermoelectric properties. BiCuOSe naturally forms superlattice structure consisting of widegap insulating oxide layers and highly conducting chalcogenide layers. The O and Se anions do not mix with each other, but form separate layers with homoleptic O-Bi_4 and Cu-Se_4 polyhedra. The 2D layered structure and hierarchical bond feature provide them with low lattice thermal conductivity, low-dimensional electrical features, and anisotropic electron and phonon transport behaviors. The quantum confinement of carriers in layered superlattice leads to a 2D electronic structure and enhanced Seebeck coefficient. The carrier concentrations can be controlled by aliovalent ion substitution at the insulating blocking layer without deteriorating electronic conductivity in carrier transport layer. The quite anisotropic chemical bonds between strong intralayer and weak interlayer bonds cause a large anharmonicity, large anisotropic

TABLE III. Lattice thermal conductivity (κ_{lat}) of various mixed-anion compounds with complex crystal structure comprising heteroleptic units.

Material	κ_{lat} (W m^{-1} K^{-1}) at 300 K	Classification	Reference
Bi_2CuSe_3I	0.30	Polycrystal	458
$Y_2Ti_2O_5S_2$	7.59 (*xx*, *yy*), 2.41 (*zz*)	Calculation	459
In_5S_5Br	1.1 (average)	Calculation	460
In_5Se_5Br	0.55 (average)	Calculation	460
$Sn_2SbS_2I_3$	0.30	Polycrystal	461
$Sn_2BiS_2I_3$	0.28	Polycrystal	461
Li_4OSe	1.75 (average)	Calculation	462
CaClF	3.77 (average)	Calculation	463
SrClF	3.04 (average)	Calculation	463
PbClF	1.66 (average)	Calculation	464
PbBrF	1.14 (average)	Calculation	464
PbIF	0.90 (average)	Calculation	464
$Ba_5Sn_2Te_{1.327}S_{7.673}$	0.36	Polycrystal	465
$Ba_7Sn_3Te_{0.839}S_{12.161}$	0.38	Polycrystal	465
α-CuSCN	1.2 (average)	Calculation	466
β-CuSCN	2.4 (average)	Calculation	466
Ba_3GeTeS_4	0.57	Polycrystal	467
$Ba_{14}Si_4Sb_8Te_{32}(Te_3)$	0.50	Polycrystal	468
Ba_4Sb_2Se	0.43 (average)	Calculation	469
Ba_4Sb_2Te	0.53 (average)	Calculation	469

group velocities, and unusual atomic motion. As can be seen in layered Cu-based oxychalcogenides, Ag-based oxychalcogenides, and Bi-based oxy(fluoro)chalcogenides, they have high controllability of blocking layers and carrier transport layers by the choice of constituent elements. Not introduced in this paper, various kinds of crystal structures have been found in mixed-anion layered compounds.[120,476–480] Designing the buildup of carrier transport and blocking layers in layered structures provide an opportunity to control their electronic and phonon transport properties, which cannot be realized by conventional 3D material systems. Further enhancement of ZT can be expected by expanding the material system with other chemical compositions and different layers.

C. Mixed-anion compounds with heteroleptic polyhedra

Mixed-anion compounds featuring heteroleptic coordination polyhedra, where a single cation is coordinated by two or more different anions, are characterized by local structures that are significantly more distorted than their homoleptic counterparts. Such local symmetry breaking not only induces crystal field splitting that affects electronic band structure but also impacts phonon band structure and thermal transport due to bonding heterogeneity, where both strong and weak bonds coexist within the same coordination polyhedron. These heteroleptic structures are observed not only in materials with relatively simple crystal structures, such as perovskite-based ones, but also in anion solid solutions where different anions become ordered under specific conditions. Additionally, unique heteroleptic coordination can arise in complex crystal structures not observed in single-anion compounds. A common feature among this class of materials is their low lattice thermal conductivity. Although still relatively underexplored, they are promising candidates for thermoelectric materials. To discover new heteroleptic material groups, high-throughput screening using DFT calculations[404–406] and structure prediction schemes employing various algorithms[407,408] are being actively utilized. Furthermore, systematic searches for materials with anion ordering based on crystallographic considerations have recently also been reported.[481]

Finally, we would like to note the currently unsolved challenges and future prospects toward the development of mixed-anion thermoelectrics. The mixed-anion compounds have large degrees of freedom for the choice of the constituent anions and their arrangement, but most of which still remains unexplored. Further exploration of new mixed-anion compounds with various anions, such as hydride, nitride, halide anions, and more complex anion compositions, will be highly desirable for discovering new thermoelectric functionalities. In addition, theoretical study on exploration and analysis leads the research on mixed-anion materials, but the experimental validation using single crystals and epitaxial thin films would be beneficial for advancing deeper understanding. In particular, mixed-anion compounds with heteroleptic polyhedra have only recently gained attention as a class of ultralow lattice thermal conductivity materials. Compared to theoretical analyses, there are still relatively few experimental demonstrations of ultralow thermal conductivity and experimental analyses, such as *in situ* neutron scattering and atomic displacement parameter measurements. Therefore, further experimental verification and detailed characterization are strongly needed. Additionally, currently discovered mixed-anion compounds typically exhibit low electronic conductivity in many cases. This is especially the case with the mixed-anion compounds with heteroleptic polyhedra. While they tend to have very strong local distortions, it remains a general fact that the electronic transport and phonon transport possess different length scales. Therefore, exploration and development of innovative doping methods should be further carried out to explore the possibility of effectively enhancing the electronic transport in such compounds. Addressing these challenges will pave the way for exploring the potential applications of thermoelectric modules using mixed-anion materials in the future.

We hope this review will provide valuable insights for new design route for high performance thermoelectric materials based on mixed-anion strategy. Conventionally, thermoelectric property modification is carried out by cation site engineering. On the other hand, anion site engineering provides an additional degree of freedom to manipulate electron and phonon transport. We expect the mixed-anion strategy to offer great potential for finding new classes of high-performance thermoelectric materials.

ACKNOWLEDGMENTS

T.K. was supported by the Special Award for Science Tokyo Advanced Researchers (STAR) funded by the Institute of Science Tokyo, a project of Kanagawa Institute of Industrial Science and Technology (KISTEC), and the Japan Society for the Promotion of Science (JSPS) through Grant-in-Aids for Scientific Research (B) (Grant No. JP22H01766), the Scientific Research (S) (Grant No. JP22H04964) and the Challenging Research (Exploratory) (Grant No. JP24K21671). N.S. was supported by JSPS through Grant-in-Aid for Early-Career Scientists (Grant No. JP22K14505). N.S. and T.M. were supported by the JST Mirai Program JPMJMI19A1. Schematic images of crystal structures were drawn using the VESTA code.[482]

AUTHOR DECLARATIONS

Conflict of Interest

The authors have no conflicts to disclose.

Author Contributions

Takayoshi Katase: Conceptualization (lead); Investigation (lead); Supervision (lead); Visualization (lead); Writing – original draft (lead). **Naoki Sato:** Conceptualization (equal); Investigation (equal); Supervision (equal); Visualization (equal); Writing – original draft (equal). **Takao Mori:** Conceptualization (equal); Investigation (equal); Supervision (equal); Visualization (equal); Writing – original draft (equal).

DATA AVAILABILITY

Data sharing is not applicable to this article as no new data were created or analyzed in this study.

REFERENCES

[1]F. J. DiSalvo, "Thermoelectric cooling and power generation," Science **285**(5428), 703–706 (1999).
[2]L. E. Bell, "Cooling, heating, generating power, and recovering waste heat with thermoelectric systems," Science **321**(5895), 1457–1461 (2008).

[3]Q. H. Zhang, X. Y. Huang, S. Q. Bai, X. Shi, C. Uher, and L. D. Chen, "Thermoelectric devices for power generation: Recent progress and future challenges," Adv. Eng. Mater. **18**(2), 194–213 (2016).
[4]H. J. Goldsmid, *Introduction to Thermoelectricity*, 2nd ed. (Springer, Berlin, Germany, 2016).
[5]G. J. Snyder and E. S. Toberer, "Complex thermoelectric materials," Nat. Mater. **7**(2), 105–114 (2008).
[6]J. P. Heremans, V. Jovovic, E. S. Toberer, A. Saramat, K. Kurosaki, A. Charoenphakdee, S. Yamanaka, and G. J. Snyder, "Enhancement of thermoelectric efficiency in PbTe by distortion of the electronic density of states," Science **321**(5888), 554–557 (2008).
[7]M. Hong, Z.-G. Chen, L. Yang, Z.-M. Liao, Y.-C. Zou, Y.-H. Chen, S. Matsumura, and J. Zou, "Achieving $zT > 2$ in p-type $AgSbTe_{2-x}Se_x$ alloys via exploring the extra light valence band and introducing dense stacking faults," Adv. Energy Mater. **8**(9), 1702333 (2018).
[8]Y. Pei, X. Shi, A. LaLonde, H. Wang, L. Chen, and G. J. Snyder, "Convergence of electronic bands for high performance bulk thermoelectrics," Nature **473**(7345), 66–69 (2011).
[9]X. Liu, T. Zhu, H. Wang, L. Hu, H. Xie, G. Jiang, G. J. Snyder, and X. Zhao, "Low electron scattering potentials in high performance $Mg_2Si_{0.45}Sn_{0.55}$ based thermoelectric solid solutions with band convergence," Adv. Energy Mater. **3**(9), 1238–1244 (2013).
[10]J.-B. Vaney, S. Aminorroaya Yamini, H. Takaki, K. Kobayashi, N. Kobayashi, and T. Mori, "Magnetism-mediated thermoelectric performance of the Cr-doped bismuth telluride tetradymite," Mater. Today Phys. **9**, 100090 (2019).
[11]T. C. Harman, P. J. Taylor, M. P. Walsh, and B. E. LaForge, "Quantum dot superlattice thermoelectric materials and devices," Science **297**(5590), 2229–2232 (2002).
[12]B. Poudel, Q. Hao, Y. Ma, Y. Lan, A. Minnich, B. Yu, X. Yan, D. Wang, A. Muto, D. Vashaee, X. Chen, J. Liu, M. S. Dresselhaus, G. Chen, and Z. Ren, "High-thermoelectric performance of nanostructured bismuth antimony telluride bulk alloys," Science **320**(5876), 634–638 (2008).
[13]T. Plirdpring, K. Kurosaki, A. Kosuga, M. Ishimaru, A. Harnwunggmoung, T. Sugahara, Y. Ohishi, H. Muta, and S. Yamanaka, "Effect of the amount of vacancies on the thermoelectric properties of Cu–Ga–Te ternary compounds," Mater. Trans. **53**(7), 1212–1215 (2012).
[14]W. Li, S. Lin, X. Zhang, Z. Chen, X. Xu, and Y. Pei, "Thermoelectric properties of Cu_2SnSe_4 with intrinsic vacancy," Chem. Mater. **28**(17), 6227–6232 (2016).
[15]S. N. Guin and K. Biswas, "Cation disorder and bond anharmonicity optimize the thermoelectric properties in kinetically stabilized rocksalt $AgBiS_2$ nanocrystals," Chem. Mater. **25**(15), 3225–3231 (2013).
[16]Y. Pei, J. Lensch-Falk, E. S. Toberer, D. L. Medlin, and G. J. Snyder, "High thermoelectric performance in PbTe due to large nanoscale Ag_2Te precipitates and la doping," Adv. Funct. Mater. **21**(2), 241–249 (2011).
[17]M. Hong, T. C. Chasapis, Z.-G. Chen, L. Yang, M. G. Kanatzidis, G. J. Snyder, and J. Zou, "N-type $Bi_2Te_{3-x}Se_x$ nanoplates with enhanced thermoelectric efficiency driven by wide-frequency phonon scatterings and synergistic carrier scatterings," ACS Nano **10**(4), 4719–4727 (2016).
[18]L. Yang, Z.-G. Chen, G. Han, M. Hong, Y. Zou, and J. Zou, "High-performance thermoelectric Cu_2Se nanoplates through nanostructure engineering," Nano Energy **16**, 367–374 (2015).
[19]A. U. Khan, K. Kobayashi, D.-M. Tang, Y. Yamauchi, K. Hasegawa, M. Mitome, Y. Xue, B. Jiang, K. Tsuchiya, D. Golberg, Y. Bando, and T. Mori, "Nano-micro-porous skutterudites with 100% enhancement in ZT for high performance thermoelectricity," Nano Energy **31**(November 2016), 152–159 (2017).
[20]K. Zhao, H. Duan, N. Raghavendra, P. Qiu, Y. Zeng, W. Zhang, J. Yang, X. Shi, and L. Chen, "Solid-state explosive reaction for nanoporous bulk thermoelectric materials," Adv. Mater. **29**(42), 1701148 (2017).
[21]L.-D. Zhao, S.-H. Lo, Y. Zhang, H. Sun, G. Tan, C. Uher, C. Wolverton, V. P. Dravid, and M. G. Kanatzidis, "Ultralow thermal conductivity and high thermoelectric figure of merit in SnSe crystals," Nature **508**(7496), 373–377 (2014).
[22]H. Liu, X. Shi, F. Xu, L. Zhang, W. Zhang, L. Chen, Q. Li, C. Uher, T. Day, and G. J. Snyder, "Copper ion liquid-like thermoelectrics," Nat. Mater. **11**(5), 422–425 (2012).
[23]S. Roychowdhury, M. K. Jana, J. Pan, S. N. Guin, D. Sanyal, U. V. Waghmare, and K. Biswas, "Soft phonon modes leading to ultralow thermal conductivity and high thermoelectric performance in AgCuTe," Angew. Chem. Int. Ed. **57**(15), 4043–4047 (2018).
[24]B. Li, H. Wang, Y. Kawakita, Q. Zhang, M. Feygenson, H. L. Yu, D. Wu, K. Ohara, T. Kikuchi, K. Shibata, T. Yamada, X. K. Ning, Y. Chen, J. Q. He, D. Vaknin, R. Q. Wu, K. Nakajima, and M. G. Kanatzidis, "Liquid-like thermal conduction in intercalated layered crystalline solids," Nat. Mater. **17**(3), 226–230 (2018).
[25]D. T. Morelli, V. Jovovic, and J. P. Heremans, "Intrinsically minimal thermal conductivity in cubic I-V-VI2 semiconductors," Phys. Rev. Lett. **101**(3), 035901 (2008).
[26]M. Dutta, K. Pal, U. V. Waghmare, and K. Biswas, "Bonding heterogeneity and lone pair induced anharmonicity resulted in ultralow thermal conductivity and promising thermoelectric properties in n-type $AgPbBiSe_3$," Chem. Sci. **10**(18), 4905–4913 (2019).
[27]H. Xie, S. Hao, J. Bao, T. J. Slade, G. J. Snyder, C. Wolverton, and M. G. Kanatzidis, "All-inorganic halide perovskites as potential thermoelectric materials: Dynamic cation off-centering induces ultralow thermal conductivity," J. Am. Chem. Soc. **142**(20), 9553–9563 (2020).
[28]M. Dutta, K. Pal, M. Etter, U. V. Waghmare, and K. Biswas, "Emphanisis in cubic $(SnSe)_{0.5}(AgSbSe_2)_{0.5}$: Dynamical off-centering of anion leads to low thermal conductivity and high thermoelectric performance," J. Am. Chem. Soc. **143**(40), 16839–16848 (2021).
[29]A. Banik, T. Ghosh, R. Arora, M. Dutta, J. Pandey, S. Acharya, A. Soni, U. V. Waghmare, and K. Biswas, "Engineering ferroelectric instability to achieve ultralow thermal conductivity and high thermoelectric performance in $Sn_{1-x}Ge_xTe$," Energy Environ. Sci. **12**(2), 589–595 (2019).
[30]D. Sarkar, T. Ghosh, S. Roychowdhury, R. Arora, S. Sajan, G. Sheet, U. V. Waghmare, and K. Biswas, "Ferroelectric instability induced ultralow thermal conductivity and high thermoelectric performance in rhombohedral p-type GeSe crystal," J. Am. Chem. Soc. **142**(28), 12237–12244 (2020).
[31]M. D. Nielsen, V. Ozolins, and J. P. Heremans, "Lone pair electrons minimize lattice thermal conductivity," Energy Environ. Sci. **6**(2), 570–578 (2013).
[32]T. Takabatake, K. Suekuni, T. Nakayama, and E. Kaneshita, "Phonon-glass electron-crystal thermoelectric clathrates: Experiments and theory," Rev. Mod. Phys. **86**(2), 669–716 (2014).
[33]G. A. Slack, *New Materials and Performance Limits for Thermoelectric Cooling* (CRC Press, 1995).
[34]S. I. Kim, K. H. Lee, H. A. Mun, H. S. Kim, S. W. Hwang, J. W. Roh, D. J. Yang, W. H. Shin, X. S. Li, Y. H. Lee, G. J. Snyder, and S. W. Kim, "Thermoelectrics. Dense dislocation arrays embedded in grain boundaries for high-performance bulk thermoelectrics," Science **348**(6230), 109–114 (2015).
[35]L. Hu, H. Wu, T. Zhu, C. Fu, J. He, P. Ying, and X. Zhao, "Tuning multiscale microstructures to enhance thermoelectric performance of n-type bismuth-telluride-based solid solutions," Adv. Energy Mater. **5**(17), 1500411 (2015).
[36]J. Mao, H. Zhu, Z. Ding, Z. Liu, G. A. Gamage, G. Chen, and Z. Ren, "High thermoelectric cooling performance of n-type Mg_3Bi_2-based materials," Science **365**(6452), 495–498 (2019).
[37]Z. Liu, W. Gao, H. Oshima, K. Nagase, C.-H. Lee, and T. Mori, "Maximizing the performance of n-type Mg_3Bi_2 based materials for room-temperature power generation and thermoelectric cooling," Nat. Commun. **13**(1), 1120 (2022).
[38]H. Cho, S. Y. Back, N. Sato, Z. Liu, W. Gao, L. Wang, H. D. Nguyen, N. Kawamoto, and T. Mori, "Outstanding room-temperature thermoelectric performance of n-type Mg_3Bi_2-based compounds through synergistically combined band engineering approaches," Adv. Funct. Mater. **34**(44), 2407017 (2024).
[39]H. Zhao, J. Sui, Z. Tang, Y. Lan, Q. Jie, D. Kraemer, K. McEnaney, A. Guloy, G. Chen, and Z. Ren, "High thermoelectric performance of MgAgSb-based materials," Nano Energy **7**, 97–103 (2014).
[40]A. Li, L. Wang, J. Li, and T. Mori, "Global softening to manipulate sound velocity for reliable high-performance MgAgSb thermoelectrics," Energy Environ. Sci. **17**(22), 8810–8819 (2024).
[41]K. F. Hsu, S. Loo, F. Guo, W. Chen, J. S. Dyck, C. Uher, T. Hogan, E. K. Polychroniadis, and M. G. Kanatzidis, "Cubic $AgPb_mSbTe_{2+m}$: Bulk

thermoelectric materials with high figure of merit," Science **303**(5659), 818–821 (2004).
[42]A. D. LaLonde, Y. Pei, H. Wang, and G. Jeffrey Snyder, "Lead telluride alloy thermoelectrics," Mater. Today **14**(11), 526–532 (2011).
[43]L.-D. Zhao, J. He, S. Hao, C.-I. Wu, T. P. Hogan, C. Wolverton, V. P. Dravid, and M. G. Kanatzidis, "Raising the thermoelectric performance of p-type PbS with endotaxial nanostructuring and valence-band offset engineering using CdS and ZnS," J. Am. Chem. Soc. **134**(39), 16327–16336 (2012).
[44]L.-D. Zhao, J. He, C.-I. Wu, T. P. Hogan, X. Zhou, C. Uher, V. P. Dravid, and M. G. Kanatzidis, "Thermoelectrics with earth abundant elements: High performance p-type PbS nanostructured with SrS and CaS," J. Am. Chem. Soc. **134**(18), 7902–7912 (2012).
[45]J. He, S. N. Girard, J.-C. Zheng, L. Zhao, M. G. Kanatzidis, and V. P. Dravid, "Strong phonon scattering by layer structured $PbSnS_2$ in PbTe based thermoelectric materials," Adv. Mater. **24**(32), 4440–4444 (2012).
[46]L.-D. Zhao, G. Tan, S. Hao, J. He, Y. Pei, H. Chi, H. Wang, S. Gong, H. Xu, V. P. Dravid, C. Uher, G. J. Snyder, C. Wolverton, and M. G. Kanatzidis, "Ultrahigh power factor and thermoelectric performance in hole-doped single-crystal SnSe," Science **351**(6269), 141–144 (2016).
[47]H. Wu, X. Lu, G. Wang, K. Peng, H. Chi, B. Zhang, Y. Chen, C. Li, Y. Yan, L. Guo, C. Uher, X. Zhou, and X. Han, "Sodium-doped tin sulfide single crystal: A nontoxic earth-abundant material with high thermoelectric performance," Adv. Energy Mater. **8**(20), 1800087 (2018).
[48]L.-D. Zhao, X. Zhang, H. Wu, G. Tan, Y. Pei, Y. Xiao, C. Chang, D. Wu, H. Chi, L. Zheng, S. Gong, C. Uher, J. He, and M. G. Kanatzidis, "Enhanced thermoelectric properties in the counter-doped SnTe system with strained endotaxial SrTe," J. Am. Chem. Soc. **138**(7), 2366–2373 (2016).
[49]Q. Zhang, B. Liao, Y. Lan, K. Lukas, W. Liu, K. Esfarjani, C. Opeil, D. Broido, G. Chen, and Z. Ren, "High thermoelectric performance by resonant dopant indium in nanostructured SnTe," Proc. Natl. Acad. Sci. U. S. A. **110**(33), 13261–13266 (2013).
[50]D. Wu, L.-D. Zhao, S. Hao, Q. Jiang, F. Zheng, J. W. Doak, H. Wu, H. Chi, Y. Gelbstein, C. Uher, C. Wolverton, M. Kanatzidis, and J. He, "Origin of the high performance in GeTe-based thermoelectric materials upon Bi_2Te_3 doping," J. Am. Chem. Soc. **136**(32), 11412–11419 (2014).
[51]C. Liu, Z. Zhang, Y. Peng, F. Li, L. Miao, E. Nishibori, R. Chetty, X. Bai, R. Si, J. Gao, X. Wang, Y. Zhu, N. Wang, H. Wei, and T. Mori, "Charge transfer engineering to achieve extraordinary power generation in GeTe-based thermoelectric materials," Sci. Adv. **9**(17), eadh0713 (2023).
[52]Y. He, P. Lu, X. Shi, F. Xu, T. Zhang, G. J. Snyder, C. Uher, and L. Chen, "Ultrahigh thermoelectric performance in mosaic crystals," Adv. Mater. **27**(24), 3639–3644 (2015).
[53]W. Liu, X. Tan, K. Yin, H. Liu, X. Tang, J. Shi, Q. Zhang, and C. Uher, "Convergence of conduction bands as a means of enhancing thermoelectric performance of n-type $Mg_2Si_{1-x}Sn_x$ solid solutions," Phys. Rev. Lett. **108**(16), 166601 (2012).
[54]W. Liu, H. S. Kim, S. Chen, Q. Jie, B. Lv, M. Yao, Z. Ren, C. P. Opeil, S. Wilson, C.-W. Chu, and Z. Ren, "n-type thermoelectric material $Mg_2Sn_{0.75}Ge_{0.25}$ for high power generation," Proc. Natl. Acad. Sci. U. S. A. **112**(11), 3269–3274 (2015).
[55]H. Tamaki, H. K. Sato, and T. Kanno, "Isotropic conduction network and defect chemistry in $Mg_{3+\delta}$ Sb_2-based layered Zintl compounds with high thermoelectric performance," Adv. Mater. **28**(46), 10182–10187 (2016).
[56]Z. Liu, N. Sato, W. Gao, K. Yubuta, N. Kawamoto, M. Mitome, K. Kurashima, Y. Owada, K. Nagase, C.-H. Lee, J. Yi, K. Tsuchiya, and T. Mori, "Demonstration of ultrahigh thermoelectric efficiency of ~7.3% in Mg_3Sb_2/MgAgSb module for low-temperature energy harvesting," Joule **5**(5), 1196–1208 (2021).
[57]L. Wang, N. Sato, Y. Peng, R. Chetty, N. Kawamoto, D. H. Nguyen, and T. Mori, "Realizing high thermoelectric performance in N-type $Mg_3(Sb, Bi)_2$-based materials via synergetic Mo addition and Sb–Bi ratio refining," Adv. Energy Mater. **13**(35), 2301667 (2023).
[58]L. Wang, W. Zhang, S. Y. Back, N. Kawamoto, D. H. Nguyen, and T. Mori, "High-performance Mg_3Sb_2-based thermoelectrics with reduced structural disorder and microstructure evolution," Nat. Commun. **15**(1), 6800 (2024).
[59]J. Zhang, L. Song, G. K. H. Madsen, K. F. F. Fischer, W. Zhang, X. Shi, and B. B. Iversen, "Designing high-performance layered thermoelectric materials through orbital engineering," Nat. Commun. **7**, 10892 (2016).
[60]L.-D. Zhao, J. He, D. Berardan, Y. Lin, J.-F. Li, C.-W. Nan, and N. Dragoe, "BiCuSeO oxyselenides: New promising thermoelectric materials," Energy Environ. Sci. **7**(9), 2900–2924 (2014).
[61]X. Zhang, C. Chang, Y. Zhou, and L.-D. Zhao, "BiCuSeO thermoelectrics: An update on recent progress and perspective," Materials **10**(2), 198 (2017).
[62]G. J. Snyder, M. Christensen, E. Nishibori, T. Caillat, and B. B. Iversen, "Disordered zinc in Zn_4Sb_3 with phonon-glass and electron-crystal thermoelectric properties," Nat. Mater. **3**(7), 458–463 (2004).
[63]T. Caillat, J.-P. Fleurial, and A. Borshchevsky, "Preparation and thermoelectric properties of semiconducting Zn_4Sb_3," J. Phys. Chem. Solids **58**(7), 1119–1125 (1997).
[64]J.-S. Rhyee, K. H. Lee, S. M. Lee, E. Cho, S. I. Kim, E. Lee, Y. S. Kwon, J. H. Shim, and G. Kotliar, "Peierls distortion as a route to high thermoelectric performance in $In_4Se_{3-\delta}$ crystals," Nature **459**(7249), 965–968 (2009).
[65]E. S. Toberer, M. Christensen, B. B. Iversen, and G. J. Snyder, "High temperature thermoelectric efficiency in $Ba_8Ga_{16}Ge_{30}$," Phys. Rev. B **77**(7), 075203 (2008).
[66]V. L. Kuznetsov, L. A. Kuznetsova, A. E. Kaliazin, and D. M. Rowe, "Preparation and thermoelectric properties of A8IIB16IIIB30IV clathrate compounds," J. Appl. Phys. **87**(11), 7871–7875 (2000).
[67]X. Shi, J. Yang, J. R. Salvador, M. Chi, J. Y. Cho, H. Wang, S. Bai, J. Yang, W. Zhang, and L. Chen, "Multiple-filled skutterudites: High thermoelectric figure of merit through separately optimizing electrical and thermal transports," J. Am. Chem. Soc. **133**(20), 7837–7846 (2011).
[68]X. Meng, Z. Liu, B. Cui, D. Qin, H. Geng, W. Cai, L. Fu, J. He, Z. Ren, and J. Sui, "Grain boundary engineering for achieving high thermoelectric performance in n-type skutterudites," Adv. Energy Mater. **7**(13), 1602582 (2017).
[69]W.-S. Liu, B.-P. Zhang, J.-F. Li, and L.-D. Zhao, "Effects of Sb compensation on microstructure, thermoelectric properties and point defect of $CoSb_3$ compound," J. Phys. D: Appl. Phys. **40**(21), 6784–6790 (2007).
[70]K. Suekuni, K. Tsuruta, T. Ariga, and M. Koyano, "Thermoelectric properties of mineral tetrahedrites $Cu_{10}Tr_2Sb_4S_{13}$ with low thermal conductivity," Appl. Phys. Express **5**(5), 051201 (2012).
[71]X. Lu, D. T. Morelli, Y. Xia, F. Zhou, V. Ozolins, H. Chi, X. Zhou, and C. Uher, "High performance thermoelectricity in earth-abundant compounds based on natural mineral tetrahedrites," Adv. Energy Mater. **3**(3), 342–348 (2013).
[72]K. Suekuni, K. Tsuruta, M. Kunii, H. Nishiate, E. Nishibori, S. Maki, M. Ohta, A. Yamamoto, and M. Koyano, "High-performance thermoelectric mineral $Cu_{12-x}Ni_xSb_4S_{13}$ tetrahedrite," J. Appl. Phys. **113**(4), 043712 (2013).
[73]B. Yu, M. Zebarjadi, H. Wang, K. Lukas, H. Wang, D. Wang, C. Opeil, M. Dresselhaus, G. Chen, and Z. Ren, "Enhancement of thermoelectric properties by modulation-doping in silicon germanium alloy nanocomposites," Nano Lett. **12**(4), 2077–2082 (2012).
[74]R. Basu and A. Singh, "High temperature Si–Ge alloy towards thermoelectric applications: A comprehensive review," Mater. Today Phys. **21**, 100468 (2021).
[75]D. Cheikh, B. E. Hogan, T. Vo, P. Von Allmen, K. Lee, D. M. Smiadak, A. Zevalkink, B. S. Dunn, J.-P. Fleurial, and S. K. Bux, "Praseodymium telluride: A high-temperature, high-ZT thermoelectric material," Joule **2**(4), 698–709 (2018).
[76]A. F. May, E. Flage-Larsen, and G. J. Snyder, "Electron and phonon scattering in the high-temperature thermoelectric $La_3Te_{4-z}Mz(M{=}Sb,Bi)$," Phys. Rev. B **81**(12), 125205 (2010).
[77]E. S. Toberer, C. A. Cox, S. R. Brown, T. Ikeda, A. F. May, S. M. Kauzlarich, and G. J. Snyder, "Traversing the metal-insulator transition in a Zintl phase: Rational enhancement of thermoelectric efficiency in $Yb_{14}Mn_{1-x}Al_xSb_{11}$," Adv. Funct. Mater. **18**(18), 2795–2800 (2008).
[78]S. R. Brown, S. M. Kauzlarich, F. Gascoin, and G. J. Snyder, "$Yb_{14}MnSb_{11}$: New high efficiency thermoelectric material for power generation," Chem. Mater. **18**(7), 1873–1877 (2006).
[79]C. Fu, S. Bai, Y. Liu, Y. Tang, L. Chen, X. Zhao, and T. Zhu, "Realizing high figure of merit in heavy-band p-type half-Heusler thermoelectric materials," Nat. Commun. **6**(1), 8144 (2015).
[80]X. Yan, W. Liu, S. Chen, H. Wang, Q. Zhang, G. Chen, and Z. Ren, "Thermoelectric property study of nanostructured p-type half-Heuslers (Hf, Zr, Ti)$CoSb_{0.8}Sn_{0.2}$," Adv. Energy Mater. **3**(9), 1195–1200 (2013).

[81]X. Yan, W. Liu, H. Wang, S. Chen, J. Shiomi, K. Esfarjani, H. Wang, D. Wang, G. Chen, and Z. Ren, "Stronger phonon scattering by larger differences in atomic mass and size in p-type half-Heuslers $Hf_{1-x}TixCoSb_{0.8}Sn_{0.2}$," Energy Environ. Sci. **5**(6), 7543–7548 (2012).
[82]J. Mao, Z. Liu, and Z. Ren, "Size effect in thermoelectric materials," npj Quant. Mater. **1**(1), 1–9 (2016).
[83]X. Zhou, Y. Yan, X. Lu, H. Zhu, X. Han, G. Chen, and Z. Ren, "Routes for high-performance thermoelectric materials," Mater. Today **21**(9), 974–988 (2018).
[84]L. Yang, Z.-G. Chen, M. S. Dargusch, and J. Zou, "High performance thermoelectric materials: Progress and their applications," Adv. Energy Mater. **8**(6), 1701797 (2018).
[85]M. K. Jana and K. Biswas, "Crystalline solids with intrinsically low lattice thermal conductivity for thermoelectric energy conversion," ACS Energy Lett. **3**(6), 1315–1324 (2018).
[86]Y. Liu, W. Wang, J. Yang, and S. Li, "Recent advances of layered thermoelectric materials," Adv. Sustainable Syst. **2**(8–9), 1800046 (2018).
[87]H. A. Eivari, Z. Sohbatzadeh, P. Mele, and M. H. N. Assadi, "Low thermal conductivity: Fundamentals and theoretical aspects in thermoelectric applications," Mater. Today Energy **21**, 100744 (2021).
[88]Q. Yan and M. G. Kanatzidis, "High-performance thermoelectrics and challenges for practical devices," Nat. Mater. **21**(5), 503–513 (2022).
[89]J. Mao, G. Chen, and Z. Ren, "Thermoelectric cooling materials," Nat. Mater. **20**(4), 454–461 (2021).
[90]X.-L. Shi, J. Zou, and Z.-G. Chen, "Advanced thermoelectric design: From materials and structures to devices," Chem. Rev. **120**(15), 7399–7515 (2020).
[91]I. Petsagkourakis, K. Tybrandt, X. Crispin, I. Ohkubo, N. Satoh, and T. Mori, "Thermoelectric materials and applications for energy harvesting power generation," Sci. Technol. Adv. Mater. **19**(1), 836–862 (2018).
[92]S. Hao, V. P. Dravid, M. G. Kanatzidis, and C. Wolverton, "Computational strategies for design and discovery of nanostructured thermoelectrics," npj Comput. Mater. **5**(1), 1–10 (2019).
[93]H. Zhu, C. Xiao, and Y. Xie, "Design of highly efficient thermoelectric materials: Tailoring reciprocal-space properties by real-space modification," Adv. Mater. **30**(48), e1802000 (2018).
[94]P. Gorai, V. Stevanović, and E. S. Toberer, "Computationally guided discovery of thermoelectric materials," Nat. Rev. Mater. **2**(9), 17053 (2017).
[95]Y. Zhou and L.-D. Zhao, "Promising thermoelectric bulk materials with 2D structures," Adv. Mater. **29**(45), 1702676 (2017).
[96]W. G. Zeier, A. Zevalkink, Z. M. Gibbs, G. Hautier, M. G. Kanatzidis, and G. J. Snyder, "Thinking like a chemist: Intuition in thermoelectric materials," Angew. Chem. Int. Ed. **55**(24), 6826–6841 (2016).
[97]Y. Qin, B. Qin, D. Wang, C. Chang, and L.-D. Zhao, "Solid-state cooling: Thermoelectrics," Energy Environ. Sci. **15**(11), 4527–4541 (2022).
[98]Z. Liu, "Challenges for thermoelectric power generation: From a material perspective," MatLab **1**, 220003 (2022).
[99]J. Wei, L. Yang, Z. Ma, P. Song, M. Zhang, J. Ma, F. Yang, and X. Wang, "Review of current high-ZT thermoelectric materials," J. Mater. Sci. **55**(27), 12642–12704 (2020).
[100]N. Jia, J. Cao, X. Y. Tan, J. Dong, H. Liu, C. K. I. Tan, J. Xu, Q. Yan, X. J. Loh, and A. Suwardi, "Thermoelectric materials and transport physics," Mater. Today Phys. **21**, 100519 (2021).
[101]T. Ghosh, M. Dutta, D. Sarkar, and K. Biswas, "Insights into low thermal conductivity in inorganic materials for thermoelectrics," J. Am. Chem. Soc. **144**(23), 10099–10118 (2022).
[102]C. Hu, K. Xia, C. Fu, X. Zhao, and T. Zhu, "Carrier grain boundary scattering in thermoelectric materials," Energy Environ. Sci. **15**(4), 1406–1422 (2022).
[103]Y. Zheng, T. J. Slade, L. Hu, X. Y. Tan, Y. Luo, Z.-Z. Luo, J. Xu, Q. Yan, and M. G. Kanatzidis, "Defect engineering in thermoelectric materials: What have we learned?," Chem. Soc. Rev. **50**(16), 9022–9054 (2021).
[104]X. Jia, S. Li, Z. Zhang, Y. Deng, X. Li, Y. Cao, Y. Yan, J. Mao, J. Yang, Q. Zhang, and X. Liu, "Using materials quality factor $B_{\Delta E}$ for design of thermoelectric materials with multiple bands," Mater. Today Phys. **18**, 100371 (2021).
[105]B. Qin, D. Wang, and L.-D. Zhao, "Slowing down the heat in thermoelectrics," InfoMat **3**(7), 755–789 (2021).
[106]C. Zhao, Z. Li, T. Fan, C. Xiao, and Y. Xie, "Defects engineering with multiple dimensions in thermoelectric materials," Research **2020**, 9652749.
[107]P.-C. Wei, C.-N. Liao, H.-J. Wu, D. Yang, J. He, G. V. Biesold-McGee, S. Liang, W.-T. Yen, X. Tang, J.-W. Yeh, Z. Lin, and J.-H. He, "Thermodynamic routes to ultralow thermal conductivity and high thermoelectric performance," Adv. Mater. **32**(12), e1906457 (2020).
[108]J. Xin, Y. Tang, Y. Liu, X. Zhao, H. Pan, and T. Zhu, "Valleytronics in thermoelectric materials," npj Quant. Mater. **3**(1), 1–10 (2018).
[109]Z. Chen, X. Zhang, and Y. Pei, "Manipulation of phonon transport in thermoelectrics," Adv. Mater. **30**(17), e1705617 (2018).
[110]T. Mori, "Novel principles and nanostructuring methods for enhanced thermoelectrics," Small **13**(45), 1702013 (2017).
[111]Y. Pei, H. Wang, and G. J. Snyder, "Band engineering of thermoelectric materials," Adv. Mater. **24**(46), 6125–6135 (2012).
[112]T. Hori and J. Shiomi, "Tuning phonon transport spectrum for better thermoelectric materials," Sci. Technol. Adv. Mater. **20**(1), 10–25 (2019).
[113]C. Xie, X. Tang, and G. Tan, "Off-centering thermoelectrics," Next Mater. **1**(4), 100048 (2023).
[114]L. Xu, Z. Yin, Y. Xiao, and L.-D. Zhao, "Interstitials in thermoelectrics," Adv. Mater. **36**(36), e2406009 (2024).
[115]Q. Xiong, G. Han, G. Wang, X. Lu, and X. Zhou, "The doping strategies for modulation of transport properties in thermoelectric materials," Adv. Funct. Mater. **34**, 2411304 (2024).
[116]R. Moshwan, X.-L. Shi, W.-D. Liu, J. Liu, and Z.-G. Chen, "Entropy engineering: An innovative strategy for designing high-performance thermoelectric materials and devices," Nano Today **58**, 102475 (2024).
[117]H. Kageyama, K. Hayashi, K. Maeda, J. P. Attfield, Z. Hiroi, J. M. Rondinelli, and K. R. Poeppelmeier, "Expanding Frontiers in materials chemistry and physics with multiple anions," Nat. Commun. **9**(1), 772 (2018).
[118]H. Kageyama, T. Yajima, Y. Tsujimoto, T. Yamamoto, C. Tassel, and Y. Kobayashi, "Exploring structures and properties through anion chemistry," Bull. Chem. Soc. Jpn. **92**(8), 1349–1357 (2019).
[119]J. K. Harada, N. Charles, K. R. Poeppelmeier, and J. M. Rondinelli, "Heteroanionic materials by design: Progress toward targeted properties," Adv. Mater. **31**(19), 1805295 (2019).
[120]K. Maeda, F. Takeiri, G. Kobayashi, S. Matsuishi, H. Ogino, S. Ida, T. Mori, Y. Uchimoto, S. Tanabe, T. Hasegawa, N. Imanaka, and H. Kageyama, "Recent progress on mixed-anion materials for energy applications," Bull. Chem. Soc. Jpn. **95**(1), 26–37 (2022).
[121]L. T. Menezes, E. Gage, A. Assoud, M. Liang, P. S. Halasyamani, and H. Kleinke, "$Sr_6Ge_3OSe_{11}$: A rationally designed noncentrosymmetric oxyselenide with polar [$GeOSe_3$] building blocks," Chem. Mater. **35**(7), 3033–3040 (2023).
[122]N. Sato, N. Kuroda, S. Nakamura, Y. Katsura, I. Kanazawa, K. Kimura, and T. Mori, "Bonding heterogeneity in mixed-anion compounds realizes ultralow lattice thermal conductivity," J. Mater. Chem. A **9**(39), 22660–22669 (2021).
[123]H. Wang, J. Wang, X. Cao, and G. J. Snyder, "Thermoelectric alloys between PbSe and PbS with effective thermal conductivity reduction and high figure of merit," J. Mater. Chem. A **2**(9), 3169–3174 (2014).
[124]P. G. Klemens, "Thermal resistance due to point defects at high temperatures," Phys. Rev. **119**, 507–509 (1960).
[125]J. Feng, J. Li, and R. Liu, "Low-temperature thermoelectric materials and applications," Nano Energy **126**, 109651 (2024).
[126]D. Sarkar, A. Bhui, I. Maria, M. Dutta, and K. Biswas, "Hidden structures: A driving factor to achieve low thermal conductivity and high thermoelectric performance," Chem. Soc. Rev. **53**(12), 6100–6149 (2024).
[127]T. Hendricks, T. Caillat, and T. Mori, "Keynote review of latest advances in thermoelectric generation materials, devices, and technologies 2022," Energies **15**(19), 7307 (2022).
[128]H.-L. Zhuang, B. Cai, Y. Pan, B. Su, Y. Jiang, J. Pei, F. Liu, H. Hu, J. Yu, J.-W. Li, Z. Wang, Z. Han, H. Li, C. Wang, and J.-F. Li, "Strong and efficient bismuth telluride-based thermoelectrics for Peltier microcoolers," Natl. Sci. Rev. **11**(10), nwae329 (2024).
[129]H. J. Goldsmid, "Heat conduction in bismuth telluride," Proc. Phys. Soc. **72**(1), 17–26 (1958).
[130]H. Goldsmid, "Recent studies of bismuth telluride and its alloys," J. Appl. Phys. **32**, 2198–2202 (1961).
[131]H. J. Goldsmid, "Bismuth telluride and its alloys as materials for thermoelectric generation," Materials **7**(4), 2577–2592 (2014).

[132]I. T. Witting, T. C. Chasapis, F. Ricci, M. Peters, N. A. Heinz, G. Hautier, and G. J. Snyder, "The thermoelectric properties of bismuth telluride," Adv. Elect. Mater. **5**(6), 1800904 (2019).

[133]Y. Lu, Y. Zhou, W. Wang, M. Hu, X. Huang, D. Mao, S. Huang, L. Xie, P. Lin, B. Jiang, B. Zhu, J. Feng, J. Shi, Q. Lou, Y. Huang, J. Yang, J. Li, G. Li, and J. He, "Staggered-layer-boosted flexible Bi_2Te_3 films with high thermoelectric performance," Nat. Nanotechnol. **18**(11), 1281–1288 (2023).

[134]T. Zhu, L. Hu, X. Zhao, and J. He, "New insights into intrinsic point defects in V_2VI_3 thermoelectric materials," Adv. Sci. **3**(7), 1600004 (2016).

[135]C. B. Satterthwaite and R. W. Ure, "Electrical and thermal properties of Bi_2Te_3," Phys. Rev. **108**(5), 1164–1170 (1957).

[136]D. O. Scanlon, P. D. C. King, R. P. Singh, A. de la Torre, S. M. Walker, G. Balakrishnan, F. Baumberger, and C. R. A. Catlow, "Controlling bulk conductivity in topological insulators: Key role of anti-site defects," Adv. Mater. **24**(16), 2154–2158 (2012).

[137]L.-L. Wang, M. Huang, S. Thimmaiah, A. Alam, S. L. Bud'ko, A. Kaminski, T. A. Lograsso, P. Canfield, and D. D. Johnson, "Native defects in tetradymite $Bi_2(Te_xSe_{3-x})$ topological insulators," Phys. Rev. B Condens. Matter Mater. Phys. **87**(12), 125303 (2013).

[138]N. Fuschillo, J. N. Bierly, and F. J. Donahoe, "Transport properties of the pseudo-binary alloy system $Bi_2Te_3-ySe_y$," J. Phys. Chem. Solids **8**, 430–433 (1959).

[139]T. C. Chasapis, D. Koumoulis, B. Leung, N. P. Calta, S.-H. Lo, V. P. Dravid, L.-S. Bouchard, and M. G. Kanatzidis, "Two-band model interpretation of the p- to n-transition in ternary tetradymite topological insulators," APL Mater. **3**(8), 083601 (2015).

[140]U. Birkholz, "Untersuchung der intermetallischen verbindung Bi_2Te_3 sowie der festen Lösungen $Bi_{2-x}Sb_xTe_3$ und $Bi_2Te_{3-x}Se_x$ hinsichtlich ihrer Eignung als Material für Halbleiter-Thermoelemente," Z. Naturforsch. A **13**(9), 780–792 (1958).

[141]J. Horák, P. Lošťák, L. Koudelka, and R. Novotný, "Inversion of conductivity type in $Bi_2Te_{3-x}S_x$ crystals," Solid State Commun. **55**(11), 1031–1034 (1985).

[142]P. Lostak, J. Horak, and L. Koudelka, "Some physical properties and point defects in $Bi_2Te_{3-x}S_x$ mixed crystal," Phys. Status Solidi. A **84**(2), K143–K147 (1984).

[143]J. Horák, Z. Star, and J. Votinsk, "Point defects in the mixed chalcogenides $Bi_2Te_{3-x}X_x$(X = S, Se)," Philos. Mag. B **69**(1), 31–38 (1994).

[144]I. T. Witting, F. Ricci, T. C. Chasapis, G. Hautier, and G. J. Snyder, "The thermoelectric properties of n-type bismuth Telluride: Bismuth selenide alloys Bi_2Te_{3-x} Se_x," Research **2020**, 4361703.

[145]F. D. Rosi, B. Abeles, and R. V. Jensen, "Materials for thermoelectric refrigeration," J. Phys. Chem. Solids **10**(2–3), 191–200 (1959).

[146]J. R. Drabble and C. H. L. Goodman, "Chemical bonding in bismuth telluride," J. Phys. Chem. Solids **5**(1–2), 142–144 (1958).

[147]L. Pauling, "The formula, structure, and chemical bonding of tetradymite, $Bi_{14}Te_{13}S_8$, and the phase $Bi_{14}Te_{15}S_6$," Am. Miner. **60**(11–12), 994–997 (1975).

[148]Z. M. Gibbs, F. Ricci, G. Li, H. Zhu, K. Persson, G. Ceder, G. Hautier, A. Jain, and G. J. Snyder, "Effective mass and Fermi surface complexity factor from ab initio band structure calculations," npj Comput. Mater. **3**(1), 1–7 (2017).

[149]W. Liu, K. C. Lukas, K. McEnaney, S. Lee, Q. Zhang, C. P. Opeil, G. Chen, and Z. Ren, "Studies on the Bi_2Te_3–Bi_2Se_3–Bi_2S_3 system for mid-temperature thermoelectric energy conversion," Energy Environ. Sci. **6**(2), 552–560 (2013).

[150]B. Jabar, F. Li, Z. Zheng, A. Mansoor, Y. Zhu, C. Liang, D. Ao, Y. Chen, G. Liang, P. Fan, and W. Liu, "Homo-composition and hetero-structure nanocomposite Pnma Bi_2SeS_2–Pnnm Bi_2SeS_2 with high thermoelectric performance," Nat. Commun. **12**(1), 7192 (2021).

[151]C. H. Champness, W. B. Muir, and P. T. Chiang, "Thermoelectric properties of n-TYPE Bi_2Te_3–Bi_2Se_3 alloys," Can. J. Phys. **45**(11), 3611–3626 (1967).

[152]R. S. Allgaier, "Valence bands in lead telluride," J. Appl. Phys. **32**(10), 2185–2189 (1961).

[153]S. V. Airapetyants, M. N. Vinogradova, IN. Dubrovskaya, N. V. Kolomoets, and I. M. Rudnik, "Structure of the valence band of heavily doped lead telluride," Soviet Phys. Solid State **8**(5), 1069–1072 (1966).

[154]D. Khokhlov, *Lead Chalcogenides: Physics & Applications* (Routledge, Boca Raton, 2021).

[155]J. He, L.-D. Zhao, J.-C. Zheng, J. W. Doak, H. Wu, H.-Q. Wang, Y. Lee, C. Wolverton, M. G. Kanatzidis, and V. P. Dravid, "Role of sodium doping in lead chalcogenide thermoelectrics," J. Am. Chem. Soc. **135**(12), 4624–4627 (2013).

[156]Y. Noda, M. Orihashi, and I. A. Nishida, "Thermoelectric properties of p-type lead Telluride doped with silver or potassium," Mater. Trans., JIM **39**(5), 602–605 (1998).

[157]J. Androulakis, I. Todorov, D. Chung, S. Ballikaya, G. Wang, C. Uher, and M. Kanatzidis, "Thermoelectric enhancement in PbTe with K or Na codoping from tuning the interaction of the light- and heavy-hole valence bands," Phys. Rev. B **82**, 115209 (2010).

[158]S. Ahmad, S. D. Mahanti, K. Hoang, and M. G. Kanatzidis, "Ab initio studies of the electronic structure of defects in PbTe," Phys. Rev. B **74**(15), 155205 (2006).

[159]Q. Zhang, F. Cao, W. Liu, K. Lukas, B. Yu, S. Chen, C. Opeil, D. Broido, G. Chen, and Z. Ren, "Heavy doping and band engineering by potassium to improve the thermoelectric figure of merit in p-type PbTe, PbSe, and PbTe1-ySey," J. Am. Chem. Soc. **134**(24), 10031–10038 (2012).

[160]S. A. Yamini, H. Wang, D. Ginting, D. R. G. Mitchell, S. X. Dou, and G. J. Snyder, "Thermoelectric performance of n-type $(PbTe)_{0.75}(PbS)_{0.15}(PbSe)_{0.1}$ composites," ACS Appl. Mater. Interfaces **6**(14), 11476–11483 (2014).

[161]S. A. Yamini, H. Wang, Z. M. Gibbs, Y. Pei, S. X. Dou, and G. J. Snyder, "Chemical composition tuning in quaternary p-type Pb-chalcogenides–a promising strategy for enhanced thermoelectric performance," Phys. Chem. Chem. Phys. **16**(5), 1835–1840 (2014).

[162]S. Aminorroaya Yamini, H. Wang, Z. M. Gibbs, Y. Pei, D. R. G. Mitchell, S. X. Dou, and G. J. Snyder, "Thermoelectric performance of tellurium-reduced quaternary p-type lead–chalcogenide composites," Acta Mater. **80**, 365–372 (2014).

[163]S. A. Yamini, D. R. G. Mitchell, Z. M. Gibbs, R. Santos, V. Patterson, S. Li, Y. Z. Pei, S. X. Dou, and G. Jeffrey Snyder, "Heterogeneous distribution of sodium for high thermoelectric performance of p-type multiphase lead-chalcogenides," Adv. Energy Mater. **5**(21), 1501047 (2015).

[164]B. Qin, X. Hu, Y. Zhang, H. Wu, S. J. Pennycook, and L.-D. Zhao, "Comprehensive investigation on the thermoelectric properties of p-type PbTe-PbSe-PbS alloys," Adv. Elect. Mater. **5**(12), 1900609 (2019).

[165]Y. Pei, Z. M. Gibbs, A. Gloskovskii, B. Balke, W. G. Zeier, and G. J. Snyder, "Optimum carrier concentration in n-type PbTe thermoelectrics," Adv. Energy Mater. **4**(13), 1400486 (2014).

[166]D. M. Rowe, *Thermoelectrics Handbook: Macro to Nano* (CRC Press, 2018).

[167]A. D. LaLonde, Y. Pei, and G. J. Snyder, "Reevaluation of $PbTe_{1-x}$ I_x as high performance n-type thermoelectric material," Energy Environ. Sci. **4**(6), 2090–2096 (2011).

[168]H. Wang, X. Cao, Y. Takagiwa, and G. J. Snyder, "Higher mobility in bulk semiconductors by separating the dopants from the charge-conducting band—A case study of thermoelectric PbSe," Mater. Horiz. **2**(3), 323–329 (2015).

[169]B. Jiang, Y. Yu, J. Cui, X. Liu, L. Xie, J. Liao, Q. Zhang, Y. Huang, S. Ning, B. Jia, B. Zhu, S. Bai, L. Chen, S. J. Pennycook, and J. He, "High-entropy-stabilized chalcogenides with high thermoelectric performance," Science **371**(6531), 830–834 (2021).

[170]A. Yamashita, Y. Goto, A. Miura, C. Moriyoshi, Y. Kuroiwa, and Y. Mizuguchi, "n-Type thermoelectric metal chalcogenide (Ag,Pb,Bi)(S,Se,Te) designed by multi-site-type high-entropy alloying," Mater. Res. Lett. **9**(9), 366–372 (2021).

[171]B. Jiang, Y. Yu, H. Chen, J. Cui, X. Liu, L. Xie, and J. He, "Entropy engineering promotes thermoelectric performance in p-type chalcogenides," Nat. Commun. **12**(1), 3234 (2021).

[172]T. Chattopadhyay, J. X. Boucherle, and H. G. vonSchnering, "Neutron diffraction study on the structural phase transition in GeTe," J. Phys. C: Solid State Phys. **20**(10), 1431–1440 (1987).

[173]J. Li, X. Zhang, S. Lin, Z. Chen, and Y. Pei, "Realizing the high thermoelectric performance of GeTe by Sb-doping and Se-alloying," Chem. Mater. **29**(2), 605–611 (2017).

[174]M. Samanta and K. Biswas, "Low thermal conductivity and high thermoelectric performance in $(GeTe)_{1-2x}(GeSe)_x(GeS)_x$: Competition between solid solution and phase separation," J. Am. Chem. Soc. **139**(27), 9382–9391 (2017).

[175]M. Li, S.-D. Xu, M. Hong, W.-Y. Lyu, Y. Wang, M. Dargusch, J. Zou, H.-M. Cheng, and Z.-G. Chen, "Roles of anion sites in high-performance GeTe thermoelectrics," Adv. Funct. Mater. **32**(48), 2208579 (2022).

[176]E. Quarez, K.-F. Hsu, R. Pcionek, N. Frangis, E. K. Polychroniadis, and M. G. Kanatzidis, "Nanostructuring, compositional fluctuations, and atomic ordering in the thermoelectric materials $AgPb_mSbTe_{2+m}$. The myth of solid solutions," J. Am. Chem. Soc. **127**(25), 9177–9190 (2005).

[177]S. V. Barabash, V. Ozolins, and C. Wolverton, "First-principles theory of competing order types, phase separation, and phonon spectra in thermoelectric $AgPbmSbTe_{m+2}$ alloys," Phys. Rev. Lett. **101**(15), 155704 (2008).

[178]R. W. Armstrong, J. W. Faust, Jr., and W. A. Tiller, "A structural study of the compound $AgSbTe_2$," J. Appl. Phys. **31**(11), 1954–1959 (1960).

[179]L. Li, B. Hu, Q. Liu, X.-L. Shi, and Z.-G. Chen, "High-performance $AgSbTe_2$ thermoelectrics: Advances, challenges, and perspectives," Adv. Mater. **36**(45), 2409275 (2024).

[180]S. Roychowdhury, T. Ghosh, R. Arora, M. Samanta, L. Xie, N. K. Singh, A. Soni, J. He, U. V. Waghmare, and K. Biswas, "Enhanced atomic ordering leads to high thermoelectric performance in $AgSbTe_2$," Science **371**(6530), 722–727 (2021).

[181]T. Ghosh, S. Roychowdhury, M. Dutta, and K. Biswas, "High-performance thermoelectric energy conversion: A tale of atomic ordering in $AgSbTe_2$," ACS Energy Lett. **6**(8), 2825–2837 (2021).

[182]Y. Zhang, Z. Li, S. Singh, A. Nozariasbmarz, W. Li, A. Genç, Y. Xia, L. Zheng, S. H. Lee, S. K. Karan, G. K. Goyal, N. Liu, S. M. Mohan, Z. Mao, A. Cabot, C. Wolverton, B. Poudel, and S. Priya, "Defect-engineering-stabilized $AgSbTe_2$ with high thermoelectric performance," Adv. Mater. **35**(11), 2208994 (2022).

[183]A. Seshita, A. Yamashita, T. Fujita, T. Katase, A. Miura, Y. Nakahira, C. Moriyoshi, Y. Kuroiwa, and Y. Mizuguchi, "Stabilization and high thermoelectric performance of high-entropy-type cubic $AgBi(S, Se, Te)_2$," J. Alloys Compd. **1004**, 175679 (2024).

[184]A. Seshita, A. Yamashita, T. Katase, and Y. Mizuguchi, "High entropy effect on thermoelectric properties of the nonequilibrium cubic phase of $AgBiSe_{2-2x}S_xTe_x$ with $x = 0$–0.6," Dalton Trans. **53**(35), 14830–14838 (2024).

[185]C. Chang, M. Wu, D. He, Y. Pei, C.-F. Wu, X. Wu, H. Yu, F. Zhu, K. Wang, Y. Chen, L. Huang, J.-F. Li, J. He, and L.-D. Zhao, "3D charge and 2D phonon transports leading to high out-of-plane ZT in n-type SnSe crystals," Science **360**(6390), 778–783 (2018).

[186]C. Zhou, Y. K. Lee, Y. Yu, S. Byun, Z.-Z. Luo, H. Lee, B. Ge, Y.-L. Lee, X. Chen, J. Y. Lee, O. Cojocaru-Mirédin, H. Chang, J. Im, S.-P. Cho, M. Wuttig, V. P. Dravid, M. G. Kanatzidis, and I. Chung, "Polycrystalline SnSe with a thermoelectric figure of merit greater than the single crystal," Nat. Mater. **20**(10), 1378–1384 (2021).

[187]Y. Huang, C. Wang, X. Chen, D. Zhou, J. Du, S. Wang, and L. Ning, "First-principles study on intrinsic defects of SnSe," RSC Adv. **7**(44), 27612–27618 (2017).

[188]J. Vidal, S. Lany, M. d'Avezac, A. Zunger, A. Zakutayev, J. Francis, and J. Tate, "Band-structure, optical properties, and defect physics of the photovoltaic semiconductor SnS," Appl. Phys. Lett. **100**(3), 032104 (2012).

[189]C.-L. Chen, H. Wang, Y.-Y. Chen, T. Day, and G. J. Snyder, "Thermoelectric properties of p-type polycrystalline SnSe doped with Ag," J. Mater. Chem. A **2**(29), 11171–11176 (2014).

[190]E. K. Chere, Q. Zhang, K. Dahal, F. Cao, J. Mao, and Z. Ren, "Studies on thermoelectric figure of merit of Na-doped p-type polycrystalline SnSe," J. Mater. Chem. A **4**(5), 1848–1854 (2016).

[191]H.-Q. Leng, M. Zhou, J. Zhao, Y.-M. Han, and L.-F. Li, "The thermoelectric performance of anisotropic SnSe doped with Na," RSC Adv. **6**(11), 9112–9116 (2016).

[192]T.-R. Wei, G. Tan, X. Zhang, C.-F. Wu, J.-F. Li, V. P. Dravid, G. J. Snyder, and M. G. Kanatzidis, "Distinct impact of alkali-ion doping on electrical transport properties of thermoelectric p-type polycrystalline SnSe," J. Am. Chem. Soc. **138**(28), 8875–8882 (2016).

[193]C. Haas and M. M. G. Corbey, "Measurement and analysis of the infrared reflection spectrum of semiconducting SnS," J. Phys. Chem. Solids **20**(3–4), 197–203 (1961).

[194]B. Zhou, S. Li, W. Li, J. Li, X. Zhang, S. Lin, Z. Chen, and Y. Pei, "Thermoelectric properties of SnS with Na-doping," ACS Appl. Mater. Interfaces **9**(39), 34033–34041 (2017).

[195]Y. Niu, Y. Chen, J. Jiang, Y. Pan, C. Yang, and C. Wang, "Enhanced thermoelectric performance in Li doped SnS via carrier concentration optimization," IOP Conf. Ser: Mater. Sci. Eng. **738**(1), 012016 (2020).

[196]Q. Tan, L.-D. Zhao, J.-F. Li, C.-F. Wu, T.-R. Wei, Z.-B. Xing, and M. G. Kanatzidis, "Thermoelectrics with earth abundant elements: Low thermal conductivity and high thermopower in doped SnS," J. Mater. Chem. A **2**(41), 17302–17306 (2014).

[197]P. Čermák, J. Hejtmánek, T. Plecháček, J. Navrátil, J. Kašparová, V. Holý, Z. Zmrhalová, M. Jarošová, L. Beneš, and Č. Drašar, "Thermoelectric properties and stability of Tl-doped SnS," J. Alloys Compd. **811**, 151902 (2019).

[198]X. He, H. Zhang, T. Nose, T. Katase, T. Tadano, K. Ide, S. Ueda, H. Hiramatsu, H. Hosono, and T. Kamiya, "Degenerated hole doping and ultralow lattice thermal conductivity in polycrystalline SnSe by nonequilibrium isovalent Te substitution," Adv. Sci. **9**(13), 2105958 (2022).

[199]Y. Nishimura, X. He, T. Katase, T. Tadano, K. Ide, S. Kitani, K. Hanzawa, S. Ueda, H. Hiramatsu, H. Kawaji, H. Hosono, and T. Kamiya, "Electronic and lattice thermal conductivity switching by 3D−2D crystal structure transition in nonequilibrium $(Pb_{1-x}Sn_x)Se$," Adv. Elect. Mater. **8**(9), 2200024 (2022).

[200]Z. Hu, M. Hiramatsu, X. He, T. Katase, T. Tadano, K. Ide, H. Hiramatsu, H. Hosono, and T. Kamiya, "Reversible thermal conductivity modulation of non-equilibrium $(Sn_{1-x}Pb_x)S$ by 2D–3D structural phase transition above room temperature," ACS Appl. Energy Mater. **6**(6), 3504–3513 (2023).

[201]X. He, J. Chen, T. Katase, M. Minohara, K. Ide, H. Hiramatsu, H. Kumigashira, H. Hosono, and T. Kamiya, "High-mobility metastable rock-salt type (Sn,Ca)Se thin film stabilized by direct epitaxial growth on a YSZ (111) single-crystal substrate," ACS Appl. Mater. Interfaces **14**(16), 18682–18689 (2022).

[202]W. He, D. Wang, H. Wu, Y. Xiao, Y. Zhang, D. He, Y. Feng, Y.-J. Hao, J.-F. Dong, R. Chetty, L. Hao, D. Chen, J. Qin, Q. Yang, X. Li, J.-M. Song, Y. Zhu, W. Xu, C. Niu, X. Li, G. Wang, C. Liu, M. Ohta, S. J. Pennycook, J. He, J.-F. Li, and L.-D. Zhao, "High thermoelectric performance in low-cost SnS0.91Se0.09 crystals," Science **365**(6460), 1418–1424 (2019).

[203]Y. He, T. Day, T. Zhang, H. Liu, X. Shi, L. Chen, and G. J. Snyder, "High thermoelectric performance in non-toxic earth-abundant copper sulfide," Adv. Mater. **26**(23), 3974–3978 (2014).

[204]L.-L. Zhao, X.-L. Wang, J.-Y. Wang, Z.-X. Cheng, S.-X. Dou, J. Wang, and L.-Q. Liu, "Superior intrinsic thermoelectric performance with zT of 1.8 in single-crystal and melt-quenched highly dense $Cu_{2-x}Se$ bulks," Sci. Rep. **5**(1), 7671 (2015).

[205]L. Zhao, X. Wang, F. Fei, J. Wang, Z. Cheng, S. Dou, J.-L. Wang, and J. Snyder, "High thermoelectric and mechanical performance in highly dense $Cu_{2-x}S$ bulks prepared by a melt-solidification technique," J. Mater. Chem. A **3**, 9432–9437 (2015).

[206]L. Zhao, X. Wang, F. Yun, J. Wang, Z. Cheng, S. Dou, J.-L. Wang, and G. J. Snyder, "The effects of Te_2− and I− substitutions on the electronic structures, thermoelectric performance, and hardness in melt-quenched highly dense $Cu_{2-x}Se$," Adv. Elect. Mater. **1**, 1400015–1400015 (2015).

[207]K. Zhao, K. Liu, Z. Yue, Y. Wang, Q. Song, J. Li, M. Guan, Q. Xu, P. Qiu, H. Zhu, L. Chen, and X. Shi, "Are Cu_2 Te-based compounds excellent thermoelectric materials?," Adv. Mater. **31**(49), e1903480 (2019).

[208]Z. Zhang, K. Zhao, T.-R. Wei, P. Qiu, L. Chen, and X. Shi, "Cu_2Se-based liquid-like thermoelectric materials: Looking back and stepping forward," Energy Environ. Sci. **13**(10), 3307–3329 (2020).

[209]K. Zhao, P. Qiu, X. Shi, and L. Chen, "Recent advances in liquid-like thermoelectric materials," Adv. Funct. Mater. **30**(8), 1903867 (2020).

[210]K. Zhao, A. B. Blichfeld, H. Chen, Q. Song, T. Zhang, C. Zhu, D. Ren, R. Hanus, P. Qiu, B. B. Iversen, F. Xu, G. J. Snyder, X. Shi, and L. Chen, "Enhanced thermoelectric performance through tuning bonding energy in Cu_2S_{e1-xSx} liquid-like materials," Chem. Mater. **29**(15), 6367–6377 (2017).

[211]M. Zhou, K. Zhao, H. Wuliji, H. Su, J. Lei, T.-R. Wei, F. Xu, and X. Shi, "High thermoelectric performance near the Mott–Ioffe–Regel limit in $CuxS_{0.6}Te_{0.4}$ meta-phases," Mater. Today Phys. **42**, 101371 (2024).

[212]W.-D. Liu, L. Yang, and Z.-G. Chen, "Cu_2Se thermoelectrics: Property, methodology, and device," Nano Today **35**, 100938 (2020).

[213]W.-D. Liu, L. Yang, Z.-G. Chen, and J. Zou, "Promising and eco-friendly Cu_2 X-based thermoelectric materials: Progress and applications," Adv. Mater. **32**(8), 1905703 (2020).

[214]A. Basit, J. Xin, G. Murtaza, L. Wei, A. Hameed, W. Guoyu, and J. Y. Dai, "Recent advances, challenges, and perspective of copper-based liquid-like thermoelectric chalcogenides: A review," EcoMat **5**(9), e12391 (2023).

[215]K. Zhao, C. Zhu, M. Zhu, H. Chen, J. Lei, Q. Ren, T.-R. Wei, P. Qiu, F. Xu, L. Chen, J. He, and X. Shi, "Structural modularization of Cu_2 Te leading to high thermoelectric performance near the Mott-Ioffe-Regel limit," Adv. Mater. **34**(19), e2108573 (2022).
[216]F. Garmroudi, M. Parzer, A. Riss, A. V. Ruban, S. Khmelevskyi, M. Reticcioli, M. Knopf, H. Michor, A. Pustogow, T. Mori, and E. Bauer, "Anderson transition in stoichiometric Fe_2VAl: High thermoelectric performance from impurity bands," Nat. Commun. **13**(1), 3599 (2022).
[217]M. T. Agne, F. R. L. Lange, J. P. Male, K. S. Siegert, H. Volker, C. Poltorak, A. Poitz, T. Siegrist, S. Maier, G. J. Snyder, and M. Wuttig, "Disorder-induced Anderson-like localization for bidimensional thermoelectrics optimization," Matter **4**(9), 2970–2984 (2021).
[218]K. Zhao, C. Zhu, W. Qiu, S. Yang, H. Su, P. Qiu, Y. He, M. Guan, T.-R. Wei, J. Ma, J. Liu, G. Zheng, F. Xu, X. Shi, J. He, and L. Chen, "Novel meta-phase arising from large atomic size mismatch," Matter **5**(2), 605–615 (2022).
[219]I. Serhiienko, A. Novitskii, F. Garmroudi, E. Kolesnikov, E. Chernyshova, T. Sviridova, A. Bogach, A. Voronin, H. D. Nguyen, N. Kawamoto, E. Bauer, V. Khovaylo, and T. Mori, "Record-high thermoelectric performance in Al-doped ZnO via Anderson localization of band edge states," Adv. Sci. **11**(26), 2309291 (2024).
[220]T. Katase, X. He, T. Tadano, J. M. Tomczak, T. Onozato, K. Ide, B. Feng, T. Tohei, H. Hiramatsu, H. Ohta, Y. Ikuhara, H. Hosono, and T. Kamiya, "Breaking of thermopower-conductivity trade-off in $LaTiO_3$ film around Mott insulator to metal transition," Adv. Sci. (Weinh) **8**(23), e2102097 (2021).
[221]H. Hu, Y. Ju, J. Yu, Z. Wang, J. Pei, H.-C. Thong, J.-W. Li, B. Cai, F. Liu, Z. Han, B. Su, H.-L. Zhuang, Y. Jiang, H. Li, Q. Li, H. Zhao, B.-P. Zhang, J. Zhu, and J.-F. Li, "Highly stabilized and efficient thermoelectric copper selenide," Nat. Mater. **23**(4), 527–534 (2024).
[222]Y. Pei, N. A. Heinz, and G. J. Snyder, "Alloying to increase the band gap for improving thermoelectric properties of Ag_2Te," J. Mater. Chem. **21**(45), 18256 (2011).
[223]D. Yang, X. Su, F. Meng, S. Wang, Y. Yan, J. Yang, J. He, Q. Zhang, C. Uher, M. G. Kanatzidis, and X. Tang, "Facile room temperature solventless synthesis of high thermoelectric performance Ag2Se via a dissociative adsorption reaction," J. Mater. Chem. A **5**(44), 23243–23251 (2017).
[224]P. Jood, R. Chetty, and M. Ohta, "Structural stability enables high thermoelectric performance in room temperature Ag_2Se," J. Mater. Chem. A **8**(26), 13024–13037 (2020).
[225]T.-R. Wei, P. Qiu, K. Zhao, X. Shi, and L. Chen, "Ag_2Q-based (Q = S, Se, Te) silver chalcogenide thermoelectric materials," Adv. Mater. **35**(1), e2110236 (2023).
[226]X. Shi, H. Chen, F. Hao, R. Liu, T. Wang, P. Qiu, U. Burkhardt, Y. Grin, and L. Chen, "Room-temperature ductile inorganic semiconductor," Nat. Mater. **17**(5), 421–426 (2018).
[227]S. Yang, Z. Gao, P. Qiu, J. Liang, T.-R. Wei, T. Deng, J. Xiao, X. Shi, and L. Chen, "Ductile $Ag_{20}S_7Te_3$ with excellent shape-conformability and high thermoelectric performance," Adv. Mater. **33**(10), e2007681 (2021).
[228]J. Liang, T. Wang, P. Qiu, S. Yang, C. Ming, H. Chen, Q. Song, K. Zhao, T.-R. Wei, D. Ren, Y.-Y. Sun, X. Shi, J. He, and L. Chen, "Flexible thermoelectrics: From silver chalcogenides to full-inorganic devices," Energy Environ. Sci. **12**(10), 2983–2990 (2019).
[229]S. He, Y. Li, L. Liu, Y. Jiang, J. Feng, W. Zhu, J. Zhang, Z. Dong, Y. Deng, J. Luo, W. Zhang, and G. Chen, "Semiconductor glass with superior flexibility and high room temperature thermoelectric performance," Sci. Adv. **6**(15), eaaz8423 (2020).
[230]J. Liang, P. Qiu, Y. Zhu, H. Huang, Z. Gao, Z. Zhang, X. Shi, and L. Chen, "Crystalline structure-dependent mechanical and thermoelectric performance in $Ag_2Se_{1-x}S_x$ system," Research (Wash. D.C.) **2020**, 6591981.
[231]X. Liang and C. Chen, "Ductile inorganic amorphous/crystalline composite Ag_4TeS with phonon-glass electron-crystal transport behavior and excellent stability of high thermoelectric performance on plastic deformation," Acta Mater. **218**, 117231 (2021).
[232]J. Chen, Q. Sun, D. Bao, B.-Z. Tian, Z. Wang, J. Tang, D. Zhou, L. Yang, and Z.-G. Chen, "Simultaneously enhanced strength and plasticity of Ag2Se-based thermoelectric materials endowed by nano-twinned CuAgSe secondary phase," Acta Mater. **220**, 117335 (2021).
[233]T. Zhu, X. Su, Q. Zhang, and X. Tang, "Structural transformation and thermoelectric performance in $Ag_2Te_{1-x}Se_x$ solid solution," J. Alloys Compd. **871**, 159507 (2021).
[234]L. Peng, S. Yang, T.-R. Wei, P. Qiu, J. Yang, Z. Zhang, X. Shi, and L. Chen, "Phase-modulated mechanical and thermoelectric properties of $Ag_2S_{1-x}Te_x$ ductile semiconductors," J. Mater. **8**(3), 656–661 (2022).
[235]K. Yu, Y. Wu, H. He, C. Niu, M. Rong, D. Wu, S. Liu, and Y. Zhang, "Ultralow lattice thermal conductivity and enhanced thermoelectric performance in $Ag_{2-x}Se_{1/3}S_{1/3}Te_{1/3}$ via anion permutation and cation modulation," J. Alloys Compd. **885**, 161378 (2021).
[236]H. Chen, C. Shao, S. Huang, Z. Gao, H. Huang, Z. Pan, K. Zhao, P. Qiu, T.-R. Wei, and X. Shi, "High-entropy cubic pseudo-ternary Ag_2(S, Se, Te) materials with excellent ductility and thermoelectric performance," Adv. Energy Mater. **14**(10), 2303473 (2024).
[237]Q. Yang, S. Yang, P. Qiu, L. Peng, T.-R. Wei, Z. Zhang, X. Shi, and L. Chen, "Flexible thermoelectrics based on ductile semiconductors," Science **377**(6608), 854–858 (2022).
[238]K. Shen, Q. Yang, P. Qiu, Z. Zhou, S. Yang, T.-R. Wei, and X. Shi, "Ductile P-type AgCu(Se,S,Te) thermoelectric materials," Adv. Mater. **36**(35), e2407424 (2024).
[239]N.-H. Li, Q. Zhang, X.-L. Shi, J. Jiang, and Z.-G. Chen, "Silver copper chalcogenide thermoelectrics: Advance, controversy, and perspective," Adv. Mater. **36**, e2313146 (2024).
[240]W. Hume-Rothery and H. M. Powell, "On the theory of super-lattice structures in alloys," Z. Kristallogr. Cryst. Mater. **91**(1–6), 23–47 (1935).
[241]Z. Wang, Y. Huang, C. T. Liu, J. Li, and J. Wang, "Atomic packing and size effect on the Hume-Rothery rule," Intermetallics (Barking) **109**, 139–144 (2019).
[242]S. M. Kauzlarich, S. R. Brown, and G. J. Snyder, "Zintl phases for thermoelectric devices," Dalton Trans. **2007**(21), 2099–2107.
[243]E. S. Toberer, A. F. May, and G. J. Snyder, "Zintl chemistry for designing high efficiency thermoelectric materials," Chem. Mater. **22**(3), 624–634 (2010).
[244]J. Zhang, L. Song, S. H. Pedersen, H. Yin, L. T. Hung, and B. B. Iversen, "Discovery of high-performance low-cost n-type Mg_3Sb_2-based thermoelectric materials with multi-valley conduction bands," Nat. Commun. **8**, 13901 (2017).
[245]J. Shuai, J. Mao, S. Song, Q. Zhu, J. Sun, Y. Wang, R. He, J. Zhou, G. Chen, D. J. Singh, and Z. Ren, "Tuning the carrier scattering mechanism to effectively improve the thermoelectric properties," Energy Environ. Sci. **10**(3), 799–807 (2017).
[246]S. Ohno, K. Imasato, S. Anand, H. Tamaki, S. D. Kang, P. Gorai, H. K. Sato, E. S. Toberer, T. Kanno, and G. J. Snyder, "Phase boundary mapping to obtain n-type Mg_3Sb_2-based thermoelectrics," Joule **2**(1), 141–154 (2018).
[247]K. Imasato, S. D. Kang, S. Ohno, and G. J. Snyder, "Band engineering in Mg_3Sb_2 by alloying with Mg_3Bi_2 for enhanced thermoelectric performance," Mater. Horiz. **5**(1), 59–64 (2018).
[248]K. Imasato, S. D. Kang, and G. J. Snyder, "Exceptional thermoelectric performance in $Mg_3Sb_{0.6}Bi_{1.4}$ for low-grade waste heat recovery," Energy Environ. Sci. **12**(3), 965–971 (2019).
[249]K. Imasato, M. Wood, S. Anand, J. J. Kuo, and G. J. Snyder, "Understanding the high thermoelectric performance of Mg_3Sb_2-Mg_3Bi_2 alloys," Adv. Energy Sustainable Res. **3**(6), 2100208 (2022).
[250]J. Zhang and B. B. Iversen, "Fermi surface complexity, effective mass, and conduction band alignment in n-type thermoelectric $Mg_3Sb_{2-x}Bi_x$ from first principles calculations," J. Appl. Phys. **126**(8), 085104 (2019).
[251]G. S. Nolas, G. A. Slack, D. T. Morelli, T. M. Tritt, and A. C. Ehrlich, "The effect of rare-earth filling on the lattice thermal conductivity of skutterudites," J. Appl. Phys. **79**(8), 4002–4008 (1996).
[252]G. S. Nolas, J. L. Cohn, and G. A. Slack, "Effect of partial void filling on the lattice thermal conductivity of skutterudites," Phys. Rev. B **58**(1), 164–170 (1998).
[253]G. S. Nolas, D. T. Morelli, and d. T. M. Tritt, "SKUTTERUDITES: A phonon-glass-electron crystal approach to advanced thermoelectric energy conversion applications," Annu. Rev. Mater. Sci. **29**(1), 89–116 (1999).
[254]B. C. Sales, D. Mandrus, B. C. Chakoumakos, V. Keppens, and J. R. Thompson, "Filled skutterudite antimonides: Electron crystals and phonon glasses," Phys. Rev. B **56**(23), 15081–15089 (1997).

[255]B. Duan, J. Yang, J. R. Salvador, Y. He, B. Zhao, S. Wang, P. Wei, F. S. Ohuchi, W. Zhang, R. P. Hermann, O. Gourdon, S. X. Mao, Y. Cheng, C. Wang, J. Liu, P. Zhai, X. Tang, Q. Zhang, and J. Yang, "Electronegative guests in $CoSb_3$," Energy Environ. Sci. **9**(6), 2090–2098 (2016).

[256]H. S. Kim, W. Liu, G. Chen, C.-W. Chu, and Z. Ren, "Relationship between thermoelectric figure of merit and energy conversion efficiency," Proc. Natl. Acad. Sci. U. S. A. **112**(27), 8205–8210 (2015).

[257]J. Mao, H. S. Kim, J. Shuai, Z. Liu, R. He, U. Saparamadu, F. Tian, W. Liu, and Z. Ren, "Thermoelectric properties of materials near the band crossing line in Mg_2Sn–Mg_2Ge–Mg_2Si system," Acta Mater. **103**, 633–642 (2016).

[258]N. Kazem, W. Xie, S. Ohno, A. Zevalkink, G. J. Miller, G. J. Snyder, and S. M. Kauzlarich, "High-temperature thermoelectric properties of the solid–solution Zintl phase $Eu_{11}Cd_6Sb_{12-x}As_x$ ($x < 3$)," Chem. Mater. **26**(3), 1393–1403 (2014).

[259]W. Peng, S. Chanakian, and A. Zevalkink, "Crystal chemistry and thermoelectric transport of layered AM_2X_2 compounds," Inorg. Chem. Front. **5**(8), 1744–1759 (2018).

[260]I. Terasaki, Y. Sasago, and K. Uchinokura, "Large thermoelectric power in $NaCo_2O_4$ single crystals," Phys. Rev. B **56**(20), R12685–R12687 (1997).

[261]R. Funahashi, I. Matsubara, H. Ikuta, T. Takeuchi, U. Mizutani, and S. Sodeoka, "An oxide single crystal with high thermoelectric performance in air," Jpn. J. Appl. Phys. **39**(11B), L1127 (2000).

[262]X.-L. Shi, H. Wu, Q. Liu, W. Zhou, S. Lu, Z. Shao, M. Dargusch, and Z.-G. Chen, "$SrTiO_3$-based thermoelectrics: Progress and challenges," Nano Energy **78**, 105195 (2020).

[263]H. Wang, W. Su, J. Liu, and C. Wang, "Recent development of n-type perovskite thermoelectrics," J. Materiomics **2**(3), 225–236 (2016).

[264]K. Koumoto, Y. Wang, R. Zhang, A. Kosuga, and R. Funahashi, "Oxide thermoelectric materials: A nanostructuring approach," Annu. Rev. Mater. Res. **40**(1), 363–394 (2010).

[265]X. He, S. Nomoto, T. Komatsu, T. Katase, T. Tadano, S. Kitani, H. Yoshida, T. Yamamoto, H. Mizoguchi, K. Ide, H. Hiramatsu, H. Kawaji, H. Hosono, and T. Kamiya, "Hydride anion substitution boosts thermoelectric performance of polycrystalline $SrTiO_3$ via simultaneous realization of reduced thermal conductivity and high electronic conductivity," Adv. Funct. Mater. **33**(28), 2213144 (2023).

[266]T. Katase, S. Nomoto, X. He, S. Kitani, T. Honda, H. Hiramatsu, H. Hosono, and T. Kamiya, "Simultaneous realization of single-crystal-like electron transport and strong phonon scattering in polycrystalline $SrTiO_{3-x}Hx$," ACS Appl. Electron. Mater. **6**(10), 7424–7429 (2024).

[267]M. Kimura, M. Ochiai, X. He, T. Katase, H. Hiramatsu, H. Hosono, and T. Kamiya, "Thermoelectric performance enhancement of environmentally-friendly $SrTiO_3$ epitaxial films by hydrogen substitution," EcoEnergy **3**, 459 (2025).

[268]T. Mori, "Thermoelectric and magnetic properties of rare earth borides: Boron cluster and layered compounds," J. Solid State Chem. **275**, 70–82 (2019).

[269]H. C. Longuet-Higgins and M. d. V. Roberts, "The electronic structure of an icosahedron of boron atoms," Proc. R. Soc. London **230**(1180), 110–119 (1955).

[270]W. N. Lipscomb and D. Britton, "Valence structure of the higher borides," J. Chem. Phys. **33**(1), 275–280 (1960).

[271]T. Mori, "Rare earth higher borides," in *Handbook on the Physics and Chemistry of Rare Earths*, edited by J.-C. G. Bünzli and V. K. Pecharsky (Elsevier, 2020), pp. 39–154.

[272]C. Wood and D. Emin, "Conduction mechanism in boron carbide," Phys. Rev. B **29**(8), 4582–4587 (1984).

[273]M. Bouchacourt and F. Thevenot, "The correlation between the thermoelectric properties and stoichiometry in the boron carbide phase B_4C-$B_{10.5}C$," J. Mater. Sci. **20**(4), 1237–1247 (1985).

[274]H. Werheit, "Boron-rich solids: A chance for high-efficiency high-temperature thermoelectric energy conversion," Mater. Sci. Eng. B **29**(1–3), 228–232 (1995).

[275]T. Mori and T. Nishimura, "Thermoelectric properties of homologous p- and n-type boron-rich borides," J. Solid State Chem. **179**(9), 2908–2915 (2006).

[276]T. Mori, T. Nishimura, W. Schnelle, U. Burkhardt, and Y. Grin, "The origin of the n-type behavior in rare earth borocarbide $Y_{1-x}B_{28.5}C_4$," Dalton Trans. **43**(40), 15048–15054 (2014).

[277]F. Zhang, A. Leithe-Jasper, J. Xu, T. Mori, Y. Matsui, T. Tanaka, and S. Okada, "Novel rare earth boron-rich solids," J. Solid State Chem. **159**(1), 174–180 (2001).

[278]T. Mori and T. Hara, "Hybrid effect to possibly overcome the trade-off between Seebeck coefficient and electrical conductivity," Scr. Mater. **111**, 44–48 (2016).

[279]L. D. Zhao, D. Berardan, Y. L. Pei, C. Byl, L. Pinsard-Gaudart, and N. Dragoe, "Bi_{1-x} Sr_x CuSeO oxyselenides as promising thermoelectric materials," Appl. Phys. Lett. **97**(9), 092118 (2010).

[280]Y. Liu, L.-D. Zhao, Y. Zhu, Y. Liu, F. Li, M. Yu, D.-B. Liu, W. Xu, Y.-H. Lin, and C.-W. Nan, "Synergistically optimizing electrical and thermal transport properties of BiCuSeO via a dual-doping approach," Adv. Energy Mater. **6**(9), 1502423 (2016).

[281]A. M. Kusainova, P. S. Berdonosov, L. G. Akselrud, L. N. Kholodkovskaya, V. A. Dolgikh, and B. A. Popovkin, "New layered compounds with the general composition (MO) (CuSe), where M = Bi, Nd, Gd, Dy, and BiOCuS: Syntheses and crystal structure," J. Solid State Chem. **112**(1), 189–191 (1994).

[282]P. S. Berdonosov, A. M. Kusainova, L. N. Kholodkovskaya, V. A. Dolgikh, L. G. Akselrud, and B. A. Popovkin, "Powder X-ray and IR studies of the new oxyselenides MOCuSe (M = Bi, Gd, Dy)," J. Solid State Chem. **118**(1), 74–77 (1995).

[283]H. Hiramatsu, H. Yanagi, T. Kamiya, K. Ueda, M. Hirano, and H. Hosono, "Crystal structures, optoelectronic properties, and electronic structures of layered oxychalcogenides MCuOch (M = Bi, La; Ch = S, Se, Te): Effects of electronic configurations of M^{3+} ions," Chem. Mater. **20**(1), 326–334 (2008).

[284]M. Y. Toriyama, J. Qu, G. J. Snyder, and P. Gorai, "Defect chemistry and doping of BiCuSeO," J. Mater. Chem. A **9**(36), 20685–20694 (2021).

[285]D. O. Scanlon, J. Buckeridge, C. R. A. Catlow, and G. W. Watson, "Understanding doping anomalies in degenerate p-type semiconductor LaCuOSe," J. Mater. Chem. C **2**(17), 3429–3438 (2014).

[286]C. Barreteau, D. Bérardan, E. Amzallag, L. Zhao, and N. Dragoe, "Structural and electronic transport properties in Sr-doped BiCuSeO," Chem. Mater. **24**(16), 3168–3178 (2012).

[287]J. Li, J. Sui, Y. Pei, C. Barreteau, D. Berardan, N. Dragoe, W. Cai, J. He, and L.-D. Zhao, "A high thermoelectric figure of merit ZT > 1 in Ba heavily doped BiCuSeO oxyselenides," Energy Environ. Sci. **5**(9), 8543–8547 (2012).

[288]J. Li, J. Sui, C. Barreteau, D. Berardan, N. Dragoe, W. Cai, Y. Pei, and L.-D. Zhao, "Thermoelectric properties of Mg doped p-type BiCuSeO oxyselenides," J. Alloys Compd. **551**, 649–653 (2013).

[289]F. Li, T.-R. Wei, F. Kang, and J.-F. Li, "Enhanced thermoelectric performance of Ca-doped BiCuSeO in a wide temperature range," J. Mater. Chem A **1**(38), 11942–11949 (2013).

[290]J. Sui, J. Li, J. He, Y.-L. Pei, D. Berardan, H. Wu, N. Dragoe, W. Cai, and L.-D. Zhao, "Texturation boosts the thermoelectric performance of BiCuSeO oxyselenides," Energy Environ. Sci. **6**(10), 2916–2920 (2013).

[291]J. Li, J. Sui, Y. Pei, X. Meng, D. Berardan, N. Dragoe, W. Cai, and L.-D. Zhao, "The roles of Na doping in BiCuSeO oxyselenides as a thermoelectric material," J. Mater. Chem. A **2**(14), 4903 (2014).

[292]M. Zhang, J. Yang, Q. Jiang, L. Fu, Y. Xiao, Y. Luo, D. Zhang, Y. Cheng, and Z. Zhou, "Multi-role of sodium doping in BiCuSeO on high thermoelectric performance," J. Electron. Mater. **44**(8), 2849–2855 (2015).

[293]J.-L. Lan, C. Deng, W. Ma, G.-K. Ren, Y.-H. Lin, and X. Yang, "Ultra-fast synthesis and high thermoelectric properties of heavy sodium doped BiCuSeO," J. Alloys Compd. **708**, 955–960 (2017).

[294]D. Sun Lee, T.-H. An, M. Jeong, H.-S. Choi, Y. Soo Lim, W.-S. Seo, C.-H. Park, C. Park, and H.-H. Park, "Density of state effective mass and related charge transport properties in K-doped BiCuOSe," Appl. Phys. Lett. **103**(23), 232110 (2013).

[295]J.-L. Lan, W. Ma, C. Deng, G.-K. Ren, Y.-H. Lin, and X. Yang, "High thermoelectric performance of Bi_{1-x} K_x CuSeO prepared by combustion synthesis," J. Mater. Sci. **52**(19), 11569–11579 (2017).

[296]A. Achour, K. Chen, M. J. Reece, and Z. Huang, "Enhanced thermoelectric performance of Cs doped BiCuSeO prepared through eco-friendly flux synthesis," J. Alloys Compd. **735**, 861–869 (2018).

[297]J. Lan, Y. Liu, B. Zhan, Y. Lin, B. Zhang, X. Yuan, W. Zhang, W. Xu, and C.-W. Nan, "Enhanced thermoelectric properties of Pb-doped BiCuSeO ceramics," Adv. Mater. **25**(36), 5086–5090 (2013).

[298]G. Ren, S. Butt, C. Zeng, Y. Liu, B. Zhan, J. Lan, Y. Lin, and C. Nan, "Electrical and thermal transport behavior in Zn-doped BiCuSeO oxyselenides," J. Electron. Mater. **44**(6), 1627–1631 (2015).
[299]Y. Liu, L.-D. Zhao, Y. Liu, J. Lan, W. Xu, F. Li, B.-P. Zhang, D. Berardan, N. Dragoe, Y.-H. Lin, C.-W. Nan, J.-F. Li, and H. Zhu, "Remarkable enhancement in thermoelectric performance of BiCuSeO by Cu deficiencies," J. Am. Chem. Soc. **133**(50), 20112–20115 (2011).
[300]Y. Liu, J. Ding, B. Xu, J. Lan, Y. Zheng, B. Zhan, B. Zhang, Y. Lin, and C. Nan, "Enhanced thermoelectric performance of La-doped BiCuSeO by tuning band structure," Appl. Phys. Lett. **106**(23), 233903 (2015).
[301]S. G. Tan, H. Lei, D. F. Shao, H. Y. Lv, W. J. Lu, Y. N. Huang, Y. Liu, B. Yuan, L. Zu, X. C. Kan, W. H. Song, and Y. P. Sun, "Enhanced low temperature thermoelectric performance of Ag-doped BiCuSeO," Appl. Phys. Lett. **105**(8), 082109 (2014).
[302]Y.-C. Liu, Y.-H. Zheng, B. Zhan, K. Chen, S. Butt, B. Zhang, and Y.-H. Lin, "Influence of Ag doping on thermoelectric properties of BiCuSeO," J. Eur. Ceram. Soc. **35**(2), 845–849 (2015).
[303]M. U. Farooq, S. Butt, K. Gao, X. L. Pang, X. Sun, Asfandiyar, F. Mohmed, A. Ahmad, A. Mahmood, and N. Mahmood, "Improved thermoelectric performance of BiCuSeO by Ag substitution at Cu site," J. Alloys Compd. **691**, 572–577 (2017).
[304]S. D. N. Luu and P. Vaqueiro, "Layered oxychalcogenides: Structural chemistry and thermoelectric properties," J. Materiomics **2**(2), 131–140 (2016).
[305]W. Tang, W. Qian, S. Jia, K. Li, Z. Zhou, J. Lan, Y.-H. Lin, and X. Yang, "BiCuSeO based thermoelectric materials: Innovations and challenges," Mater. Today Phys. **35**, 101104 (2023).
[306]F. Li, J.-F. Li, L.-D. Zhao, K. Xiang, Y. Liu, B.-P. Zhang, Y.-H. Lin, C.-W. Nan, and H.-M. Zhu, "Polycrystalline BiCuSeO oxide as a potential thermoelectric material," Energy Environ. Sci. **5**(5), 7188–7195 (2012).
[307]Y.-L. Pei, J. He, J.-F. Li, F. Li, Q. Liu, W. Pan, C. Barreteau, D. Berardan, N. Dragoe, and L.-D. Zhao, "High thermoelectric performance of oxyselenides: Intrinsically low thermal conductivity of Ca-doped BiCuSeO," NPG Asia Mater. **5**(5), e47–e47 (2013).
[308]G.-K. Ren, J.-L. Lan, S. Butt, K. J. Ventura, Y.-H. Lin, and C.-W. Nan, "Enhanced thermoelectric properties in Pb-doped BiCuSeO oxyselenides prepared by ultrafast synthesis," RSC Adv. **5**(85), 69878–69885 (2015).
[309]Q. Wen, C. Chang, L. Pan, X. Li, T. Yang, H. Guo, Z. Wang, J. Zhang, F. Xu, Z. Zhang, and G. Tang, "Enhanced thermoelectric performance of BiCuSeO by increasing Seebeck coefficient through magnetic ion incorporation," J. Mater. Chem. A **5**(26), 13392–13399 (2017).
[310]S. Das, S. M. Valiyaveettil, K.-H. Chen, S. Suwas, and R. C. Mallik, "Thermoelectric properties of Mn doped BiCuSeO," Mater. Res. Express **6**(8), 086305 (2019).
[311]Z. Li, C. Xiao, S. Fan, Y. Deng, W. Zhang, B. Ye, and Y. Xie, "Dual vacancies: An effective strategy realizing synergistic optimization of thermoelectric property in BiCuSeO," J. Am. Chem. Soc. **137**(20), 6587–6593 (2015).
[312]H. Shao, X. Tan, G.-Q. Liu, J. Jiang, and H. Jiang, "A first-principles study on the phonon transport in layered BiCuOSe," Sci. Rep. **6**(1), 21035 (2016).
[313]J. Ding, B. Xu, Y. Lin, C. Nan, and W. Liu, "Lattice vibration modes of the layered material BiCuSeO and first principles study of its thermoelectric properties," New J. Phys. **17**(8), 083012 (2015).
[314]S. K. Saha, "Exploring the origin of ultralow thermal conductivity in layered BiOCuSe," Phys. Rev. B **92**(4), 041202 (2015).
[315]P. Vaqueiro, R. A. R. Al Orabi, S. D. N. Luu, G. Guélou, A. V. Powell, R. I. Smith, J.-P. Song, D. Wee, and M. Fornari, "The role of copper in the thermal conductivity of thermoelectric oxychalcogenides: Do lone pairs matter?," Phys. Chem. Chem. Phys. **17**(47), 31735–31740 (2015).
[316]M. Yasukawa, K. Ueda, and H. Hosono, "Thermoelectric properties of layered oxyselenides $La_{1-x}Sr_xCuOSe$ (x = 0 to 0.2)," J. Appl. Phys. **95**, 3594–3597 (2004).
[317]N. Wang, M. Li, H. Xiao, X. Zu, and L. Qiao, "Layered LaCuOSe: A promising anisotropic thermoelectric material," Phys. Rev. Appl. **13**(2), 024038 (2020).
[318]J. Yang, G. Yang, G. Zhang, and Y. X. Wang, "Low effective mass leading to an improved ZT value by 32% for n-type BiCuSeO: A first-principles study," J. Mater. Chem A **2**(34), 13923–13931 (2014).
[319]Z. Zhou, X. Tan, G. Ren, Y. Lin, and C. Nan, "Thermoelectric properties of Cl-doped BiCuSeO oxyselenides," J. Electron. Mater. **46**(5), 2593–2598 (2017).
[320]X. Zhang, D. Feng, J. He, and L.-D. Zhao, "Attempting to realize n-type BiCuSeO," J. Solid State Chem. **258**, 510–516 (2018).
[321]X. Zhang, D. Wang, G. Wang, and L.-D. Zhao, "Realizing n-type BiCuSeO through halogens doping," Ceram. Int. **45**(12), 14953–14957 (2019).
[322]S. Tan, C. Gao, C. Wang, Y. Sun, Q. Jing, Q. Meng, T. Zhou, and J. Ren, "Realization of n-type BiCuSeO through Co doping," Solid State Sci. **98**, 106019 (2019).
[323]J.-B. Labégorre, R. Al Rahal Al Orabi, A. Virfeu, J. Gamon, P. Barboux, L. Pautrot-d'Alençon, T. Le Mercier, D. Berthebaud, A. Maignan, and E. Guilmeau, "Electronic band structure engineering and enhanced thermoelectric transport properties in Pb-doped BiCuOS oxysulfide," Chem. Mater. **30**(3), 1085–1094 (2018).
[324]H. Zhu, T. Su, H. Li, C. Pu, D. Zhou, P. Zhu, and X. Wang, "High pressure synthesis, structure and thermoelectric properties of BiCuChO (Ch = S, Se, Te)," J. Eur. Ceram. Soc. **37**(4), 1541–1546 (2017).
[325]H. Yanagi, J. Tate, S. Park, C.-H. Park, and D. Keszler, "p-Type conductivity in wide-band-gap BaCuQF (Q=S, Se)," Appl. Phys. Lett. **82**, 2814–2816 (2003).
[326]C.-H. Park, R. Kykyneshi, A. Yokochi, J. Tate, and D. A. Keszler, "Structure and physical properties of BaCuTeF," J. Solid State Chem. **180**(5), 1672–1677 (2007).
[327]T. Yue, Y. Zhao, J. Ni, S. Meng, and Z. Dai, "Microscopic mechanism of low lattice thermal conductivity in natural superlattice materials BaF (X = Cu, Ag; Y = Se, Te) including fully quartic anharmonicity," Phys. Rev. B **107**(2), 024301 (2023).
[328]J. S. O. Evans, E. B. Brogden, A. L. Thompson, and R. L. Cordiner, "Synthesis and characterisation of the new oxyselenide $Bi_2YO_4Cu_2Se_2$," Chem. Commun. **2002**(8), 912–913.
[329]Y. Yang, J. Han, Z. Zhou, M. Zou, Y. Xu, Y. Zheng, C.-W. Nan, and Y.-H. Lin, "Seeking new layered oxyselenides with promising thermoelectric performance," Adv. Funct. Mater. **32**(18), 2113164 (2022).
[330]S. G. Tan, D. F. Shao, W. J. Lu, B. Yuan, Y. Liu, J. Yang, W. H. Song, H. Lei, and Y. P. Sun, "CuSe-based layered compound $Bi_2YO_4Cu_2Se_2$ as a quasi-two-dimensional metal," Phys. Rev. B **90**(8), 085144 (2014).
[331]S. Tan, C. Gao, C. Wang, Q. Jing, T. Zhou, G. Yin, M. Sun, F. Xing, R. Cao, and Y. Sun, "Synthesis, structure and physical properties of the new layered oxyselenides $Bi_2LnO_4Cu_2Se_2$ (Ln = rare earth)," R. Soc. Open Sci. **7**(10), 201078 (2020).
[332]Y. Xiao, Y. Pei, C. Chang, X. Zhang, X. Tan, X. Ye, S. Gong, Y. Lin, J. He, and L.-D. Zhao, "Electrical and thermal transport properties of layered $Bi_2YO_4Cu_2Se_2$," J. Solid State Chem. **239**, 178–183 (2016).
[333]K. Ueda, S. Hirose, H. Kawazoe, and H. Hosono, "Electrical and optical properties of layered oxysulfides with CuS layers: Sr−Cu−M−O−S system (M = Zn, Ga, In)," Chem. Mater. **13**(5), 1880–1883 (2001).
[334]S. Jin, X. Chen, J. Guo, M. Lei, J. Lin, J. Xi, W. Wang, and W. Wang, "$Sr_2Mn_3Sb_2O_2$ type oxyselenides: Structures, magnetism, and electronic properties of $Sr_2AO_2M_2Se_2$ (A=Co, Mn; M=Cu, Ag)," Inorg. Chem. **51**(19), 10185–10192 (2012).
[335]T. L. Chou, O. Mustonen, T. S. Tripathi, and M. Karppinen, "Isovalent Ca and Ba substitutions in thermoelectric layer-structured oxyselenide $Sr_2CoO_2Cu_2Se_2$," J. Phys.: Condens. Matter **28**(3), 035802 (2016).
[336]D. Song, G. Guélou, T. Mori, M. Ochi, K. Kuroki, H. Fujihisa, Y. Gotoh, Y. Iwasa, H. Eisaki, and H. Ogino, "Synthesis and the physical properties of layered copper oxytellurides $Sr_2TMCu_2Te_2O_2$ (TM = Mn, Co, Zn)," J. Mater. Chem. C **6**(45), 12260–12266 (2018).
[337]H. Hirose, K. Ueda, H. Kawazoe, and H. Hosono, "Electronic structure of $Sr_2Cu_2ZnO_2S_2$ layered oxysulfide with CuS layers," Chem. Mater. **14**(3), 1037–1041 (2002).
[338]X. He, T. Cho, T. Katase, K. Hanzawa, S. Kitani, H. Hiramatsu, H. Hosono, and T. Kamiya, "Wide-gap p-type layered oxychalcogenides AE_2CuInO_3Ch (AE: Alkaline earth; Ch: Chalcogen): Unusually low residual carrier concentration and green-to-red emission," Chem. Mater. **36**(12), 6086–6099 (2024).
[339]K. Bu, J. Huang, M. Luo, M. Guan, C. Zheng, J. Pan, X. Zhang, S. Wang, W. Zhao, X. Shi, L. Xu, and F. Huang, "Observation of high Seebeck coefficient and low thermal conductivity in [SrO]-intercalated $CuSbSe_2$ compound," Chem. Mater. **30**(16), 5539–5543 (2018).

[340]K. Bu, M. Luo, R. Wang, X. Zhang, J. He, D. Wang, W. Zhao, and F. Huang, "Enhanced photoelectric $SrOCuSbS_2$ of a [SrO]-intercalated $CuSbS_2$ structure," Inorg. Chem. **58**(1), 69–72 (2019).
[341]M. Luo, K. Bu, X. Zhang, J. Huang, R. Wang, and F. Huang, "Intrinsically low thermal conductivity in a p-type semiconductor $SrOCuBiSe_2$ with a [SrO]-intercalated $CuBiSe_2$ structure," Chem. Commun. **56**(31), 4356–4359 (2020).
[342]D. Zhang, J. Yang, Q. Jiang, L. Fu, Y. Xiao, Y. Luo, and Z. Zhou, "Ternary $CuSbSe_2$ chalcostibite: Facile synthesis, electronic-structure and thermoelectric performance enhancement," J. Mater. Chem. A **4**(11), 4188–4193 (2016).
[343]H.-J. Förster, L. Bindi, and C. J. Stanley, "Grundmannite, $CuBiSe_2$, the Se-analogue of emplectite, a new mineral from the El Dragón mine, Potosí, Bolivia," Eur. J. Mineral. **28**(2), 467–477 (2016).
[344]L.-C. Yin, W.-D. Liu, M. Li, Q. Sun, H. Gao, D.-Z. Wang, H. Wu, Y.-F. Wang, X.-L. Shi, Q. Liu, and Z.-G. Chen, "High carrier mobility and high figure of merit in the $CuBiSe_2$ alloyed GeTe," Adv. Energy Mater. **11**(45), 2102913 (2021).
[345]C. Zhang, J. He, R. McClain, H. Xie, S. Cai, L. N. Walters, J. Shen, F. Ding, X. Zhou, C. D. Malliakas, J. M. Rondinelli, M. G. Kanatzidis, C. Wolverton, V. P. Dravid, and K. R. Poeppelmeier, "Low thermal conductivity in heteroanionic materials with layers of homoleptic polyhedra," J. Am. Chem. Soc. **144**(6), 2569–2579 (2022).
[346]A. BaQais, A. Curutchet, A. Ziani, H. Ait Ahsaine, P. Sautet, K. Takanabe, and T. Le Bahers, "Bismuth silver oxysulfide for photoconversion applications: Structural and optoelectronic properties," Chem. Mater. **29**(20), 8679–8689 (2017).
[347]R. Zhao, Y. Zhou, Y. Dong, S. Dong, F. Zhang, J. Zhou, F. He, S. Gai, and P. Yang, "Ball-milling fabrication of BiAgOS nanoparticles for 808 nm light mediated photodynamic/photothermal treatment," Chem. Eng. J. **411**, 128568 (2021).
[348]R. D. Shannon, "Revised effective ionic radii and systematic studies of interatomic distances in halides and chalcogenides," Acta Cryst. A **32**(5), 751–767 (1976).
[349]M. Mukherjee and A. K. Singh, "Strong chemical bond hierarchy leading to exceptionally high thermoelectric figure of merit in oxychalcogenide AgBiTeO," ACS Appl. Mater. Interfaces **12**(7), 8280–8287 (2020).
[350]S. Bai, J. Zhang, M. Wu, D. Luo, D. Wan, X. Li, and S. Tang, "Theoretical prediction of thermoelectric performance for layered LaAgOX (X = S, Se) materials in consideration of the four-phonon and multiple carrier scattering processes," Small Methods **7**(3), e2201368 (2023).
[351]Y. Mizuguchi, H. Fujihisa, Y. Gotoh, K. Suzuki, H. Usui, K. Kuroki, S. Demura, Y. Takano, H. Izawa, and O. Miura, "BiS_2-based layered superconductor $Bi_4O_4S_3$," Phys. Rev. B: Condens. Matter Mater. Phys. **86**(22), 220510 (2012).
[352]S. Demura, Y. Mizuguchi, K. Deguchi, H. Okazaki, H. Hara, T. Watanabe, S. James Denholme, M. Fujioka, T. Ozaki, H. Fujihisa, Y. Gotoh, O. Miura, T. Yamaguchi, H. Takeya, and Y. Takano, "New member of BiS_2-based superconductor $NdO_{1-x}F_xBiS_2$," J. Phys. Soc. Jpn. **82**(3), 033708 (2013).
[353]J. Xing, S. Li, X. Ding, H. Yang, and H.-H. Wen, "Superconductivity appears in the vicinity of semiconducting-like behavior in $CeO_{1-x}F_xBiS_2$," Phys. Rev. B **86**(21), 214518 (2012).
[354]R. Jha, A. Kumar, S. Kumar Singh, and V. P. S. Awana, "Synthesis and superconductivity of new BiS_2 based superconductor $PrO_{0.5}F_{0.5}BiS_2$," J. Supercond. Nov. Magn. **26**(3), 499–502 (2013).
[355]D. Yazici, K. Huang, B. D. White, A. H. Chang, A. J. Friedman, and M. B. Maple, "Superconductivity of F-substitutedLnOBiS$_2$(Ln=La, Ce, Pr, Nd, Yb) compounds," Philos. Mag. **93**(6), 673–680 (2013).
[356]K. Deguchi, Y. Mizuguchi, S. Demura, H. Hara, T. Watanabe, S. J. Denholme, M. Fujioka, H. Okazaki, T. Ozaki, H. Takeya, T. Yamaguchi, O. Miura, and Y. Takano, "Evolution of superconductivity in $LaO_{1-x}F_xBiS_2$ prepared by high-pressure technique," Europhys. Lett. **101**(1), 17004 (2013).
[357]D. Yazici, K. Huang, B. D. White, I. Jeon, V. W. Burnett, A. J. Friedman, I. K. Lum, M. Nallaiyan, S. Spagna, and M. B. Maple, "Superconductivity induced by electron doping in $La_{1-x}M_xOBiS_2$(M=Ti, Zr, Hf, Th)," Phys. Rev. B **87**(17), 174512 (2013).
[358]Y. Mizuguchi, S. Demura, K. Deguchi, Y. Takano, H. Fujihisa, Y. Gotoh, H. Izawa, and O. Miura, "Superconductivity in novel BiS_2-based layered superconductor $LaO_{1-x}F_xBiS_2$," J. Phys. Soc. Jpn. **81**(11), 114725 (2012).
[359]X. Lin, X. Ni, B. Chen, X. Xu, X. Yang, J. Dai, Y. Li, X. Yang, Y. Luo, Q. Tao, G. Cao, and Z. Xu, "Superconductivity induced by La doping in $Sr_{1-x}La_xFBiS_2$," Phys. Rev. B: Condens. Matter Mater. Phys. **87**, 020504 (2013).
[360]H. Sakai, D. Kotajima, K. Saito, H. Wadati, Y. Wakisaka, M. Mizumaki, K. Nitta, Y. Tokura, and S. Ishiwata, "Insulator-to-superconductor transition upon electron doping in a BiS_2-based superconductor $Sr_{1-x}La_xFBiS_2$," J. Phys. Soc. Jpn. **83**(1), 014709 (2014).
[361]R. Jha, B. Tiwari, and V. P. S. Awana, "Appearance of bulk superconductivity under hydrostatic pressure in $Sr_{0.5}RE_{0.5}FBiS_2$ (RE = Ce, Nd, Pr, and Sm) compounds," J. Appl. Phys. **117**(1), 013901 (2015).
[362]H. Zhai, Z. Tang, H. Jiang, K. Xu, K. Zhang, P. Zhang, J. Bao, Y.-L. Sun, W. Jiao, I. Nowik, I. Felner, Y. Li, X.-F. Xu, Q. Tao, C. Feng, Z.-A. Xu, and G. Cao, "Possible charge-density wave, superconductivity, and f-electron valence instability in $EuBiS_2F$," Phys. Rev. B **90**, 064518 (2014).
[363]H.-F. Zhai, P. Zhang, S.-Q. Wu, C.-Y. He, Z.-T. Tang, H. Jiang, Y.-L. Sun, J.-K. Bao, I. Nowik, I. Felner, Y.-W. Zeng, Y.-K. Li, X.-F. Xu, Q. Tao, Z.-A. Xu, and G.-H. Cao, "Anomalous Eu valence state and superconductivity in undoped $Eu_3Bi_2S_4F_4$," J. Am. Chem. Soc. **136**(43), 15386–15393 (2014).
[364]P. Zhang, H. F. Zhai, Z. J. Tang, L. Li, Y. K. Li, Q. Chen, J. Chen, Z. Wang, C. M. Feng, G. H. Cao, and Z. A. Xu, "Superconductivity enhanced by Se doping in $Eu_3Bi_2(S,Se)_4F_4$," Europhys. Lett. **111**(2), 27002 (2015).
[365]J. Wu, H. Yuan, M. Meng, C. Chen, Y. Sun, Z. Chen, W. Dang, C. Tan, Y. Liu, J. Yin, Y. Zhou, S. Huang, H. Q. Xu, Y. Cui, H. Y. Hwang, Z. Liu, Y. Chen, B. Yan, and H. Peng, "High electron mobility and quantum oscillations in non-encapsulated ultrathin semiconducting Bi_2O_2Se," Nat. Nanotech. **12**(6), 530–534 (2017).
[366]C. Chen, M. Wang, J. Wu, H. Fu, H. Yang, Z. Tian, T. Tu, H. Peng, Y. Sun, X. Xu, J. Jiang, N. B. M. Schröter, Y. Li, D. Pei, S. Liu, S. A. Ekahana, H. Yuan, J. Xue, G. Li, J. Jia, Z. Liu, B. Yan, H. Peng, and Y. Chen, "Electronic structures and unusually robust bandgap in an ultrahigh-mobility layered oxide semiconductor, Bi_2O_2Se," Sci. Adv. **4**(9), eaat8355 (2018).
[367]T. Ghosh, M. Samanta, A. Vasdev, K. Dolui, J. Ghatak, T. Das, G. Sheet, and K. Biswas, "Ultrathin free-standing nanosheets of Bi_2O_2Se: Room temperature ferroelectricity in self-assembled charged layered heterostructure," Nano Lett. **19**(8), 5703–5709 (2019).
[368]R. Higashinaka, H. Endo, J. Kajitani, T. D. Matsuda, and Y. Aoki, "Single crystal growth and physical properties of BiS_2-layered compound $Eu_3Bi_2S_4F_4$," Phys. B: Condens. Matter **536**, 824–826 (2018).
[369]Y.-L. Sun, A. Ablimit, H.-F. Zhai, J.-K. Bao, Z.-T. Tang, X.-B. Wang, N.-L. Wang, C.-M. Feng, and G.-H. Cao, "Design and synthesis of a new layered thermoelectric material $LaPbBiS_3O$," Inorg. Chem. **53**(20), 11125–11129 (2014).
[370]H. Boller, "Die Kristallstruktur von Bi_2O_2Se," Monatsh. Chem. **104**(4), 916–919 (1973).
[371]S.-L. Wu, K. Sumida, K. Miyamoto, K. Taguchi, T. Yoshikawa, A. Kimura, Y. Ueda, M. Arita, M. Nagao, S. Watauchi, I. Tanaka, and T. Okuda, "Direct evidence of hidden local spin polarization in a centrosymmetric superconductor $LaO_{0.55}F_{0.45}BiS_2$," Nat. Commun. **8**(1), 1919 (2017).
[372]A. Omachi, J. Kajitani, T. Hiroi, O. Miura, and Y. Mizuguchi, "High-temperature thermoelectric properties of novel layered bismuth-sulfide $LaO_{1-x}F_xBiS_2$," J. Appl. Phys. **115**(8), 083909 (2014).
[373]Y. Mizuguchi, A. Omachi, Y. Goto, Y. Kamihara, M. Matoba, T. Hiroi, J. Kajitani, and O. Miura, "Enhancement of thermoelectric properties by Se substitution in layered bismuth-chalcogenide $LaOBiS_{2-x}Se_x$," J. Appl. Phys. **116**(16), 163915 (2014).
[374]A. Nishida, O. Miura, C.-H. Lee, and Y. Mizuguchi, "High thermoelectric performance and low thermal conductivity of densified LaOBiSSe," Appl. Phys. Express **8**(11), 111801 (2015).
[375]H. Lei, K. Wang, M. Abeykoon, E. S. Bozin, and C. Petrovic, "New layered fluorosulfide $SrFBiS_2$," Inorg. Chem. **52**(18), 10685–10689 (2013).
[376]H. Huang, C. Lin, S. Li, K. Guo, J. Zhang, W. Lyu, J. Zhang, J. Xing, Y. Jiang, J. Yang, and J. Luo, "Enhancing thermoelectric performance of $SrFBiS_2$−Se via band engineering and structural texturing," J. Materiomics **8**(2), 302–310 (2022).
[377]Y. Goto, A. Miura, R. Sakagami, Y. Kamihara, C. Moriyoshi, Y. Kuroiwa, and Y. Mizuguchi, "Synthesis, crystal structure, and thermoelectric properties of

layered antimony selenides $REOSbSe_2$ (RE = La, Ce)," J. Phys. Soc. Jpn. **87**(7), 074703 (2018).
[378]Y. Mizuguchi, A. Miura, A. Nishida, O. Miura, K. Tadanaga, N. Kumada, C. H. Lee, E. Magome, C. Moriyoshi, and Y. Kuroiwa, "Compositional and temperature evolution of crystal structure of new thermoelectric compound $LaOBiS_{2-x}Se_x$," J. Appl. Phys. **119**(15), 155103 (2016).
[379]C. H. Lee, A. Nishida, T. Hasegawa, H. Nishiate, H. Kunioka, S. Ohira-Kawamura, M. Nakamura, K. Nakajima, and Y. Mizuguchi, "Effect of rattling motion without cage structure on lattice thermal conductivity in $LaOBiS_{2-x}Se_x$," Appl. Phys. Lett. **112**(2), 023903 (2018).
[380]S. G. Tan, L. J. Li, Y. Liu, P. Tong, B. C. Zhao, W. J. Lu, and Y. P. Sun, "Superconducting and thermoelectric properties of new layered superconductor $Bi_4O_4S_3$," Phys. C Supercond. **483**, 94–96 (2012).
[381]K. Kurematsu, M. Ochi, H. Usui, and K. Kuroki, "First-principles study of $LaOPbBiS_3$ and its analogous compounds as thermoelectric materials," J. Phys. Soc. Jpn. **89**(2), 024702 (2020).
[382]P. Ruleova, C. Drasar, P. Lostak, C.-P. Li, S. Ballikaya, and C. Uher, "Thermoelectric properties of Bi_2O_2Se," Mater. Chem. Phys. **119**(1), 299–302 (2010).
[383]J. Wang, W. Hu, Z. Lou, Z. Xu, X. Yang, T. Wang, and X. Lin, "Thermoelectric properties of Bi_2O_2Se single crystals," Appl. Phys. Lett. **119**(8), 081901 (2021).
[384]C. Wang, G. Ding, X. Wu, S. Wei, and G. Gao, "Electron and phonon transport properties of layered Bi_2O_2Se and Bi_2O_2Te from first-principles calculations," New J. Phys. **20**(12), 123014 (2018).
[385]B. Zhan, S. Butt, Y. Liu, J.-L. Lan, C.-W. Nan, and Y.-H. Lin, "High-temperature thermoelectric behaviors of Sn-doped n-type Bi_2O_2Se ceramics," J. Electroceram. **34**(2–3), 175–179 (2015).
[386]R. Liu, J.-L. Lan, X. Tan, Y.-C. Liu, G.-K. Ren, C. Liu, Z.-F. Zhou, C.-W. Nan, and Y.-H. Lin, "Carrier concentration optimization for thermoelectric performance enhancement in n-type Bi_2O_2Se," J. Eur. Ceram. Soc. **38**(7), 2742–2746 (2018).
[387]P. Ruleova, T. Plechacek, J. Kasparova, M. Vlcek, L. Benes, P. Lostak, and C. Drasar, "Enhanced thermoelectric performance of n-type Bi_2O_2Se ceramics induced by Ge doping," J. Electron. Mater. **47**(2), 1459–1466 (2018).
[388]X. Tan, Y. Liu, R. Liu, Z. Zhou, C. Liu, J.-L. Lan, Q. Zhang, Y.-H. Lin, and C.-W. Nan, "Synergistical enhancement of thermoelectric properties in n-type Bi_2O_2Se by carrier engineering and hierarchical microstructure," Adv. Energy Mater. **9**(31), 1900354 (2019).
[389]M. Kim, D. Park, and J. Kim, "Enhancement of Bi_2O_2Se thermoelectric power factor via Nb doping," J. Alloys Compd. **851**, 156905 (2021).
[390]X. Tan, J.-L. Lan, G. Ren, Y. Liu, Y.-H. Lin, and C.-W. Nan, "Enhanced thermoelectric performance of n-type Bi_2O_2Se by Cl-doping at Se site," J. Am. Ceram. Soc. **100**(4), 1494–1501 (2017).
[391]X. Tan, J.-L. Lan, K. Hu, B. Xu, Y. Liu, P. Zhang, X.-Z. Cao, Y. Zhu, W. Xu, Y.-H. Lin, and C.-W. Nan, "Boosting the thermoelectric performance of Bi_2O_2Se by isovalent doping," J. Am. Ceram. Soc. **101**(10), 4634–4644 (2018).
[392]N. Yang, L. Pan, C. Chen, and Y. Wang, "Effects of Sb-doping on the electron-phonon transport properties of Bi_2O_2Se," J. Alloys Compd. **858**, 157748 (2021).
[393]B. Zhan, Y. Liu, X. Tan, J.-L. Lan, Y.-H. Lin, and C.-W. Nan, "Enhanced thermoelectric properties of Bi_2O_2Se ceramics by Bi deficiencies," J. Am. Ceram. Soc. **98**(8), 2465–2469 (2015).
[394]T. Van Quang and M. Kim, "Role of O and Se defects in the thermoelectric properties of bismuth oxide selenide," J. Appl. Phys. **120**(19), 195105 (2016).
[395]L. Pan, W.-D. Liu, J.-Y. Zhang, X.-L. Shi, H. Gao, Q.-F. Liu, X. Shen, C. Lu, Y.-F. Wang, and Z.-G. Chen, "Synergistic effect approaching record-high figure of merit in the shear exfoliated n-type $Bi_2O_{2-2x}Te_{2x}Se$," Nano Energy **69**, 104394 (2020).
[396]H.-Y. Song, X.-J. Ge, M.-Y. Shang, J. Zhang, and J.-T. Lü, "Intrinsically low thermal conductivity of bismuth oxychalcogenides originating from interlayer coupling," Phys. Chem. Chem. Phys. **21**(33), 18259–18264 (2019).
[397]S. D. N. Luu and P. Vaqueiro, "Synthesis, characterisation and thermoelectric properties of the oxytelluride Bi_2O_2Te," J. Solid State Chem. **226**, 219–223 (2015).
[398]F. Yang, J. Wu, A. Suwardi, Y. Zhao, B. Liang, J. Jiang, J. Xu, D. Chi, K. Hippalgaonkar, J. Lu, and Z. Ni, "Gate-tunable polar optical phonon to piezoelectric scattering in few-layer Bi_2O_2Se for high-performance thermoelectrics," Adv. Mater. **33**(4), e2004786 (2021).
[399]D. Guo, C. Hu, Y. Xi, and K. Zhang, "Strain effects to optimize thermoelectric properties of doped Bi_2O_2Se via Tran–Blaha modified Becke–Johnson density functional theory," J. Phys. Chem. C **117**(41), 21597–21602 (2013).
[400]W. Chen, U. Khan, S. Feng, B. Ding, X. Xu, and B. Liu, "High-fidelity transfer of 2D Bi_2O_2Se and its mechanical properties," Adv. Funct. Mater. **30**(43), 2004960 (2020).
[401]G. Liu, H. Sun, J. Zhou, Q. Li, and X. G. Wan, "Thermal properties of layered oxychalcogenides BiCuOCh (Ch = S, Se, and Te): A first-principles calculation," J. Appl. Phys. **119**(18), 185109 (2016).
[402]J. Li, W. Zhai, C. Zhang, Y. Yan, P.-F. Liu, and G. Yang, "Anharmonicity and ultralow thermal conductivity in layered oxychalcogenides BiAgOCh (Ch = S, Se, and Te)," Mater. Adv. **2**(14), 4876–4882 (2021).
[403]P. Vaqueiro, G. Guélou, M. Stec, E. Guilmeau, and A. V. Powell, "A copper-containing oxytelluride as a promising thermoelectric material for waste heat recovery," J. Mater. Chem. A **1**(3), 520–523 (2013).
[404]M. Amsler, L. Ward, V. I. Hegde, M. G. Goesten, X. Yi, and C. Wolverton, "Ternary mixed-anion semiconductors with tunable band gaps from machine-learning and crystal structure prediction," Phys. Rev. Mater. **3**(3), 035404 (2019).
[405]J. Shen, V. I. Hegde, J. He, Y. Xia, and C. Wolverton, "High-throughput computational discovery of ternary mixed-anion oxypnictides," Chem. Mater. **33**(24), 9486–9500 (2021).
[406]J. Shen, S. D. Griesemer, A. Gopakumar, B. Baldassarri, J. E. Saal, M. Aykol, V. I. Hegde, and C. Wolverton, "Reflections on one million compounds in the open quantum materials database (OQMD)," J. Phys. Mater. **5**(3), 031001 (2022).
[407]D. Kato, P. Song, H. Ubukata, H. Taguro, C. Tassel, K. Miyazaki, T. Abe, K. Nakano, K. Hongo, R. Maezono, and H. Kageyama, "Evolutionary algorithm directed synthesis of mixed anion compounds LaF_2 X (X=Br, I) and $LaFI_2$," Angew. Chem. Int. Ed. **62**(30), e202301416 (2023).
[408]D. Han, B. Zhu, Z. Cai, K. B. Spooner, S. S. Rudel, W. Schnick, T. Bein, D. O. Scanlon, and H. Ebert, "Discovery of multi-anion antiperovskites X_6NFSn_2 (X = Ca, Sr) as promising thermoelectric materials by computational screening," Matter **7**(1), 158–174 (2024).
[409]J. Wang, B.-Y. Zhang, H.-J. Kang, Y. Li, X. Yaer, J.-F. Li, Q. Tan, S. Zhang, G.-H. Fan, C.-Y. Liu, L. Miao, D. Nan, T.-M. Wang, and L.-D. Zhao, "Record high thermoelectric performance in bulk $SrTiO_3$ via nano-scale modulation doping," Nano Energy **35**, 387–395 (2017).
[410]T. Maiti, M. Saxena, and P. Roy, "Double perovskite ($Sr_2B'B''O_6$) oxides for high-temperature thermoelectric power generation—A review," J. Mater. Res. **34**(1), 107–125 (2019).
[411]K. H. Lee, S. W. Kim, H. Ohta, and K. Koumoto, "Ruddlesden-Popper phases as thermoelectric oxides: Nb-doped $SrO(SrTiO_3)n$ (n=1,2)," J. Appl. Phys. **100**(6), 063717 (2006).
[412]H. Wu, X.-L. Shi, W.-D. Liu, M. Li, H. Gao, W. Zhou, Z. Shao, Y. Wang, Q. Liu, and Z.-G. Chen, "Double perovskite Pr_2CoFeO_6 thermoelectric oxide: Roles of Sr-doping and micro/nanostructuring," Chem. Eng. J. **425**, 130668 (2021).
[413]P. Acharyya, T. Ghosh, K. Pal, K. Kundu, K. Singh Rana, J. Pandey, A. Soni, U. V. Waghmare, and K. Biswas, "Intrinsically ultralow thermal conductivity in Ruddlesden-Popper 2D perovskite $Cs_2PbI_2Cl_2$: Localized anharmonic vibrations and dynamic octahedral distortions," J. Am. Chem. Soc. **142**(36), 15595–15603 (2020).
[414]N. A. Benedek and C. J. Fennie, "Hybrid improper ferroelectricity: A mechanism for controllable polarization-magnetization coupling," Phys. Rev. Lett. **106**(10), 107204 (2011).
[415]A. T. Mulder, N. A. Benedek, J. M. Rondinelli, and C. J. Fennie, "Turning ABO3 antiferroelectrics into ferroelectrics: Design rules for practical rotation-driven ferroelectricity in double perovskites and $A_3B_2O_7$ Ruddlesden-popper compounds," Adv. Funct. Mater. **23**(38), 4810–4820 (2013).
[416]Y. S. Oh, X. Luo, F.-T. Huang, Y. Wang, and S.-W. Cheong, "Experimental demonstration of hybrid improper ferroelectricity and the presence of abundant charged walls in $(Ca,Sr)_3Ti_2O_7$ crystals," Nat. Mater. **14**(4), 407–413 (2015).

[417]P. Acharyya, T. Ghosh, K. Pal, K. S. Rana, M. Dutta, D. Swain, M. Etter, A. Soni, U. V. Waghmare, and K. Biswas, "Glassy thermal conductivity in $Cs_3Bi_2I_6Cl_3$ single crystal," Nat. Commun. **13**(1), 5053 (2022).
[418]Y. Okamoto, A. Sakamaki, and K. Takenaka, "Thermoelectric properties of antiperovskite calcium oxides Ca_3PbO and Ca_3SnO," J. Appl. Phys. **119**(20), 205106 (2016).
[419]X. He, S. Kimura, T. Katase, T. Tadano, S. Matsuishi, M. Minohara, H. Hiramatsu, H. Kumigashira, H. Hosono, and T. Kamiya, "Inverse-perovskite Ba_3BO (B = Si and Ge) as a high performance environmentally benign thermoelectric material with low lattice thermal conductivity," Adv. Sci. **11**(10), 2307058 (2024).
[420]M. Ochi and K. Kuroki, "Comparative first-principles study of antiperovskite oxides and nitrides as thermoelectric material: Multiple Dirac cones, low-dimensional band dispersion, and high valley degeneracy," Phys. Rev. Appl. **12**(3), 034009 (2019).
[421]J. Yue, Y. Liu, W. Ren, S. Lin, C. Shen, H. Kumar Singh, T. Cui, T. Tadano, and H. Zhang, "Role of atypical temperature-responsive lattice thermal transport on the thermoelectric properties of antiperovskites Mg_3XN (X = P, As, Sb, Bi)," Mater. Today Phys. **41**, 101340 (2024).
[422]Y. Zhao, C. Lian, S. Zeng, Z. Dai, S. Meng, and J. Ni, "Quartic anharmonicity and anomalous thermal conductivity in cubic antiperovskites A_3BO (A=K, Rb; B=Br, Au)," Phys. Rev. B: Condens. Matter **101**(18), 184303 (2020).
[423]Y. Zhao, C. Lian, S. Zeng, Z. Dai, S. Meng, and J. Ni, "Anomalous electronic and thermoelectric transport properties in cubic Rb_3AuO antiperovskite," Phys. Rev. B **102**(9), 094314 (2020).
[424]P. Pegolo, S. Baroni, and F. Grasselli, "Temperature- and vacancy-concentration-dependence of heat transport in Li_3ClO from multi-method numerical simulations," npj Comput. Mater. **8**(1), 24 (2022).
[425]S. Zeng, Q. Shen, L. Guo, Y. Zhao, H. Huang, G. Li, and Y. Tu, "Remarkable thermoelectric efficiency of cubic antiperovskites Rb_3X(Se & Te)I with strong anharmonicity," J. Mater. Chem. A **11**(44), 24047–24056 (2023).
[426]S. Zeng, L. Guo, Z. Huang, Q. Shen, Y. Zhao, H. Huang, G. Li, and Y. Tu, "Anomalous thermal conductivity and high thermoelectric performance of cubic antiperovskites K_3IX(Se & Te)," Chem. Mater. **36**(1), 211–218 (2024).
[427]S. Zeng, X. Yan, Q. Shen, Y. Tu, H. Huang, and G. Li, "Low lattice thermal conductivities and good thermoelectric performance of hexagonal antiperovskites X(Ba & Sr)$_3$BiN with quartic anharmonicity," Phys. Chem. Chem. Phys. **25**(39), 26507–26514 (2023).
[428]W. Rahim, J. M. Skelton, and D. O. Scanlon, "Ca_4Sb_2O and Ca_4Bi_2O: Two promising mixed-anion thermoelectrics," J. Mater. Chem. A **9**(36), 20417–20435 (2021).
[429]J. Gebhardt and A. M. Rappe, "Adding to the perovskite universe: Inverse-hybrid perovskites," ACS Energy Lett. **2**(12), 2681–2685 (2017).
[430]N. Charles, R. J. Saballos, and J. M. Rondinelli, "Structural diversity from anion order in heteroanionic materials," Chem. Mater. **30**(10), 3528–3537 (2018).
[431]M. Yang, J. Oró-Solé, J. A. Rodgers, A. B. Jorge, A. Fuertes, and J. P. Attfield, "Anion order in perovskite oxynitrides," Nat. Chem. **3**(1), 47–52 (2011).
[432]H. Lin, G. Tan, J.-N. Shen, S. Hao, L.-M. Wu, N. Calta, C. Malliakas, S. Wang, C. Uher, C. Wolverton, and M. G. Kanatzidis, "Concerted rattling in $CsAg_5Te_3$ leading to ultralow thermal conductivity and high thermoelectric performance," Angew. Chem. Int. Ed. **55**(38), 11431–11436 (2016).
[433]J. M. Hodges, Y. Xia, C. D. Malliakas, G. C. B. Alexander, M. K. Y. Chan, and M. G. Kanatzidis, "Two-dimensional $CsAg_5Te_{3-x}S_x$ semiconductors: Multi-anion chalcogenides with dynamic disorder and ultralow thermal conductivity," Chem. Mater. **30**(20), 7245–7254 (2018).
[434]J. M. Hodges, Y. Xia, C. D. Malliakas, T. J. Slade, C. Wolverton, and M. G. Kanatzidis, "Mixed-valent copper chalcogenides: Tuning structures and electronic properties using multiple anions," Chem. Mater. **32**(23), 10146–10154 (2020).
[435]Z. Liu, W. Zhang, W. Gao, and T. Mori, "A material catalogue with glass-like thermal conductivity mediated by crystallographic occupancy for thermoelectric application," Energy Environ. Sci. **14**(6), 3579–3587 (2021).
[436]P. Jafarzadeh, M. Oudah, A. Assoud, N. Farahi, E. Müller, and H. Kleinke, "High thermoelectric performance of $Ba_3Cu_{16-x}(S,Te)_{11}$," J. Mater. Chem. C **6**(47), 13043–13048 (2018).
[437]P. Jafarzadeh, M. R. Rodrigues, Y. Shi, A. Assoud, T. Zou, J. B. Kycia, and H. Kleinke, "Effect of mixed occupancies on the thermoelectric properties of $BaCu_{6-x}Se_{1-y}Te_{6+y}$ polychalcogenides," Dalton Trans. **48**(25), 9357–9364 (2019).
[438]B. Kuropatwa, Y. Cui, A. Assoud, and H. Kleinke, "Crystal structure and physical properties of the new selenide−tellurides $Ba_3Cu_{17-x}(Se,Te)_{11}$," Chem. Mater. **21**(1), 88–93 (2009).
[439]B. A. Kuropatwa, A. Assoud, and H. Kleinke, "Crystal structure and physical properties of the new chalcogenides $Ba_3Cu_{(17-x)}(S,Te)_{11}$ and $Ba_3Cu_{(17-x)}(S,Te)_{11.5}$ with two different Cu clusters," Inorg. Chem. **50**(16), 7831–7837 (2011).
[440]O. Mayasree, C. R. Sankar, A. Assoud, and H. Kleinke, "New barium copper chalcogenides synthesized using two different chalcogen atoms: $Ba_2Cu_{(6-x)}STe_4$ and $Ba_2Cu_{(6-x)}Se_{(y)}Te_{(5-y)}$," Inorg. Chem. **50**(10), 4580–4585 (2011).
[441]O. Mayasree, C. R. Sankar, Y. Cui, A. Assoud, and H. Kleinke, "Synthesis, structure, and thermoelectric properties of barium copper polychalcogenides with chalcogen-centered Cu clusters and Te_2^{2-} dumbbells," Eur. J. Inorg. Chem. **2011**(26), 4037–4042.
[442]D. K. Amarasinghe, P. Yox, G. Viswanathan, A. N. Adeyemi, and K. Kovnir, "Modulation of transport properties via S/Br substitution: Solvothermal synthesis, crystal structure, and transport properties of $Bi_{13}S_{17}Br_3$," Dalton Trans. **51**(43), 16748–16756 (2022).
[443]B. Xu, T. Feng, M. T. Agne, Q. Tan, Z. Li, K. Imasato, L. Zhou, J.-H. Bahk, X. Ruan, G. J. Snyder, and Y. Wu, "Manipulating band structure through reconstruction of binary metal sulfide for high-performance thermoelectrics in solution-synthesized nanostructured $Bi_{13}S_{18}I_2$," Angew. Chem. Int. Ed. **130**(9), 2437–2442 (2018).
[444]A. Vogel, T. Miller, C. Hoch, M. Jakob, O. Oeckler, and T. Nilges, "$Cu_{9.1}Te_4Cl_3$: A thermoelectric compound with low thermal and high electrical conductivity," Inorg. Chem. **58**(9), 6222–6230 (2019).
[445]A. Vogel and T. Nilges, "Ion dynamics and polymorphism in $Cu_{20}Te_{11}Cl_3$," Inorg. Chem. **60**(20), 15233–15241 (2021).
[446]C. Doussier, P. Léone, and Y. Moëlo, "Single crystal structure and magnetic properties of $MnSbS_2Cl$," Solid State Sci. **6**(12), 1387–1391 (2004).
[447]C. Doussier, G. André, P. Léone, E. Janod, and Y. Moëlo, "Magnetic study of two isotypic manganese chloro-sulfides: $MnSbS_2Cl$ and the new compound $MnBiS_2Cl$," J. Solid State Chem. **179**(2), 486–491 (2006).
[448]X. Yu, H. Shao, X. Wang, Y. Zhu, D. Fang, and J. Hong, "Anomalous lattice thermal conductivity in layered MNCl (M = Zr, Hf) materials driven by lanthanide contraction," J. Mater. Chem. A **8**(6), 3128–3134 (2020).
[449]C. J. Hawkins, J. A. Newnham, B. Almoussawi, N. L. Gulay, S. L. Goodwin, M. Zanella, T. D. Manning, L. M. Daniels, M. S. Dyer, T. D. Veal, J. B. Claridge, and M. J. Rosseinsky, "Synthesis, structure, and properties of $CuBiSeCl_2$: A chalcohalide material with low thermal conductivity," Chem. Mater. **36**(9), 4530–4541 (2024).
[450]Q. D. Gibson, M. S. Dyer, G. F. S. Whitehead, J. Alaria, M. J. Pitcher, H. J. Edwards, J. B. Claridge, M. Zanella, K. Dawson, T. D. Manning, V. R. Dhanak, and M. J. Rosseinsky, "$Bi_4O_4Cu_{1.7}Se_{2.7}Cl_{0.3}$: Intergrowth of BiOCuSe and Bi_2O_2Se stabilized by the addition of a third anion," J. Am. Chem. Soc. **139**(44), 15568–15571 (2017).
[451]Q. D. Gibson, M. S. Dyer, C. Robertson, C. Delacotte, T. D. Manning, M. J. Pitcher, L. M. Daniels, M. Zanella, J. Alaria, J. B. Claridge, and M. J. Rosseinsky, "Bi_{2+2} nO_{2+2} $nCu_{2-\delta}Se_{2+n-\delta}X\delta$ (X = Cl, Br): A three-anion homologous series," Inorg. Chem. **57**(20), 12489–12500 (2018).
[452]Q. D. Gibson, T. Zhao, L. M. Daniels, H. C. Walker, R. Daou, S. Hébert, M. Zanella, M. S. Dyer, J. B. Claridge, B. Slater, M. W. Gaultois, F. Corà, J. Alaria, and M. J. Rosseinsky, "Low thermal conductivity in a modular inorganic material with bonding anisotropy and mismatch," Science **373**(6558), 1017–1022 (2021).
[453]Z. Tong, A. Pecchia, C. Yam, T. Dumitrică, and T. Frauenheim, "Glass-like transport dominates ultralow lattice thermal conductivity in modular crystalline $Bi_4O_4SeCl_2$," Nano Lett. **23**(20), 9468–9473 (2023).
[454]J. A. Newnham, T. Zhao, Q. D. Gibson, T. D. Manning, M. Zanella, E. Mariani, L. M. Daniels, J. Alaria, J. B. Claridge, F. Corà, and M. J. Rosseinsky, "Band structure engineering of $Bi_4O_4SeCl_2$ for thermoelectric applications," ACS Org Inorg Au **2**(5), 405–414 (2022).
[455]Q. D. Gibson, J. A. Newnham, M. S. Dyer, C. M. Robertson, M. Zanella, T. W. Surta, L. M. Daniels, J. Alaria, J. B. Claridge, and M. J. Rosseinsky, "Expanding

multiple anion superlattice chemistry: Synthesis, structure and properties of $Bi_4O_4SeBr_2$ and $Bi_6O_6Se_2Cl_2$," J. Solid State Chem. **312**, 123246 (2022).
[456]R. Ji, M. Lei, C. Genevois, W. Zhang, X. Ming, L. He, M. Allix, C. Yin, X. Kuang, and X. Xing, "Multiple anion chemistry for ionic layer thickness tailoring in $Bi_{2+2n}O_{2+2n}SenX_2$ (X = Cl, Br) van der Waals semiconductors with low thermal conductivities," Chem. Mater. **34**(10), 4751–4764 (2022).
[457]J. A. Newnham, Q. D. Gibson, T. W. Surta, A. Morscher, T. D. Manning, L. M. Daniels, J. B. Claridge, and M. J. Rosseinsky, "Low thermal conductivity in $Bi_8CsO_8SeX_7$ (X = Cl, Br) by combining different structural motifs," J. Mater. Chem. A **11**(29), 15739–15748 (2023).
[458]I.-C. Liang, D. I. Bilc, M. Manoli, W.-Y. Chang, W.-F. Lin, T. Kyratsi, and K.-F. Hsu, "Syntheses, crystal structures and electronic structures of new metal chalcoiodides Bi_2CuSe_3I and $Bi_6Cu_3S_{10}I$," J. Solid State Chem. **234**, 1–8 (2016).
[459]K. Brlec, K. B. Spooner, J. M. Skelton, and D. O. Scanlon, "$Y_2Ti_2O_5S_2$—A promising n-type oxysulphide for thermoelectric applications," J. Mater. Chem. A **10**(32), 16813–16824 (2022).
[460]T. Pandey, A. S. Nissimagoudar, A. Mishra, and A. K. Singh, "Ultralow thermal conductivity and high thermoelectric figure of merit in mixed valence In_5X_5Br (X = S, and Se) compounds," J. Mater. Chem. A **8**(27), 13812–13819 (2020).
[461]J. Mark, W. Zhang, K. Maeda, T. D. Yamamoto, H. Kageyama, and T. Mori, "Ultralow thermal conductivity in the mixed-anion solid solution $Sn_2SbS_{2-x}SexI_3$," J. Mater. Chem. A **11**, 10213–10221 (2023).
[462]S.-M. Liu, J.-J. Shi, Y.-H. Zhu, W.-H. Guo, Y. He, C. Tian, X. Wang, and H.-X. Zhong, "Significant reduction of the lattice thermal conductivity in antifluorites via a split-anion approach," Phys. Rev. B **107**(20), 205206 (2023).
[463]L. Kunduru, N. Yedukondalu, S. C. R. Roshan, S. Sripada, M. Sainath, L. Ehm, and J. B. Parise, "Pressure-induced martensitic phase transition and low lattice thermal conductivity of SrClF," J. Phys. Chem. C **125**(31), 17261–17270 (2021).
[464]N. Yedukondalu, A. Shafique, S. C. Rakesh Roshan, M. Barhoumi, R. Muthaiah, L. Ehm, J. B. Parise, and U. Schwingenschlögl, "Lattice instability and ultralow lattice thermal conductivity of layered PbIF," ACS Appl. Mater. Interfaces **14**(36), 40738–40748 (2022).
[465]W. Guo, Q. Huang, W.-L. Zhang, D.-G. Chen, A. Chen, E. H. Ang, H.-H. Cui, Z.-Z. Luo, and Z. Zou, "Two mixed-anion semiconductors in the Ba–Sn–Te–S system with low thermal conductivity," ACS Appl. Energy Mater. **6**(4), 2508–2514 (2023).
[466]Y. Shen, F. Q. Wang, and Q. Wang, "Ultralow thermal conductivity and negative thermal expansion of CuSCN," Nano Energy **73**(March), 104822 (2020).
[467]S. Yadav, G. Panigrahi, M. K. Niranjan, and J. Prakash, "Ba_3GeTeS_4: A new quaternary heteroanionic chalcogenide semiconductor," J. Solid State Chem. **323**, 124028 (2023).
[468]S. Jana, S. Yadav, Swati, M. K. Niranjan, and J. Prakash, "$Ba_{14}Si_4Sb_8Te_{32}(Te_3)$: Hypervalent Te in a new structure type with low thermal conductivity," Dalton Trans. **52**(42), 15426–15439 (2023).
[469]E. Al Dawood, A. Shafique, and U. Schwingenschlögl, "Anomalous ultralow lattice thermal conductivity in mixed-anion Ba_4Sb_2Se and Ba_4Sb_2Te," ACS Appl. Electron. Mater. **5**(8), 4268–4274 (2023).
[470]J. Zhang, S. Jia, I. Kholmanov, L. Dong, D. Er, W. Chen, H. Guo, Z. Jin, V. B. Shenoy, L. Shi, and J. Lou, "Janus monolayer transition-metal dichalcogenides," ACS Nano **11**(8), 8192–8198 (2017).
[471]A.-Y. Lu, H. Zhu, J. Xiao, C.-P. Chuu, Y. Han, M.-H. Chiu, C.-C. Cheng, C.-W. Yang, K.-H. Wei, Y. Yang, Y. Wang, D. Sokaras, D. Nordlund, P. Yang, D. A. Muller, M.-Y. Chou, X. Zhang, and L.-J. Li, "Janus monolayers of transition metal dichalcogenides," Nat. Nanotech. **12**(8), 744–749 (2017).
[472]L. Ju, M. Bie, J. Shang, X. Tang, and L. Kou, "Janus transition metal dichalcogenides: A superior platform for photocatalytic water splitting," J. Phys. Mater. **3**(2), 022004 (2020).
[473]D. Mehta, J. Zhang, B. Smith, J. Lou, and L. Shi, "Thermoelectric measurements of high-resistance Janus monolayer transition-metal dichalcogenide," Rev. Sci. Instrum **90**(10), 105110 (2019).
[474]A. Patel, D. Singh, Y. Sonvane, P. B. Thakor, and R. Ahuja, "High thermoelectric performance in two-dimensional Janus monolayer material WS-X (X = Se and Te)," ACS Appl. Mater. Interfaces **12**(41), 46212–46219 (2020).
[475]T. V. Vu, C. V. Nguyen, H. V. Phuc, A. A. Lavrentyev, O. Y. Khyzhun, N. V. Hieu, M. M. Obeid, D. P. Rai, H. D. Tong, and N. N. Hieu, "Theoretical prediction of electronic, transport, optical, and thermoelectric properties of Janus monolayers In_2XO (X=S,Se,Te)," Phys. Rev. B **103**(8), 0 85422 (2021).
[476]M. Guittard, S. Benazeth, J. Dugue′, S. Jaulmes, M. Palazzi, P. Laruelle, and J. Flahaut, "Oxysulfides and oxyselenides in sheets, formed by a rare earth element and a second metal," J. Solid State Chem. **51**(2), 227–238 (1984).
[477]S. J. Clarke, P. Adamson, S. J. C. Herkelrath, O. J. Rutt, D. R. Parker, M. J. Pitcher, and C. F. Smura, "Structures, physical properties, and chemistry of layered oxychalcogenides and oxypnictides," Inorg. Chem. **47**(19), 8473–8486 (2008).
[478]Y. Mizuguchi, "Review of superconductivity in BiS_2-based layered materials," J. Phys. Chem. Solids **84**, 34–48 (2015).
[479]Y. Tsujimoto, K. Yamaura, and E. Takayama-Muromachi, "Oxyfluoride chemistry of layered perovskite compounds," Appl. Sci. **2**(1), 206–219 (2012).
[480]M. Orr, G. R. Hebberd, E. E. McCabe, and R. T. Macaluso, "Structural diversity of rare-earth oxychalcogenides," ACS Omega **7**(10), 8209–8218 (2022).
[481]A. Tassanov, H. Lee, Y. Xia, and J. M. Hodges, "Rational pathways to ordered multianion chalcogenides using retrosynthetic crystal chemistry," J. Am. Chem. Soc. **146**(47), 32627–32639 (2024).
[482]K. Momma and F. Izumi, "VESTA 3 for three-dimensional visualization of crystal, volumetric and morphology data," J. Appl. Crystallogr. **44**(6), 1272–1276 (2011).